SEARCH FOR SECOND GENERATION SCALAR LEPTOQUARK PAIRS WITH THE ATLAS DETECTOR

by

Shanti Wendler

Master of Science, University of Pittsburgh, 2007

Submitted to the Graduate Faculty of

the Department of Physics in partial fulfillment

of the requirements for the degree of

Doctor of Philosophy

University of Pittsburgh

2010

UNIVERSITY OF PITTSBURGH

PHYSICS DEPARTMENT

This dissertation was presented

by

Shanti Wendler

It was defended on

July 21st, 2010

and approved by

Vittorio Paolone, University of Pittsburgh, Associate Professor, Dept. of Physics

Vladimir Savinov, University of Pittsburgh, Associate Professor, Dept. of Physics

Adam Leibovich, University of Pittsburgh, Associate Professor, Dept. of Physics

Arthur Kosowsky, University of Pittsburgh, Associate Professor, Dept. of Physics

Roy Briere, Carnegie Mellon University, Associate Professor, Dept. of Physics

Dissertation Director: Vittorio Paolone, University of Pittsburgh, Associate Professor, Dept. of Physics

SEARCH FOR SECOND GENERATION SCALAR LEPTOQUARK PAIRS WITH THE ATLAS DETECTOR

Shanti Wendler, PhD

University of Pittsburgh, 2010

Proton collisions at the Large Hadron Collider could provide evidence for the existence of leptoquarks, hypothetical bosons that couple directly to leptons and quarks. Monte Carlo based studies of second generation leptoquark pair production in the ATLAS detector are presented, as well as predictions for discovery and exclusion potential with early ATLAS data.

TABLE OF CONTENTS

LIST OF TABLES

LIST OF FIGURES

LIST OF EQUATIONS

1.0 INTRODUCTION

The Standard Model (SM) of particle physics describes most of what particle physicists know about fundamental particles and the forces through which they interact. With the startup of the Large Hadron Collider (LHC), new regions of phase space will be studied for signs of physics beyond the Standard Model (BSM), allowing physicists to search for indications of a more fundamental theory that can not only encompass confirmed SM phenomena but provide explanations for SM properties whose origins are currently unknown. For example, although leptons and quarks appear as independent fields in the SM, the remarkable symmetry between the two types of matter suggests that a more fundamental theory could unify the fields in a single matter multiplet [1]. Since baryogenesis requires that baryon and lepton numbers are not conserved at some energy scale, it is not surprising that grand unified theories (GUTs) predict theoretical particles that couple to both leptons and quarks and mediate transitions between the two. Such hypothetical bosons are generally referred to as leptoquarks, and although their masses have loose experimental and theoretical limits, there are scenarios in which they could be produced at the LHC [2]. The following chapters of this dissertation outline a strategy for the search of second generation leptoquarks with the ATLAS detector. Discovery and exclusion predictions are also presented, based on the fully simulated response of the ATLAS detector in Monte Carlo data.

2.0 ATLAS DETECTOR AND ITS PERFORMANCE

With a main ring diameter of more than 8 km and containing over 6,000 magnets, the LHC is the largest machine ever built. Designed for a center of mass energy of 14 TeV, the LHC will circulate and collide proton beams inside of three main detectors, ATLAS, CMS, and LHCb. ATLAS and CMS are multipurpose experiments, designed to detect a wide range of physical processes, and LHCb is designed to study B meson production and decays. In addition to colliding protons, the LHC will also accelerate and collide lead ion beams, which will intersect inside the ALICE detector. Such collisions are expected to produce a quark-gluon plasma, a state of matter where colored particles are deconfined. Design parameters for the LHC were constrained by the size of the existing LEP tunnel and the strength of the latest superconducting magnets. The injector chain for the LHC begins with a linear particle accelerator, Linac2, which generates 50 MeV protons and feeds them into three successive synchrotron accelerators. The Proton Synchrotron Booster (PSB) accelerates the protons to 1.4 GeV and transfers them into the Proton Synchrotron (PS), which accelerates them to 26 GeV before feeding them into the Super Proton Synchrotron (SPS), where they are accelerated to 450 GeV before being injected into the main ring. In the main ring, the protons are focused into bunches and accelerated to their collision energy, which will be 3.5 TeV for the first two years of operation. After 18-24 months of operation, the LHC will be shut down for repairs and upgrades in preparation for accelerating the beams to the design energy of 7 TeV per beam [3].

The ATLAS detector consists of 5 subdetectors. The inner detector tracks particles from the interaction point, the calorimeters measure particle energies, the muon system tracks particles leaving the calorimeters, magnet systems provide the bending power needed for momentum measurements of charged particles through the trackers, and the trigger system

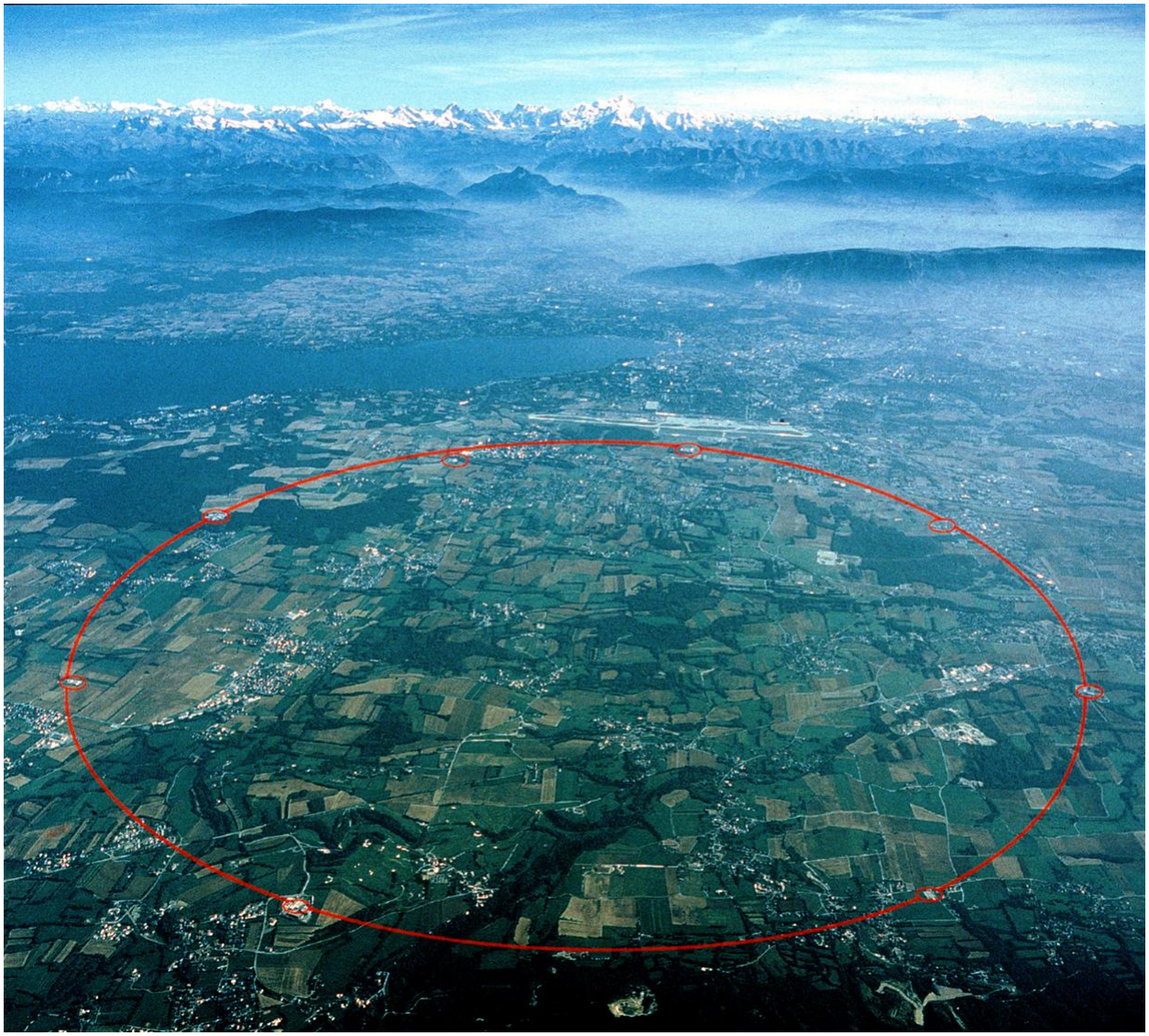

Figure 2.1: Aerial view of the Swiss/French border with the French Alps in the background and the LHC ring overlaid (ATLAS at 2 o'clock on the ring)

determines which events should be recorded and analyzed further.

Following the readout of the detector, reconstruction algorithms can begin. First, standalone reconstruction is performed for each subdetector, and then information from different subdetectors is combined, improving the accuracy of momentum measurements and particle identification. The properties and performances of each subdetector and the various particle reconstruction algorithms are summarized in the following chapter.

2.1 MAGNET SYSTEM

The magnet system consists of a central solenoid surrounding the inner detector and three air-core toroids in the muon spectrometer. A central refrigeration plant provides forced flow helium at 4.5 K, which indirectly cools the magnets through tubes welded on the casings of the windings. With a nominal field of 2 T, the central solenoid provides bending power about the beam axis for the inner detector. Due to its position between the inner detector and electromagnetic calorimeter, the central solenoid is designed to be as thin and transparent as possible so as not to interfere with the performance of the calorimeter. In addition, the central solenoid and liquid argon calorimeters share a single vacuum vessel in order to eliminate two vacuum walls between them.

The three toroid magnets in the muon spectrometer provide bending power along the beam axis for the muon spectrometer system. With total dimensions of 26 m in length and 20 m in diameter, the toroids are the largest superconducting magnets ever built. The system consists of one barrel toroid and two end-cap toroids. Each toroid consists of eight coils evenly spaced about the beam axis, and the end-cap toroids are rotated 22.5° with respect to the barrel to improve the bending power in the transition region. The barrel toroid provides a peak field of 3.9 T, and the end-cap toroids have a peak field of 4.1 T. In the barrel toroid, each coil is housed in its own cryostat, and the eight coils in each end-cap toroids are contained in a single cryostat. Service lines running through a gap in the center of the muon spectrometer (MS) link the eight barrel cryostats to a separate service cryostat, providing connections to the power supply, helium refrigerator, vacuum systems,

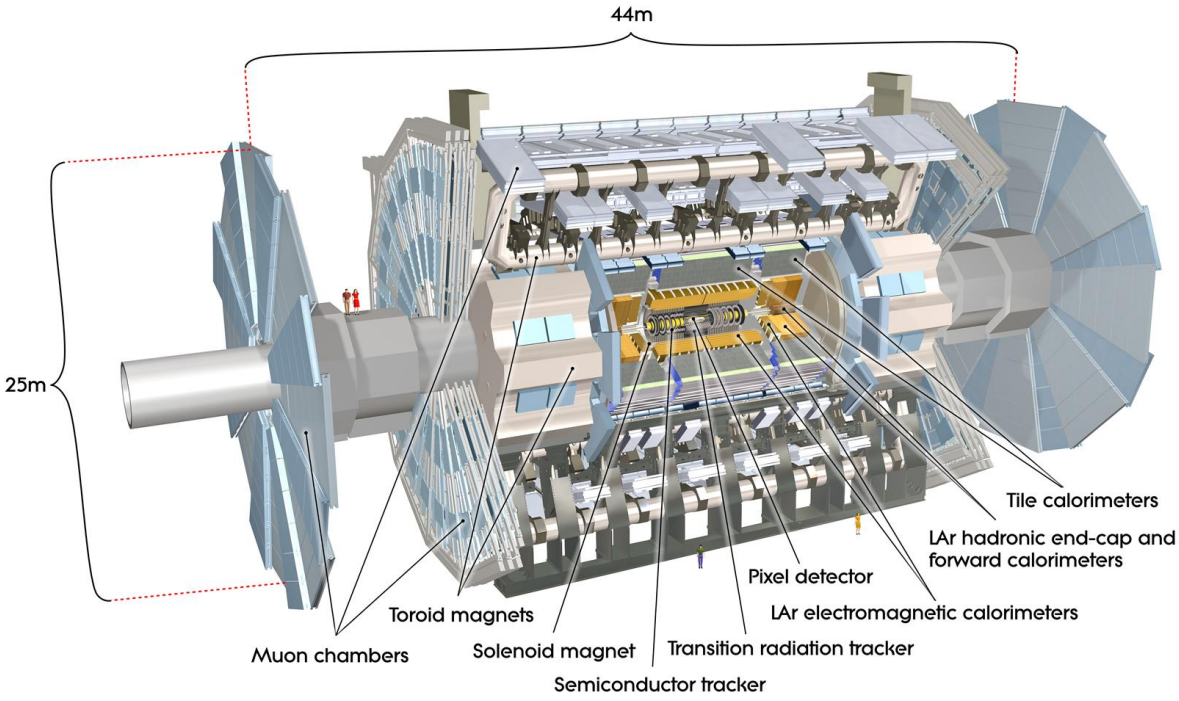

Figure 2.2: Computer generated graphic of the ATLAS detector

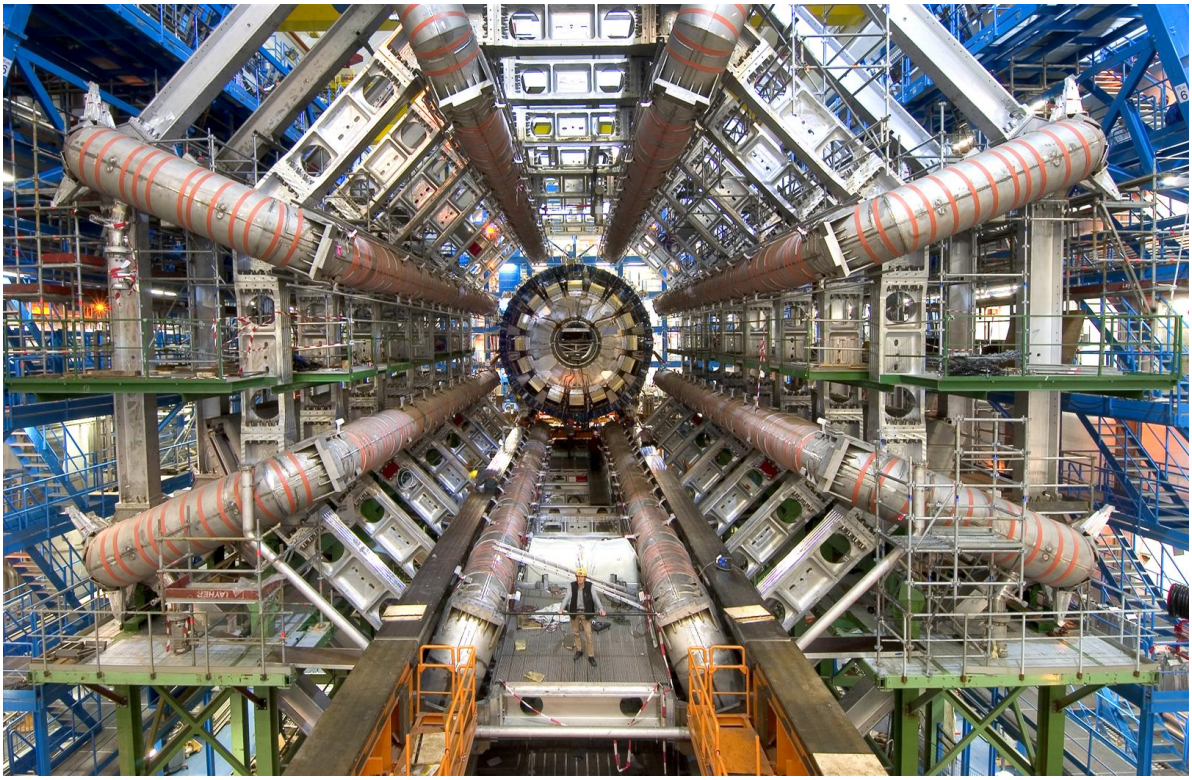

Figure 2.3: View into the center of the toroid as the barrel calorimeter is inserted

and control systems. The aluminum support structures and open air design allow for a relatively lightweight system for its size, approximately 1,300 tons in total. In the barrel, the support structures and coils are important due to their interference in the coverage of the first layer of sensitive material in the MS and will be discussed further in the muon spectrometer section [4].

2.2 INNER DETECTOR

The inner detector is designed to provide high-resolution measurements nearest the interaction point with continuous tracking out to the calorimeters. This is achieved with three subsystems: the pixel detector, the semiconductor tracker (SCT), and the transition radiation tracker (TRT), all of which are enclosed by the central solenoid at a nominal field of 2 T. The finest granularity is achieved using pixel and silicon microstrip technologies nearest the interaction point with a resolution on the order of 10-100 μm, although the number of layers is limited by their high cost and the amount of material they introduce. Straw tube trackers provide a large number of points per track at a lower cost and using less material [5].

2.2.1 Pixel Detector

The pixel detector surrounds the interaction point and primarily determines the impact parameter resolution and detection efficiency of short-lived mesons and tau leptons. With three barrel layers and three disks on each end-cap, the detector provides almost complete angular coverage and extends radially from 51 mm to 122 mm in the barrel, with a length of 400 mm. The first layer, at a radius of 51 mm from the beam axis in the barrel, is often called the vertexing layer, as it provides the measurements closest to the interaction point, making it extremely important for accurately reconstructing primary and secondary vertices in the beam pipe. Tau leptons, b quarks, and heavy flavor mesons have decay lengths on the order of 100 μm, and the intrinsic resolution of the pixel detector is approximately 10 μm in

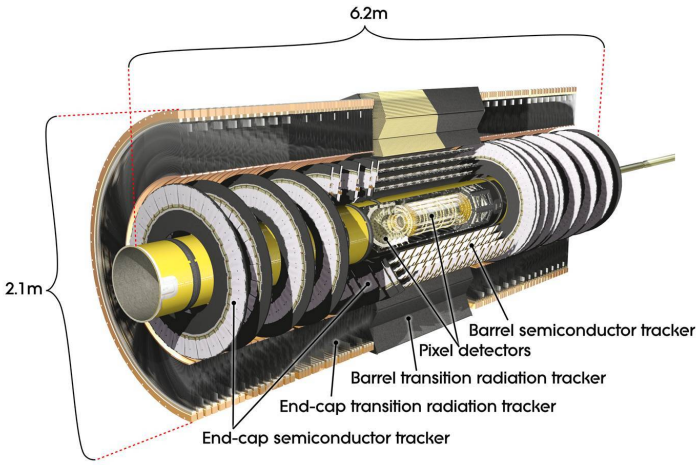

Figure 2.4: Computer generated graphic of the ATLAS inner detector

R-ϕ plane (115 μm in z), making it possible to reconstruct these secondary vertices. With two-dimensional segmentation and three layers, space-points are more easily interpreted, but the readout requires complex electronic techniques. Pixel elements with individual circuits are arranged in 24×160 arrays on readout chips, where information can be buffered while awaiting the level-1 trigger decision. The chip must be bonded to the detector substrate to allow such a high density of connections. In total, the detector contains more than 140 million pixels, each 50×400 μm^2 [5].

2.2.2 Semiconductor Tracker

The SCT has four double layers of silicon microstrips. Layers are assembled in radially at 30.0, 37.3, 44.7, and 52.0 cm from the beam axis. Each silicon detector is 6.36×6.40 cm^2 and has 768 readout strips, providing resolutions of 17 μm in the ϕ direction and 580 μm in z for a module with a single measurement in each direction. Four silicon detectors form a module, where two detectors are bonded together to form 12.8 cm long strips, and these two detector pairs are glued back-to-back at a small angle, separated by a heat transport plate. The electronics for readout are mounted above the detectors, where hits are stored awaiting the level-1 trigger decision. The end-cap modules are similar, except the strips are aligned

along the radial direction in a single layer wheel instead of a double layer barrel shape, and 9 layers are assembled in the z direction. Modules are mounted on carbon fiber cylinders which carry the cooling system. The SCT contains 61 m^2 of silicon detectors with 6.2 million readout channels [5].

2.2.3 Transition Radiation Tracker

The TRT is the last inner detector subsystem within the central solenoid, and it consists of straw detectors which contain sensing wires in individual gas volumes, sandwiched between layers of scintillating plastic foils. Xenon gas is used to detect transition-radiation photons, which helps in discriminating between electrons and pions. Such a technique allows for a large number of measurements per track (typically 30-36), but in turn must handle large occupancy and extremely high counting rates in the ATLAS environment, approximately 5-20 MHz. Single straw hit measurements have resolutions of about 130 μm in the R-ϕ plane at average counting rates. Although only approximately 70% of straws give accurate drift-time measurements, the large number of straws per track yields a combined momentum measurement with less than 50 μm uncertainty, after averaging over all straws and including 30 μm systematic error for the inner detector alignment. Transition radiation measurements provide additional discriminating power when identifying electrons and hadrons in p_T ranges of 1-100 GeV, particularly when trying to distinguish between pions and electrons in the calorimeters. Without the TRT, ATLAS electron identification could not reach the performance level needed for many studies which require a clean sample of events with isolated electrons, particularly in the p_T range 20-40 GeV. Straw spacing has been optimized for tracking performance rather than electron identification, which would be improved by increasing the path length through the radiator with fewer straws. The barrel modules consist of 329-793 axial straws with radial coverage of 56-107 cm from the beam axis. End-cap modules have 18 wheels covering the radial range of 64-103 cm, with the 4 wheels furthest from the interaction point extending to 48 cm from the beam line. The geometry and number of straws are designed to give an approximately constant number of crossed straws ($\sim$30) over the entire acceptance range of $|\eta| < 2.0$ [5].

2.2.4 Track Reconstruction in the ID

Tracking in the inner detector is difficult due to extremely high track density, not only from the large number of particles emerging from the primary interaction, but also multiple proton-proton interactions per bunch crossing. Inner detector tracks are reconstructed with the NewTracking code (NEWT), which performs inside-out track reconstruction, followed by outside-in tracking. Hits from the silicon detectors are reconstructed in three dimensions, tracks seeds are built, and pattern recognition algorithms are applied to find hits toward the outer regions of the ID. The initial collection of tracks is then cleaned, resolving overlapping track segments and shared hits. Silicon tracks are then used to search for compatible TRT hits, which are added as an extension to the original silicon track measurement. Following this inside-out reconstruction, TRT track segments are identified using a global pattern recognition of all hits that have not previously been assigned as extensions to silicon tracks. These TRT segments are then traced back to the silicon detectors in order to assign silicon track segments that were not included in tracks reconstructed in the inside-out procedure. Finally, a second stage pattern recognition is employed to search for vertices, kinks, and their associated tracks [6].

2.2.5 Tracking Performance

In general, the approximate resolution of a track parameter X, as a function of $\mathrm{p_T}$, can be written as:

$$\sigma_X(p_T) = \sigma_X(\infty)(1 \oplus p_X/p_T) \tag{2.1}$$

where σ_X is the resolution of an infinite momentum straight line track and p_X is a constant given by the value of $\mathrm{p_T}$ for which the intrinsic term is known, and $\oplus$ indicates addition in quadrature of the two terms. This expression works well at high or low $\mathrm{p_T}$, when dominated by either the intrinsic detector resolution or multiple scattering term [7]. The analysis presented in this dissertation selects final state objects with extremely high $\mathrm{p_T}$, so ID tracking resolution is dominated by the intrinsic detector errors. Tracks are characterized by 5 parameters, and their resolutions in the inner detector are summarized in Table 2.1. Resolutions are defined as the RMS evaluated for a range of values that include 99.7% of the

Track parameter	$0.25 < \|\eta\| < 0.50$		$1.50 < \|\eta\| < 1.75$	
	$\sigma_X(\infty)$	p_X [GeV]	$\sigma_X(\infty)$	p_X [GeV]
Inverse transverse momentum (q/p_T)	0.34 TeV^{-1}	44	0.41 TeV^{-1}	80
Azimuthal angle (ϕ)	70 μrad	39	92 μrad	49
Polar angle ($\cot\theta$)	0.7x10^{-3}	5.0	1.2x10^{-3}	10
Transverse impact parameter (d_0)	10 μm	14	12 μm	20
Longitudinal impact parameter (z_0)	91 μm	2.3	71 μm	3.7

Table 2.1: Expected track parameter resolution for two η regions, corresponding to a part of the barrel with a minimum amount of material and a part of the end-cap with a maximum amount [7].

data points (corresponding to $\pm 3\sigma$ for a Gaussian distribution). Momentum and angular resolutions are given for isolated muons, since they provide the best reference for optimal performance, while impact parameter resolutions are given for isolated pions, since impact parameters are primarily used to distinguish hadronic decays. As seen in Figure 2.5, track reconstruction efficiency in the inner detector is essentially 100% for high p_T muons and is not expected to be affected by pile-up even at design luminosity. For high-p_T muons, the resolution on the inverse transverse momentum is approximately 4% in the barrel, as seen in Figure 2.6. The resolution for reconstructing primary vertices in the inner detector is approximately 10-15 μm in the transverse plane, and 40-50 μm in the z direction [8].

2.3 CALORIMETERS

The ATLAS calorimeters are sampling detectors, consisting of alternating layers of metal absorbers and sensitive detectors. Electrons, photons, and hadrons produced in the primary interaction trigger particle showers in the absorber layers, while the sensitive detectors mea-

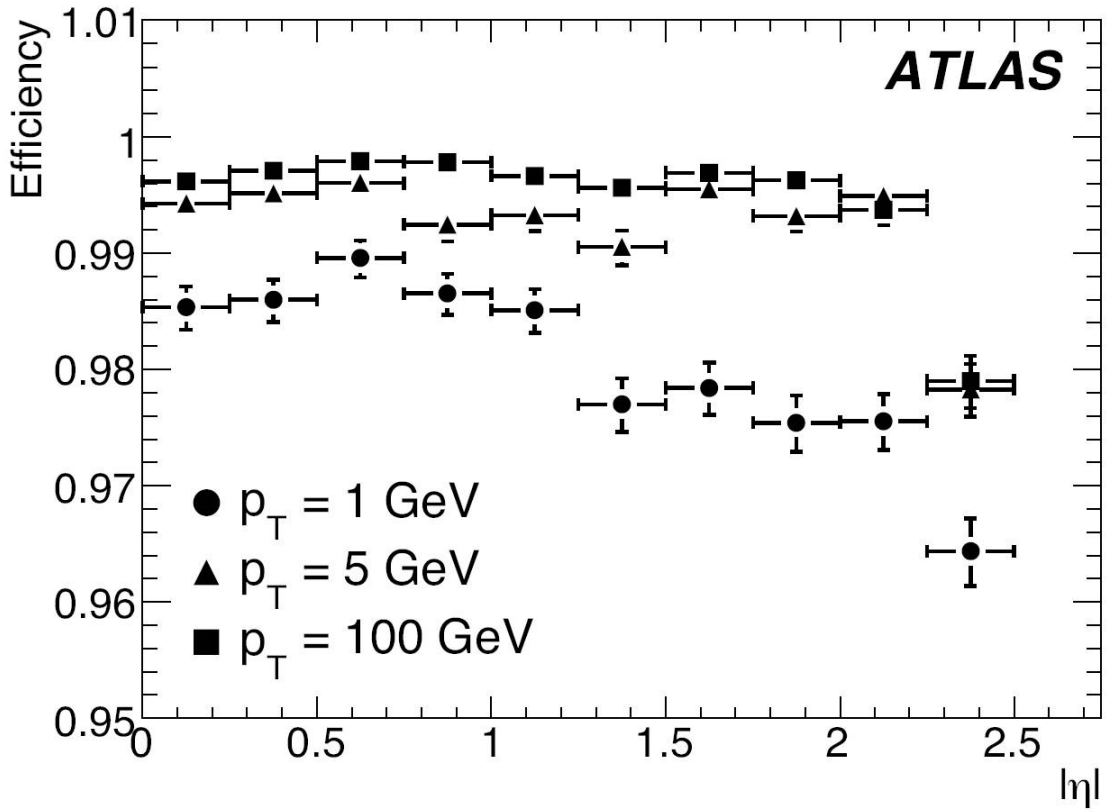

Figure 2.5: ID track reconstruction efficiency as a function of η for muons with p_T =1, 5, and 100 GeV [7]

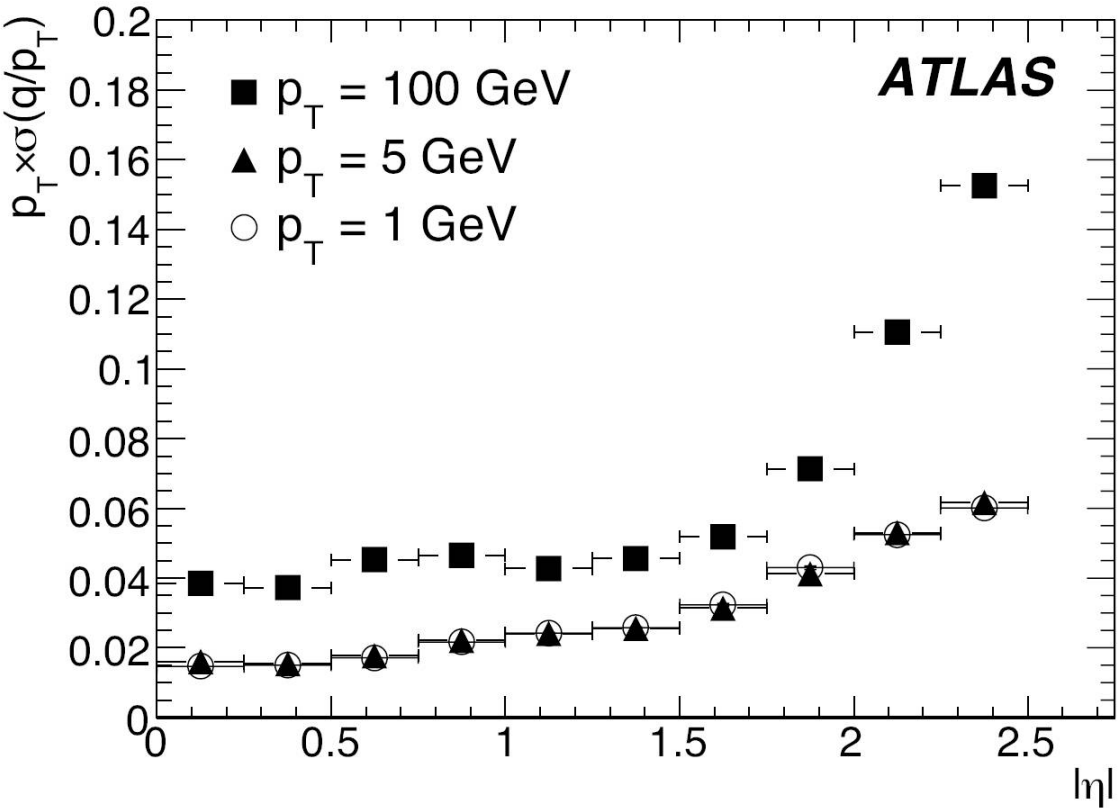

Figure 2.6: Relative transverse momentum resolution for ID tracks as a function of η for muons with p_T = 1, 5, and 100 GeV [7]

sure the shower energies. Calorimeter technology varies in different η regions. The central part of the detector includes electromagnetic calorimeters nearest the central solenoid followed by hadronic tile calorimeters, each covering $|\eta| \leq 3.2$. Forward calorimeters cover the region nearest the beam line at $3.1 \leq |\eta| \leq 4.9$. The electromagnetic calorimeter uses liquid argon (LAr) as the sensitive material with lead absorbers. The hadronic barrel and two extended barrel sections consist of plastic scintillating tiles and iron absorbers, covering the region $|\eta| \leq 1.7$. The hadronic end-cap is a copper LAr detector, covering $1.5 \leq |\eta| \leq 3.2$. Forward calorimeters use LAr in a tungsten matrix at $3.1 \leq |\eta| \leq 4.9$. The LAr technology is intrinsically radiation hard, making it appropriate for the harsh environment of the more forward regions in the calorimeters. A barrel cryostat houses the electromagnetic barrel calorimeter, and two end-cap cryostats house the end-cap electromagnetic, hadronic, and forward calorimeters. Approximately 200,000 signals leave the LAr calorimeters and cryostats through cold-to-warm feedthroughs. All electronics, up to digitization, are contained in front-end crates attached to these feedthroughs in vertical gaps between the barrel and extended barrel tile calorimeters [9].

2.3.1 Electromagnetic Calorimeter

The electromagnetic (EM) calorimeter is a lead LAr detector with Kapton electrodes and lead absorber plates in an accordion geometry, which allows for complete ϕ symmetry without cracks along the beam axis. The calorimeter consists of a barrel section at $|\eta| \leq 1.375$, which is split into two identical sections with a small 6 mm gap, and two end-caps at $1.375 \leq |\eta| \leq 3.2$, which consist of coaxial inner and outer wheels. In the barrel, the lead absorbers and LAr gaps have a constant thickness, although in the end-caps the amplitude of the accordion waves increases radially, and since the absorber thickness is constant, the gap thickness also increases. The total thickness of the EM calorimeter is greater than 24 radiation lengths (X_0) in the barrel and 26 X_0 in the end-cap (upstream material included). In the region used for precise physics measurements, with inner detector tracking and muon spectrometer coverage ($|\eta| \leq 2.5$), the EM calorimeter is segmented in three layers with an additional presampler layer in the barrel. The presampler allows for corrections for energy

lost in upstream material. The first layer of the EM calorimeter is the strip section with a thickness of $\sim$6 X_0 (including upstream material) and consists of narrow strips with a pitch of $\sim$4 mm. As a preshower detector, this section provides precise measurements at the calorimeter entrance and enhances particle identification measurements from the ID, helping to distinguish between electrons or photons and pions. The middle section is segmented into square towers of $\Delta\eta \times \Delta\phi = 0.025 \times 0.025$ with a total thickness of $\sim$24 X_0 (including upstream material) and tapering at higher pseudorapidity. The last section is similar to the middle, only with granularity of 0.05 and providing an additional 2-12 X_0 of thickness. At higher pseudorapidities, two segments with coarser granularity are sufficient for reconstruction of jets and missing ET measurements. Signals are sent to preamplifiers near the feedthroughs and then to bipolar shapers, sampled every 25 ns and stored in analogue memories during level-1 trigger latency. If the level-1 trigger is passed, the samples (approximately 5) are digitized and read out by the data acquisition system [9].

2.3.2 Hadronic Calorimeters

Three hadronic calorimeters are employed to satisfy the widely varying requirements over the acceptance range $|\eta| \leq 4.9$. In the barrel region $|\eta| \leq 1.7$, one central barrel and two extended barrels are composed of three layers of iron absorbers and scintillating tiles. The tiles are staggered in radial distance from the beam line, periodically along z. Tiles are 3 mm thick, with the $14mm$ thick iron absorbers, and are read out by PMTs on two sides. Radially, the tile calorimeter extends from 2.28 to 4.25 m from the beam line, and it is segmented into 64 modules azimuthally with a resulting granularity of $\Delta\eta \times \Delta\phi = 0.1 \times 0.1$. A 68 cm gap between the central and extended barrels contains the front-end electronics and allows space for cables and service pipes from the inner detector, central solenoid, and electromagnetic calorimeters. The total number of readout channels is approximately 10,000, and the fast PMT pulse is transformed by shapers to a unipolar pulse with a 50 ns FWHM.

The hadronic end-cap (HEC) calorimeters, covering the range $1.5 \leq |\eta| \leq 3.2$, are copper LAr detectors, each consisting of two independent wheels with outer radius 2.03 m, with LAr gap geometry and readout similar to the EM calorimeter. Finally, the forward calorimeters

(FCAL) cover the highest pseudorapidities of the acceptance region, $3.1 \leq |\eta| \leq 4.9$. They are composed of tungsten and copper, with liquid argon as the active material. The absorbers are constructed in a honeycomb matrix. A tube and rod with a LAr filled gap between them is inserted in each hole. The rod is held at positive high voltage while the tube and matrix are grounded. This allows for a very thin and precise LAr gap, as small as a few hundred microns in some layers. The forward calorimeters are of course essential in calculating missing E_T (MET), but they are not vital for reconstructing jets in high p_T events [9].

2.3.3 Electron and Jet Reconstruction

Electron, photon, and jet reconstruction algorithms begin with clusters reconstructed from showers in the calorimeters. Clusters in the electromagnetic calorimeters, also known as egamma objects, are reconstructed using two algorithms: the "sliding window" algorithm and the "topological" algorithm.

The "sliding window" algorithm clusters calorimeter cells according to rectangles of fixed sizes, positioning the window such that the contained E_T is a local maximum. Calibration is very precise due to the fixed cluster size. Two such algorithms are employed, one for the electromagnetic calorimeters used for electron and photon identification in a standalone algorithm, and again for the combined clusters which use information from the electromagnetic and hadronic calorimeters. The algorithm begins with tower building, in which the $\eta - \phi$ space of the calorimeters is divided into a grid of elements $\Delta\eta \times \Delta\phi$. Longitudinal cells in an element of $\Delta\eta \times \Delta\phi$ are summed into the tower energy. When tower building is complete, the algorithm searches for preclusters, or seeds. A fixed window is then moved over the grid of tower elements, and a precluster is formed if the transverse energy contained in the window is a local maximum above noise threshold. The position of the precluster is then recomputed as an energy weighted average of η and ϕ for cells within a window about the central tower element. Clusters are then formed by summing cells within a fixed rectangular window of a seed (precluster), whose size depends on the cluster location, seed layer, and hypothesized particle. The windows for finding preclusters, calculating the position of preclusters, and summing cells into clusters, are not necessarily the same.

The topological algorithm begins with a seed cell and adds neighboring cells where the energy deposited is sufficiently above the noise threshold, and as a result can efficiently suppress noise in clusters with a large number of cells. As a result, clusters have varying numbers of cells. Seeds are identified by finding cells with a significant signal to noise ratio above some threshold t_{seed}, and neighboring cells are added if their signal to noise ratio is above some lower threshold t_{cell}. The seed threshold is sufficiently high to protect against electronics and pile-up noise while the lower cell threshold allows accurate measurement of the tails in the shower [10].

In combined electron reconstruction, clusters from the EM calorimeters are matched to ID tracks that do not belong to photon conversions. Shape variables for the egamma objects are also used to define electron candidates of varying quality (i.e. loose, medium, and tight). Examples of important variables used in medium electron identification are given in Table 2.2.

Clusters are also used as input to jet building algorithms and MET. Jets can begin with two types of clusters, topological clusters or calorimeter tower clusters, and additionally, ATLAS jet reconstruction algorithms can be divided into two categories, cone algorithms and cluster algorithms, depending on how the jet constituents (topo or tower clusters) are combined and overlapping composite jet candidates are split or merged. Since the composite objects are built by summing the four-momenta of constituents, rapidity y ($y = \frac{1}{2}\ln\frac{E+p_z}{E-p_z}$), rather than the pseudorapidity η ($\eta = -\ln[\tan\frac{\theta}{2}]$), is meaningful in reconstruction, although η is still most convenient when discussing the distribution of jets in the geometry of the detector, since it maps directly to the angle θ.

Previous cone algorithms (referred to as ATLAS cone algorithms) were iterative in nature, beginning from a seed cluster in the calorimeter and adding energies in a solid cone of various sizes, but this was determined to be an infrared unsafe procedure. A new cone algorithm has been also developed in ATLAS that uses a seedless, infrared safe cone algorithm, or SISCone. To understand the seedless algorithm, consider points in a two dimensional plane. Rather than searching directly for a stable maximum as in a seeded algorithm, the task is to determine a distinct set of circles that encompass two points. This is done by drawing a circle where the two points lie on the edge. There are two such circles and four permutations

of each circle that correspond to both, one, or neither points lying in the circle. The center of each circle is compared to the p_T weighted average centroid of the two points, and if they are the same, then a stable protojet has been identified. In this way, the SISCone algorithm identifies a list of protojets containing a unique combination of clusters. Once protojets are formed, a split/merge algorithm is applied in which protojets that share clusters are either split or merged depending on what fraction of their energies is shared. If they are split into two jets, the shared energy is reconstructed in the higher p_T object.

Clustering algorithms again begin by considering pairs of input objects, and some parameter R quantifies the distance at which the pair should be clustered together. For every input object, the quantities d_{iB} and d_{ij} are calculated, where:

$$d_{iB} = E_{Ti}^{2p} \tag{2.2}$$

$$d_{ij} = min(E_{Ti}^{2p}, E_{Tj}^{2p})(\Delta R_{ij}/R)^2 \tag{2.3}$$

$$\Delta R_{ij} = \sqrt{(y_i - y_j)^2 + (\phi_i - \phi_j)^2} \tag{2.4}$$

If the smallest d value is d_{ij}, then objects i and j are clustered together, and the list is recompiled and run again. If the smallest value is d_{iB}, the object is considered a jet and removed from the list. Qualitatively, R is a parameter for how well jets can be resolved from each other. In the k_T clustering algorithm, $p = 1$, so that objects with low p_T are merged first, and in jet construction, the last merge is the hardest. In the anti-k_T algorithm, $p = -1$, such that low p_T objects near a high p_T object will be merged with the hard object in order of their distance ΔR, with the closest soft objects merging first. In this sense, the clustering algorithm probes the structure of the jet, and can be used to resolve particles or decays within jets [11].

2.3.4 Calorimeter Calibration and Performance

Calibration of the LAr calorimeters is performed in two steps. First, a channel-by-channel calibration of the electronics readout is used to determine an overall energy scale, often called

Type	Description
Acceptance of the detector	$\|\eta\| < 2.47$
Hadronic Leakage	Ratio of E_T in the first sampling of the hadronic calorimeter to E_T of the EM cluster
Second layer of EM calorimeters	Ratio in η of cell energies in 3×7 vs. 7×7 cells
	Ratio in ϕ of cell energies in 3×3 vs. 3×7 cells
	Lateral width of the shower
First layer of EM calorimeter	Difference between energy associated with the second largest energy deposit and energy associated with the minimal value between the first and second maxima.
	Second largest energy deposit normalized to the cluster energy.
	Total shower width.
	Shower width for three strips around maximum strip.
	Fraction of energy outside core of three central strips but within seven strips
Track quality	Number of hits in the pixel detector (at least one).
	Number of hits in the pixels and SCT (at least nine).
	Transverse impact parameter (less than 1 mm).

Table 2.2: Variables used in medium electron identification [12]

"electronics calibration", where the digitized raw signal from each cell is converted into a deposited energy. Next, the cells of each layer are summed in clusters, as described in the previous section, and an energy-weighted position is calculated. Calorimeter geometry leads to three important effects that must be understood for proper calibration of cluster energy and position. First, particles traverse a varying amount of material as a function of ϕ due to the accordion geometry of the LAr absorbers, creating a ϕ modulation of the reconstructed energy. Second, the shower energy is not completely contained in the chosen η window for the cluster, and the granularity of the calorimeter cells is finite. This creates a bias in the measured cluster position as well as a modulation of the reconstructed cluster energy, as a function of η, depending on the actual impact point of a particle within a cell. Third, a particle produced in a vertex away from the beam line no longer intersects each layer at the same η, as a perfectly projective particle produced at the origin would. The luminous region from a shower extends significantly in z, such that properly combining η measurements for such particles requires parameterization of shower depth (both lateral and longitudinal) in each layer. As a result of these detector effects, and since the jet and EM energy scale depend on the position in the detector, initial cluster position measurements must be corrected first, followed by summing the cluster energy in each layer while applying corrections for lateral and longitudinal shower shapes, and finally the impact point of the shower is used to find the necessary corrections for η and ϕ energy modulation.

The overall energy resolution of the EM calorimeters can be generally expressed as $\sigma_{calo} = \sigma_o \oplus \sigma_E/E$. The corrections described here for LAr calorimeters reduce the constant term of the calorimeter energy resolution from 0.65% to 0.43%. The energy dependent term of resolution varies in different regions of the detector, as can be seen in Figures 2.7, 2.8, and 2.9 [8].

The tile calorimeter, which uses PMTs to measure light produced by charged particles in scintillating tiles, is calibrated using two integrated systems, a charge injection system which determines the gain per channel of the digitized PMT output and a laser calibration system which monitors each PMT's properties. Charge injection scans can be performed monthly, and they measure the combined detector-PMT response, while the laser system monitors the stability of the PMT response between scans.

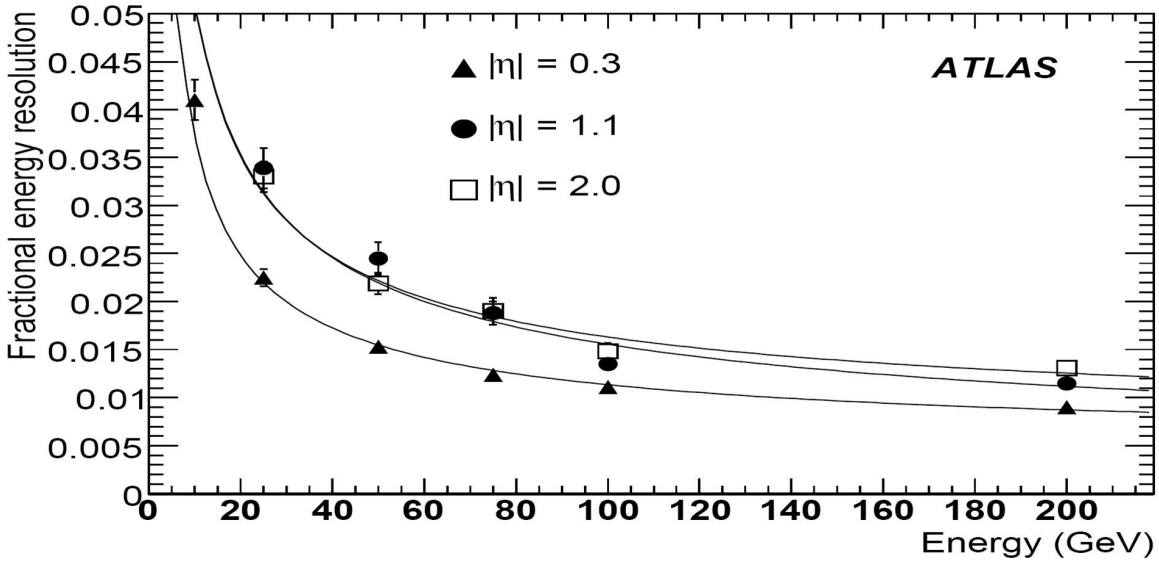

Figure 2.7: Expected fractional energy resolution as a function of energy for electrons in three η regions of the EM calorimeter [12]

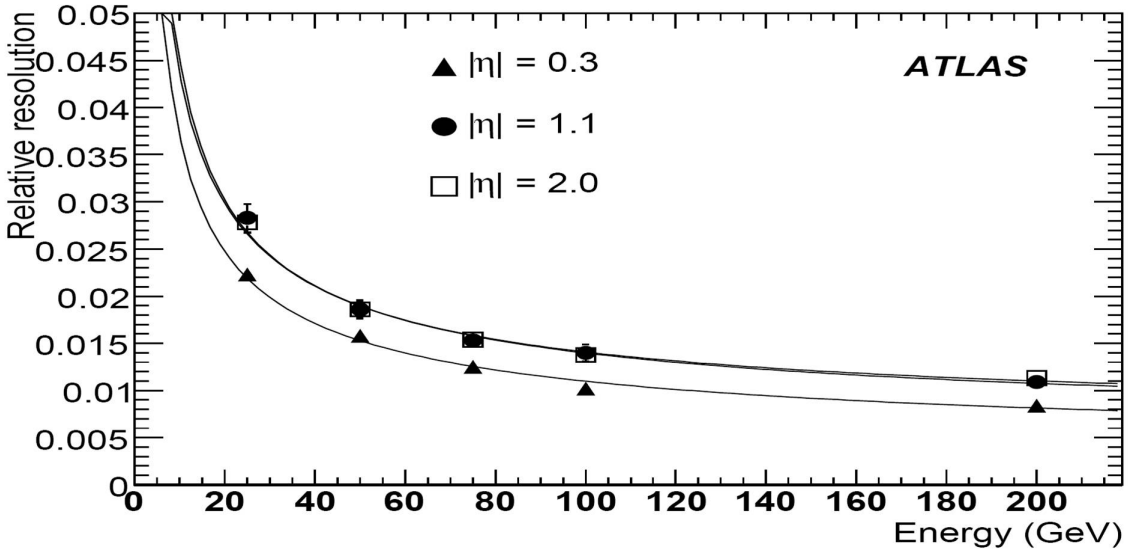

Figure 2.8: Expected Fractional energy resolution as a function of energy for photons in three η regions of the EM calorimeter [12]

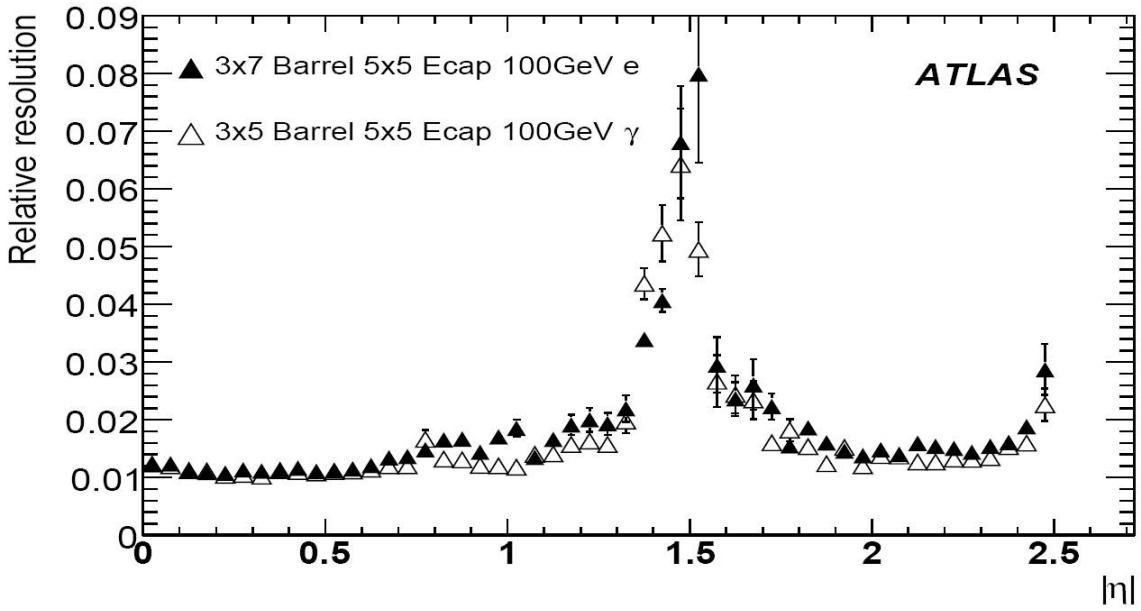

Figure 2.9: Fractional energy resolution as a function of eta for electrons and photons in the EM calorimeter [12]

Performance of various jet building algorithms, as described in the previous section, can be assessed by comparing Monte Carlo jets as built by ATLAS algorithms, using the simulated detector response, and "truth jets" which are jets built at the particle level in the simulation. Jet reconstruction efficiency, jet energy scale, and jet energy resolution can be estimated using Monte Carlo information and are defined as:

$$\text{efficiency} = \frac{\#\text{truth jets matching reconstructed jets with}\Delta R<0.3}{\#\text{truth jets}}$$

$$\text{jet energy scale} = E_{truth}/E_{reco}$$

$$\text{jet energy resolution} = \sigma/E = a/\sqrt{E} + b/E + c$$

where $\Delta R = \sqrt{\Delta\phi^2 + \Delta\eta^2}$ and σ is the jet energy standard deviation. The parameters of jet energy resolution include a sampling term (a), a noise term (b), and a constant term (c). Jet energy resolution is within 2% for all jet algorithms across the entire detector when calibrations derived for each algorithm are used. Jet building performance also depends on the event topology. The leptoquark analysis in this dissertation consists of high p_T events in which the two leading p_T jets are selected. The jet reconstruction efficiency results shown in Figure 2.10 were derived from studies on $t\bar{t}$ events, measuring properties of the light jets coming from one W boson that decays hadronically (while the other decays leptonically). Events were selected by requiring one high p_T lepton from W decay and four high p_T jets, which must not overlap with the selected electron ($\Delta R_{lepton-jet} > 0.4$). Such overlap removal is required since electrons are almost always reconstructed as jets. Reconstruction efficiency as a function of jet p_T , as seen in Figure 2.10, is very comparable for all jet algorithms except for the wide cone jet algorithm, due to the overlap removal criterion. In-situ validation of the jet energy scale is always limited to a particular range of p_T . High p_T measurements can be made by examining events where one high p_T jet is balanced by a recoil system of low p_T jets in the opposing hemisphere. A study of multi-jet events reveals, again, comparable performance between the various cone algorithms. Events are selected by requiring three jets with $|\eta| < 2.5$ and $p_T > 20$ GeV. The jets are ordered in decreasing p_T , and the non-leading

jets where the ϕ direction is within one radian of the opposite ϕ direction of the leading jet, or $\beta = \phi_{jet} - (\pi + \phi_{leadingjet}) < 1$, are summed as the recoil system to be compared to the leading jet. In addition, the ϕ of the recoil system is required to be back-to-back with the leading jet within $\alpha = \phi_{\text{leading jet}} - \phi_{\text{recoil system}} < 0.02$. Figure 2.11 shows that the jet energy scale is validated with comparable performance for all four jet algorithms. Different p_T regimes can be tested with similar p_T balance methods in other systems, such as di-jets, photon-jet systems, where the well-measured photon recoiling against a hadronic system can be used to extract information about the jet energy scale [11].

2.4 MUON SPECTROMETER

The muon spectrometer is the last subdetector that can measure particles' momenta before they escape the ATLAS detector, and it can independently trigger and track over the range $|\eta| \leq 2.4$. The large toroids provide the magnetic field for momentum measurements, and four different technologies are employed for tracking and triggering on charged particles. In the barrel, monitored drift tubes (MDTs), similar to the TRT in the inner detector, provide precision measurements in the bending direction. At high pseudorapidity and near the interaction point, cathode strip chambers (CSCs) are able to handle higher rates and a harsher environment. Resistive plate chambers (RPCs) in the barrel, and thin gap chambers (TGCs) in the end-caps, provide the level-1 trigger information and tracking points in the ϕ direction, orthogonal to the bending direction of the magnets. A 16-fold segmentation in the azimuthal direction follows the 8-fold segmentation of the toroid magnet, and a gap at $\eta = 0$ provides space for cables and service lines to the inner detector, central solenoid, and calorimeters [13].

2.4.1 Monitored Drift Tubes and Cathode Strip Chambers

The MDTs are the primary precision detectors in the muon spectrometer. Similar to the TRT straws in the inner detector, an MDT contains a sensing wire in an individual gas

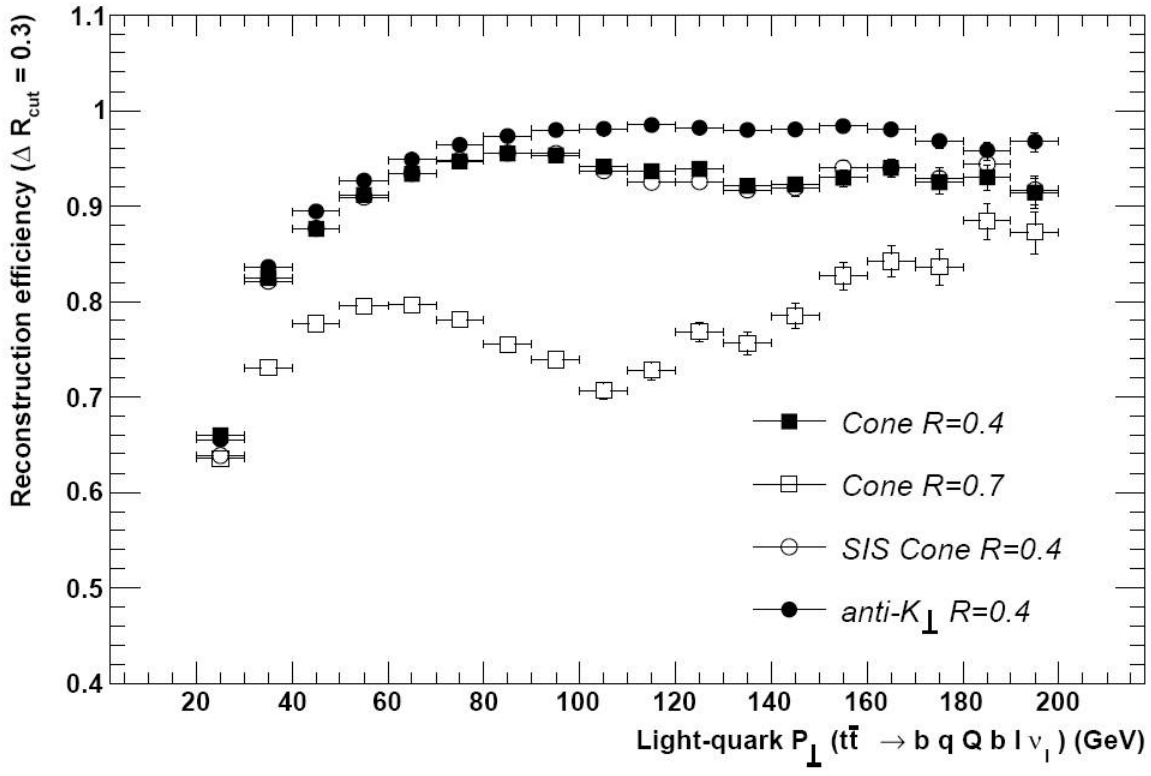

Figure 2.10: Jet reconstruction efficiency for jets coming from W boson decay in $t\bar{t}$ events as a function of jet p_T , where a reconstructed jet is considered matched to a truth jet if $\Delta R_{reco-truth} < 0.3$ [11].

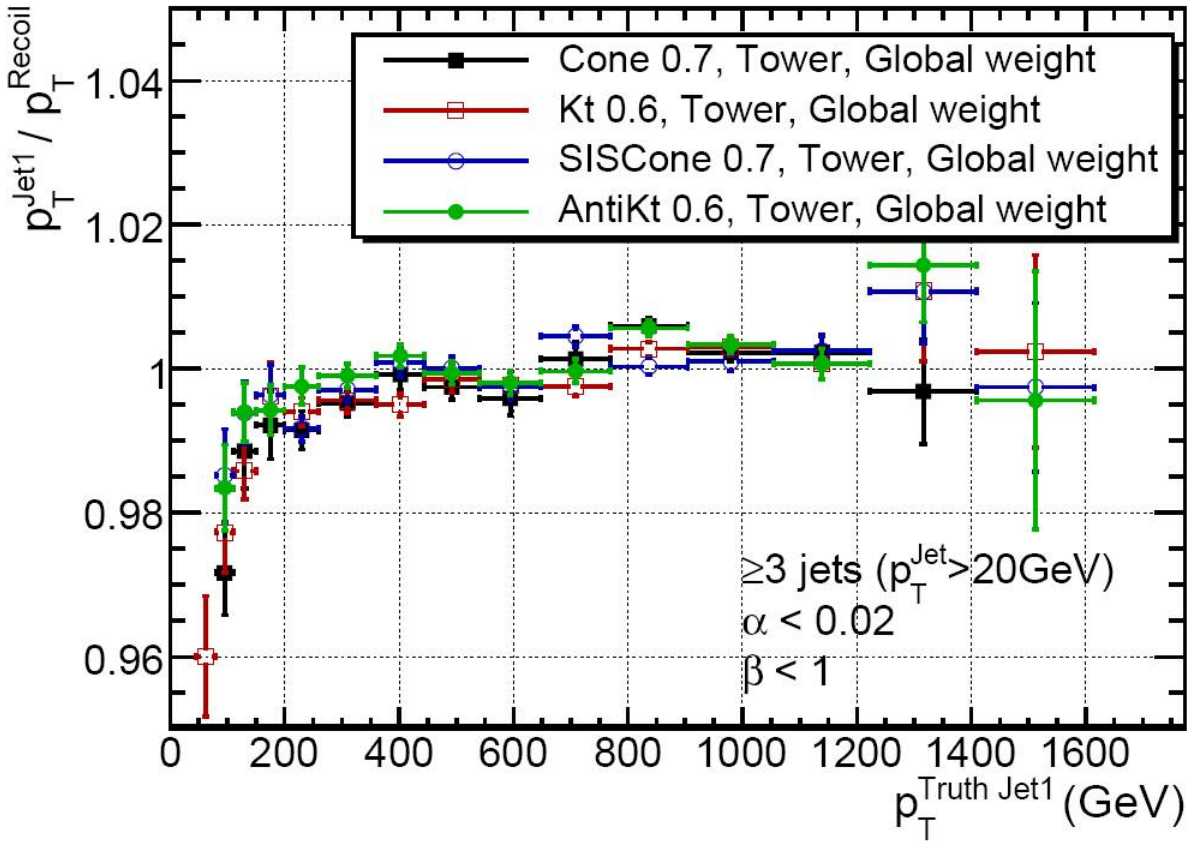

Figure 2.11: Ratio of the p_T of the leading jet and the p_T of the recoil system as a function of the leading jet truth p_T , where the jet is considered matched to a truth jet if $\Delta R_{reco-truth} < 0.3$, in events with at least 3 jets with $p_T > 20$ GeV, $|\eta| < 2.5$, $\beta < 0.1$, and $\alpha < 0.02$ [11].

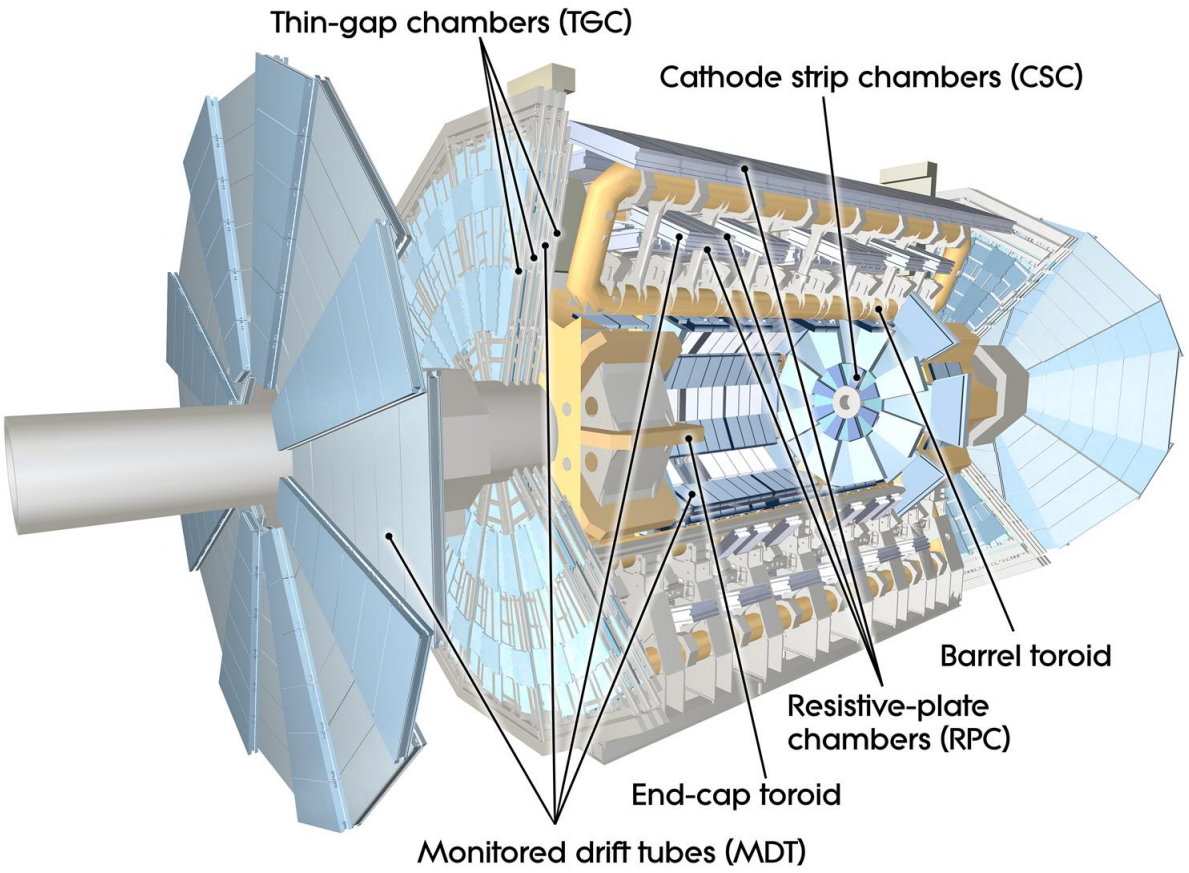

Figure 2.12: Computer generated graphic of the ATLAS muon spectrometer

volume. At a diameter of 30 mm, the tubes are larger than those in the TRT, and they contain a mixture of argon and carbon dioxide with a W-Re wire. The single wire resolution is approximately 80 microns, with a maximum drift time of ∼700 ns. Chambers consist of 2×4 or 2×3 monolayers of MDTs and are arranged in multilayers (3-4) on either side of a rigid support structure to form a "station". Since the tubes range in length from 70-630 cm, gravitational sag cannot be ignored, and the structural supports are used to correct this effect in non-vertical modules. Mechanical deformations of the tubes are monitored with an optical alignment system in situ. Drift tubes are read out at one end, and the detector contains a total of 370,000 MDT readout channels [13].

At high pseudorapidities and near the interaction point, CSCs provide precision measurements. The CSCs are multiwire proportional chambers with cathode strip readout. An avalanche formed on the anode wire induces a charge on the segmented cathode. This segmentation, along with charge interpolation between neighboring strips, gives good spatial resolution, approximately 60 μm. The precision measurement is given by cathode strips perpendicular to the anode wire. There are 67,000 readout channels for the CSCs, but they only cover 27 m^2, or 0.2% of the total area covered by muon spectrometer chambers [13].

2.4.2 Resistive Plate Chambers and Thin Gap Chambers

The RPCs and TGCs alone provide the information needed by the level-1 trigger. In general, high p_T particles traverse three stations in the MS, and information from all three stations is required in order to pass the level-1 high p_T triggers, while only two layers are needed to pass low p_T triggers, as shown in Figure 2.13. These chambers provide information for bunch crossing identification, well defined p_T cutoffs for the level-1 trigger, and measurements perpendicular to the bending direction.

In the barrel, RPCs consist of parallel plastic plates, separated by insulating spacers, and a gap filled with a tetraflouroethane mixture. The outer surfaces of the plates are coated with graphite and connected to the high voltage power supply. Inside the gas gap, ionized electrons are multiplied into avalanches by a high uniform electric field (∼4.5 kV/mm) and are collected on two orthogonal planes of readout strips, providing measurements in both

the eta and phi directions. A chamber consists of two layers of such gas gaps. An infinite momentum straight-line trajectory is interpolated from the chamber hits to the interaction point, defining a window of coincidence. The level-1 p_T threshold describes the allowed deviation from this straight-line trajectory, as illustrated in Figure 2.13. Three RPC layers, or stations, are situated in and among the structure of the toroid magnets, often secured to the structure itself. For this reason, the geometric acceptance of the level-1 trigger in the barrel is reduced to ∼85%, and an image of the holes in the acceptance can be seen in Figure 2.14. The first layers of RPCs are situated on both sides of the middle precision MDT layer, and the last RPC layer is behind the last MDT layer, as shown in Figure 2.15. Concentric cylindrical layers of RPCs cover the range $|\eta| \leq 1$ and are situated at radii of approximately 5, 7.5, and 10 m from the beam axis [13].

TGCs consists of seven layers, each with anode wires in a gas-filled gap sandwiched between cathode plates, and each layer is separated by a paper honeycomb layer to give a rigid structure. The anode wires are aligned along the direction of the precision MDT wires, and charge induced on readout strips orthogonal to the wires provide a second coordinate measurement. Four layers of TGCs cover the end-cap regions at $1.0 \leq |\eta| \leq 2.7$ and are situated in discs at distances of 7, 10, 14, and 22 m from the interaction point. The first layer is in front of the first MDT station, the second TGC station is behind the middle MDT layer, and the third and fourth TGC stations form a doublet behind the last MDT layer [13].

2.4.3 Combined Muon Reconstruction

There are two combined muon reconstruction algorithms for high p_T muons, in which MS tracks are combined with ID tracks. The results from both algorithms, STACO and Muid, are quite consistent with each other. Tracking in the ID is highly efficient, as was described in the previous ID section, and is often considered to be 100% efficient when discussing combined muon reconstruction efficiency. Alternatively, tracking in the muon spectrometer is more difficult and is primarily limited by the large amount of inert material, the varying number of detector stations crossed as a function of position, and the highly inhomogeneous

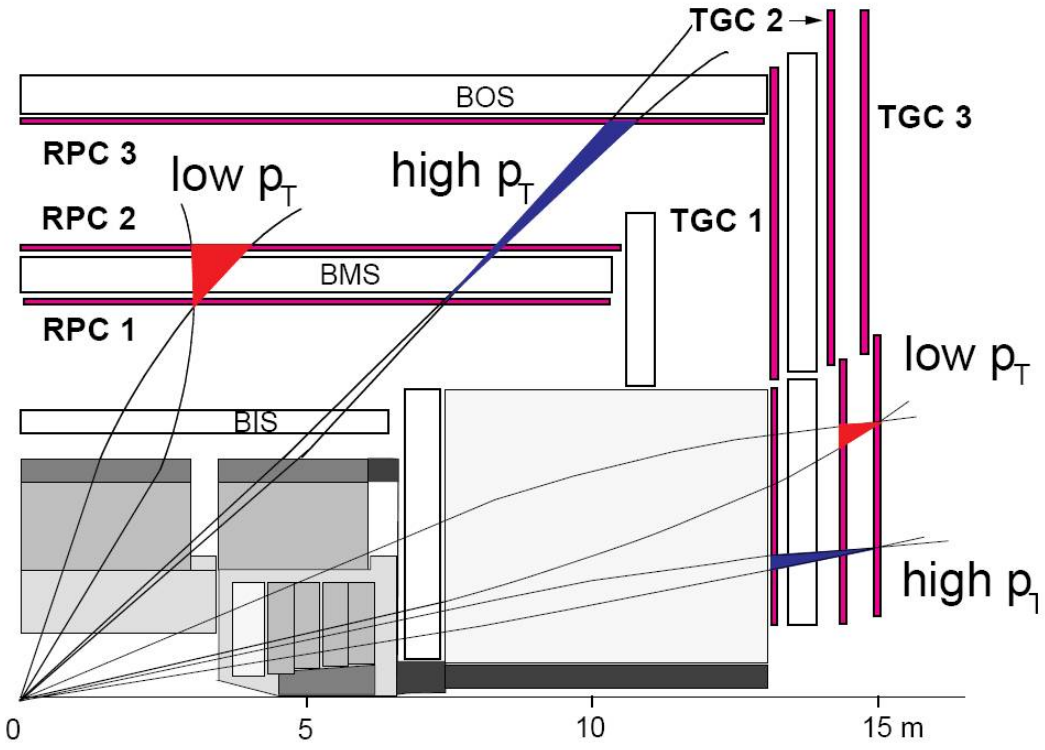

Figure 2.13: Diagram of two LVL1 muon trigger hypotheses in the MS [13]

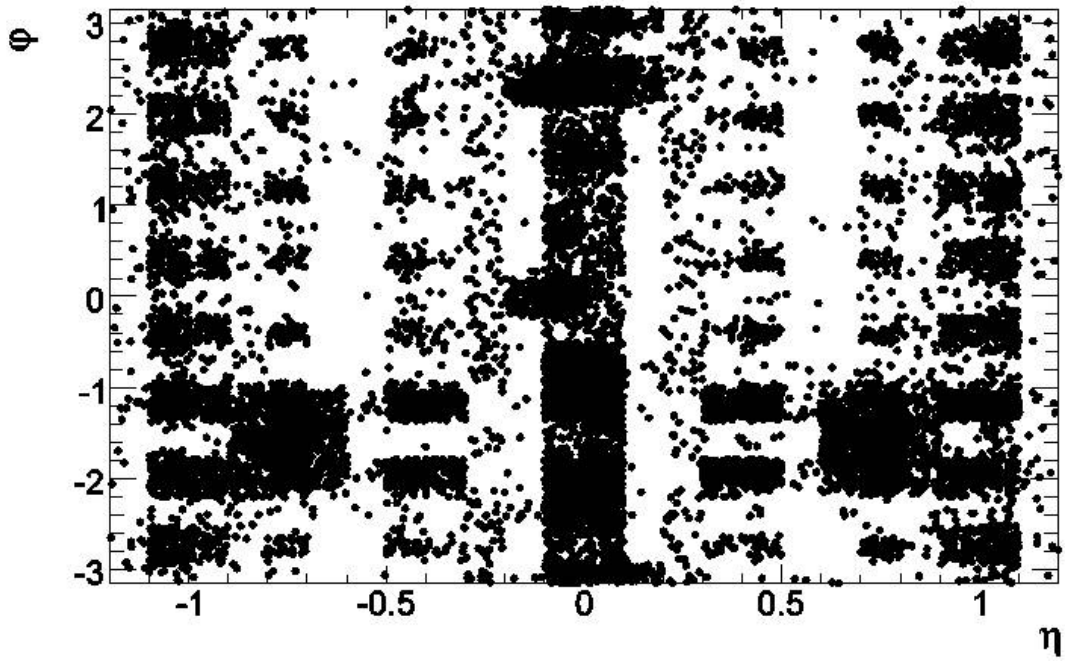

Figure 2.14: $\eta - \phi$ map of holes in RPC coverage due to magnet supports and toroid ribs [13]

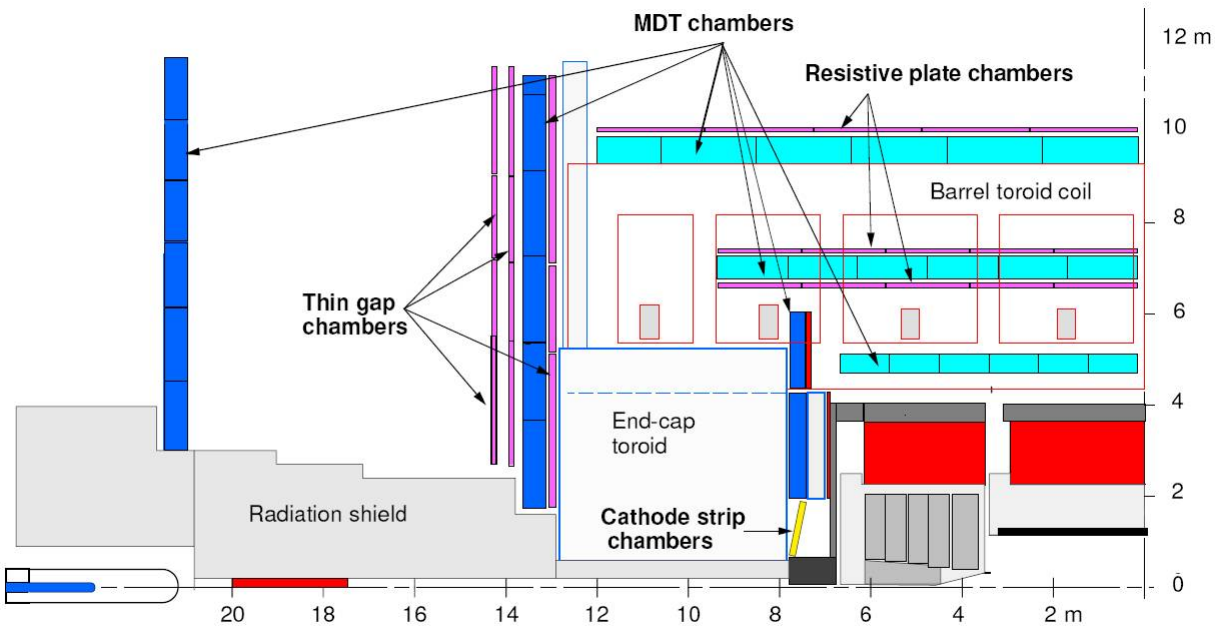

Figure 2.15: Muon Spectrometer [15]

magnetic field.

STACO (STAtistical COmbination) statistically merges the two independent measurements from the MS and ID by combining the covariance matrices of the two tracks. STACO muon spectrometer tracks are found with the standalone Muonboy reconstruction code. Using segment pattern recognition with MDT, CSC, and RPC hits, Muonboy tracks muon candidates through the toroidal magnetic field, fits a track to the hits to extract a momentum measurement, and propagates this track back to the interaction point. Muonboy begins by identifying a region of activity (ROA), which is seeded by the trigger chambers (RPCs and TGCs). Hits from the trigger chambers are formed into straight line segments using a pattern recognition algorithm, and the segments' position and direction is used to extract some rough, first estimates of momentum. Continuous tracking through the magnetic field in three dimensions searches for more segments in other stations. Multiple combinations are tested and track quality estimates determine whether a track is found. If the track points back to the interaction point, a standalone muon candidate has been found. Lastly, a global

fit is performed, starting from the best tracks using the raw hit information rather than segments. Here it is possible to select the best hits for track reconstruction and disregard "bad" hits from cosmic rays or background sources that may have been included in the segment reconstruction. Standalone tracks must be extrapolated back to the IP, at which point energy loss from multiple scattering and energy loss in the calorimeters must be accounted for [14]. Muonboy assigns an energy loss based on the amount of material in the calorimeters along the direction of the extrapolated track [15].

After extrapolating the muon spectrometer track back to the interaction point, inner detector tracks are matched to the standalone muon candidates, and the two tracks are combined using their covariance matrices. For tracks with parameter vectors P_1 and P_2, with covariance matrices C_1 and C_2, the combined track with parameter vector P and covariance matrix C is given by the equation:

$$C^{-1} \times P = C_1^{-1} \times P_1 + C_2^{-1} \times P_2 \tag{2.5}$$

where, given the independent measurements, C is given by:

$$C^{-1} = C_1^{-1} + C_2^{-1} \tag{2.6}$$

so the combined track parameter is the solution to the equation:

$$(C_1^{-1} + C_2^{-1}) \times P = C_1^{-1} \times P_1 + C_2^{-1} \times P_2 \tag{2.7}$$

and the corresponding χ^2 is:

$$\chi^2 = (P - P_1)^T \times C_1^{-1} \times (P - P_1) + (P - P_2)^T \times C_2^{-1} \times (P - P_2) \tag{2.8}$$

The combined track is recorded as a combined muon, and the χ^2 is used as the figure of merit when assessing the quality of the combined muon candidate [15].

Muid begins with the Moore MS track reconstruction algorithm. Moore begins track finding by searching for straight-line segments in the x-y plane, where the bending power of the toroids is negligible. Phi segments are build from the RPC/TGC hits with a histogramming method, since hits from the same track tend to populate the same bin. Crude R-z straight-line segments are then formed for individual MDT modules, which provide the

precision measurement in the bending plane. Pattern recognition algorithms compare the two sets of segments, iteratively combining the segments until a refined track with hits from at least two layers is formed. If the χ^2 of the fit of hits for the resulting track pass some quality criteria and points toward the IP, a high p_T Moore candidate is found. Another stage of pattern recognition loops over these track candidates to assign hits from parts of the detector without LVL1 detectors (i.e. holes in the RPC/TGC geometric acceptance), and another fit is performed. Next, the tracking is further refined by identifying scattering centers along each track, in order to account for multiple Coulomb scattering effects, and an attempt is made to remove any hits from the track which contribute to the χ^2 above some threshold [15].

Moore tracks are propagated back toward the IP through the magnetic field to obtain the track parameters and associated covariance matrices at the point of closest approach to the beam line. Energy loss in the calorimeters due to multiple scattering is either determined by measurements in the calorimeter or estimated using a parameterization as a function of η and muon momentum. The resulting tracks constitute the Muid standalone tracks.

Finally, MS and ID tracks are combined by forming the match χ^2 from the 5 track parameters (as in ID tracks) weighted by the summed covariance matrix:

$$\chi^2_{match} = (T_{ID} - T_{MS})^T (C_{ID} + C_{MS})^{-1} (T_{ID} - T_{MS}) \tag{2.9}$$

where T is the vector of track parameters, expressed at the point of closest approach to the beam line, and C is the covariance matrix. A combined fit is performed for all combinations with a χ^2 probability above some threshold and are retained as combined muons [16].

2.4.4 Combined Muon Performance

As discussed in the previous sections, high p_T muons typically cross three layers, or stations, of detectors, each of which provide precision measurements in the bending plane of the toroid magnets (MDT) and less precise η and ϕ measurements (RPC/TGC) that are used in the LVL1 trigger decision. Various aspects of the MS measurement affect resolution with varying degrees for different momentum ranges in different parts of the detector. Resolution for low

momentum measurements is dominated by uncertainties in energy lost in the material in front of the MS, while intermediate momentum uncertainty is dominated by multiple scattering in the MS, and finally high p_T muon (> 300 GeV) resolution is dominated by the limiting detector resolution and alignment effects. Different contributions to resolution as a function of p_T are summarized in Figure 2.16.

Muon reconstruction efficiency is nearly 100% for both combined algorithms in most regions of the detector, so it is primarily limited by the holes in the geometric acceptance of LVL1 systems (Figure 2.14) and regions where there are fewer than three stations of precision detectors (Figure 2.17). This effect can be seen in the η dependence of the muon reconstruction efficiency in Monte Carlo $t\bar{t}$ events in Figure 2.18, where the "found" efficiency is the fraction of truth muons that match a reconstructed muon within a distance of $\Delta\eta < 0.5$ and $\Delta\phi < 0.5$ and with $p_{Treco} > 0.25 p_{Ttrue}$ for same-sign matches and $p_{Treco} > 0.50 p_{Ttrue}$ for opposite signed matches, and "good" efficiency is the fraction of truth muons that match reconstructed muons using a match of the track parameters, weighted by the covariance matrix of the reconstructed track, where the chi-square probability is above 0.0011, or the "evaluation distance" $D_{eva} = \sqrt{(T_{reco} - T_{true}) C^{-1}_{reco} (T_{reco} - T_{true})} < 4.5$ [15]. An in-situ measurement of muon reconstruction efficiency in data can be obtained using the dimuon signal from Z boson decays, as described in the following section.

The resolution of momentum measurements is also extremely good for both muon algorithms, but the complicated magnetic field in the transition region between the barrel and end-cap toroids degrades the p_T measurement around the region of $|\eta| \sim 1.5$, as seen in Figure 2.19. Muon p_T resolution is also a function of p_T , as shown in Figure 2.20, although the high p_T muons used in the following leptoquark analysis have relatively constant resolution, limited by misalignment of the MS chambers and the intrinsic resolution of the detectors.

2.5 MUON RECONSTRUCTION EFFICIENCY

A tag-and-probe method has been developed to measure the combined muon reconstruction efficiency in data as a function of muon p_T . This study was performed using MC samples

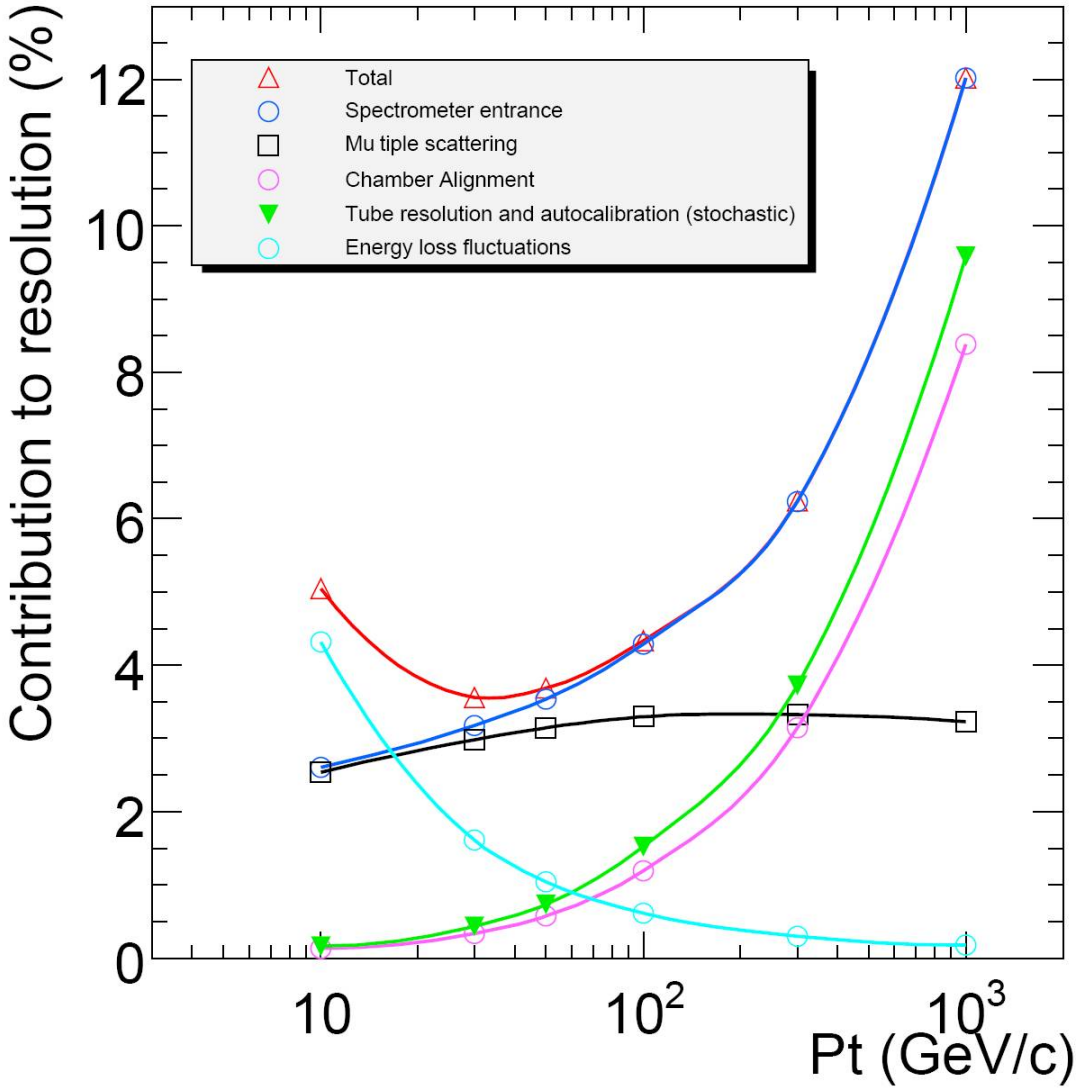

Figure 2.16: Contributions to muon relative momentum resolution as a function of p_T for $|\eta| < 1.5$, where the red curve represents the total resolution, and the dark blue curve represents the total resolution from MS contributions (i.e. pink+black+green). The alignment curve corresponds to an uncertainty of 30 μm in chamber position [15].

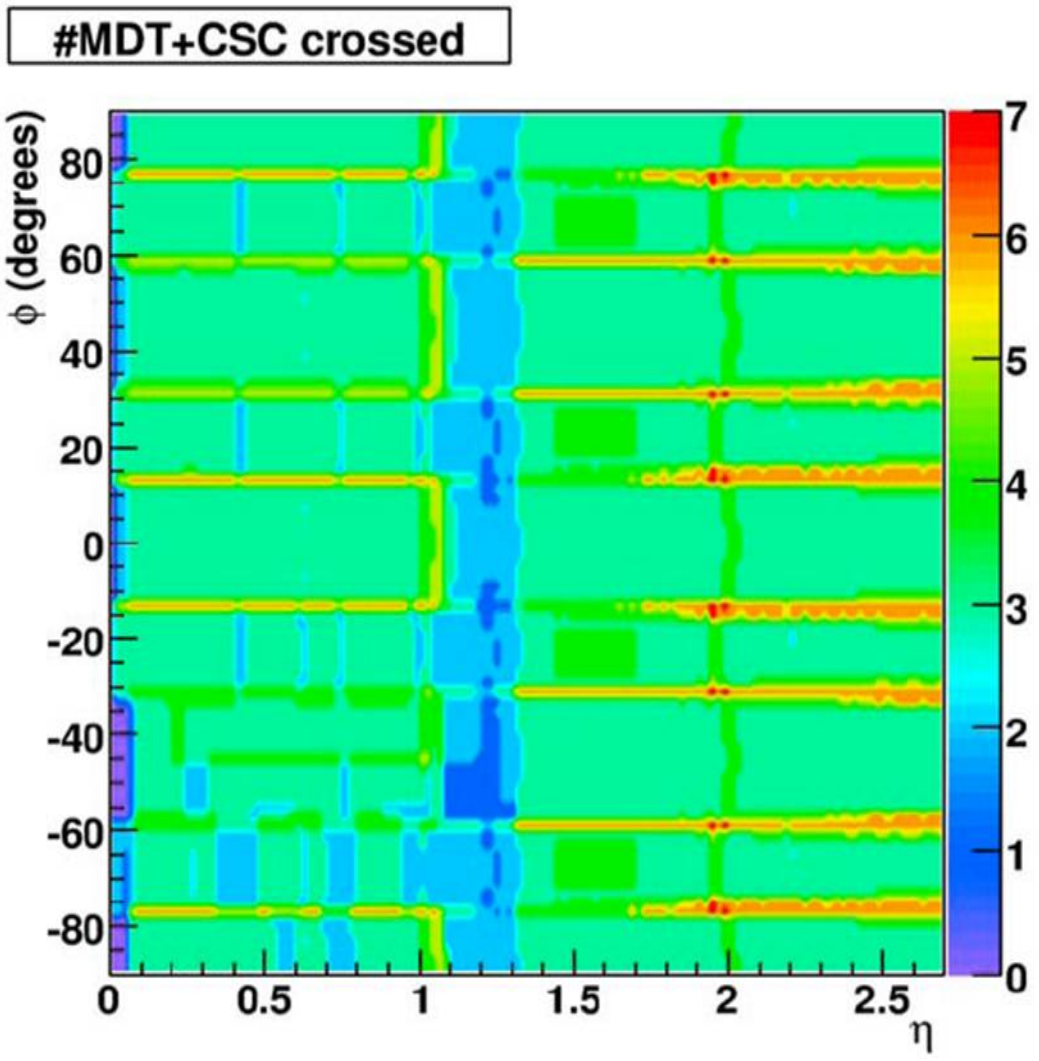

Figure 2.17: Number of precision detector (MDT or CSC) stations crossed by a particle in the MS as a function of η and ϕ [15].

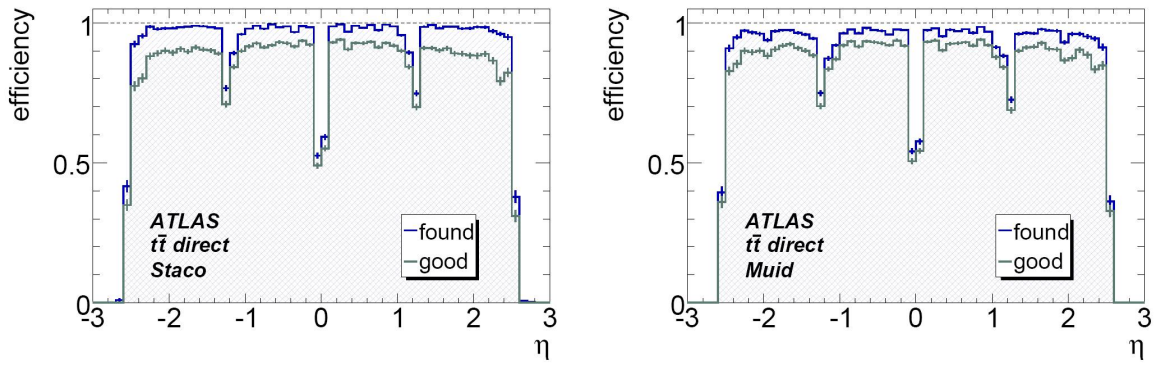

Figure 2.18: Muon reconstruction efficiency as a function of η for STACO (left) and Muid (right) in $t\bar{t}$ events using MC truth matching. See text for definition of "found" and "good" matches [15].

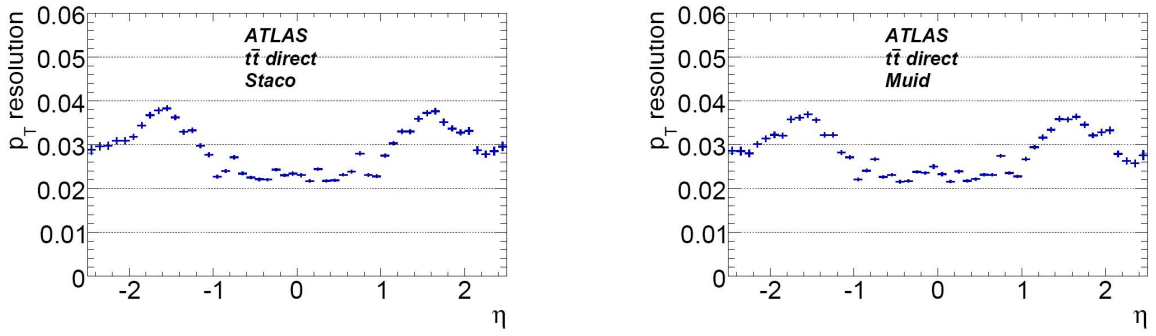

Figure 2.19: Muon relative p_T resolution as a function of η for STACO (left) and Muid (right) in $t\bar{t}$ events using MC truth matching [15].

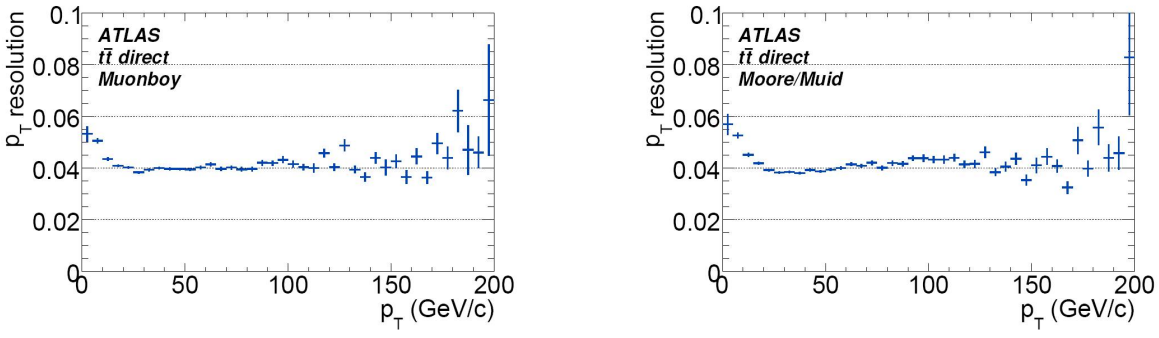

Figure 2.20: Muon relative p_T resolution as a function of p_T for STACO (left) and Muid (right) in $t\bar{t}$ events using MC truth matching [15].

generated at 10 TeV and correspond to 100 pb^{-1} of integrated luminosity. Combined muons refer to candidates with matching tracks in the muon spectrometer (MS) and inner detector (ID). Events are selected by requiring one high quality reconstructed muon (the tag), and then the efficiency of an inner detector track (probe) matching a reconstructed muon with $\Delta R = \sqrt{\Delta\phi^2 + \Delta\eta^2} \leq 0.2$ is measured in such 'tagged' events. Since the presence of a second muon can not be assumed, a distinctive signature for a dimuon event is required. This is provided by the sharp peak of the Z boson in the dimuon mass distribution.

All ID tracks with p_T greater than 20 GeV and $|\eta| \leq 2.5$ (the coverage of the ID) are considered. In an effort to isolate the p_T dependence of muon reconstruction efficiency, probes at $|\eta| \leq 0.1$ and $1.1 \leq |\eta| \leq 1.3$ are excluded due to the inefficiencies in the MS, the former region is a gap for service lines and the latter is a transition region between TGCs and RPCs. The invariant mass of the muon tag and ID probe is analyzed to determine the number of tag-probe pairs that lie in the Z peak. The fraction of tag-probe pairs from the Z peak with a probe matching a reconstructed muon gives the muon reconstruction efficiency. The requirements for a tag and probe are listed in Table 2.3. At least one tag and one probe are required per event, although there can be more. If more than one muon satisfies the criteria for a tag then one is chosen at random. All probes in an event are included in the measurement, excluding inner detector tracks matching the tag muon. Finally, tag-probe

tag	reconstructed standalone MS muon MS track matched to ID track $p_T \geq 20$ GeV $\|\eta\| \leq 2.5$
probe	reconstructed ID track $\|\eta\| \leq 2.5$ $p_T \geq 20$ GeV

Table 2.3: Tag and probe object definitions for muon reconstruction measurements

pairs are divided into bins according to the probe p_T .

The Z peak is assumed to be a Breit-Wigner shape. The detector resolution effects on the reconstructed dimuon mass can be seen in Figure 2.22 and is approximately Gaussian in shape. Although the true Z boson mass distribution follows a Breit-Wigner shape, the presence of final state radiation creates a modified low mass tail in the true dimuon mass distribution (neglecting detector effects), as seen in Figure 2.21. As expected, this is more apparent in lower probe p_T bins, where more energy is carried away by the radiated photon and not reconstructed in the dimuon mass. This effect does not significantly affect the results after backgrounds and detector resolution effects are taken into account, so it is neglected in favor of a simplified shape for the Z mass peak. The shape of the non-Z background is determined using ID tracks with the same sign as the tag muon. Using unbinned maximum likelihood, the tag-probe mass of same-sign pairs is fitted with a polynomial shape, which is then used in the final fits to extract the number of events in the Z peak. An extended maximum likelihood fit is used to extract the number of events in the Z peak in tag-probe distributions where the probe matches a combined muon (n_{comb}) and distributions where the probe doesn't match a combined muon ($n_{notcomb}$). Efficiency is calculated by $\epsilon = n_{comb}/(n_{notcomb} + n_{comb})$, giving an uncertainty of $\sigma_\epsilon = \frac{\sqrt{(\sigma_{n_{comb}} n_{notcomb})^2 + (\sigma_{n_{notcomb}} n_{comb})^2}}{(n_{comb}+n_{notcomb})^2}$.

In order to confirm the validity of the tag and probe method, truth information is used

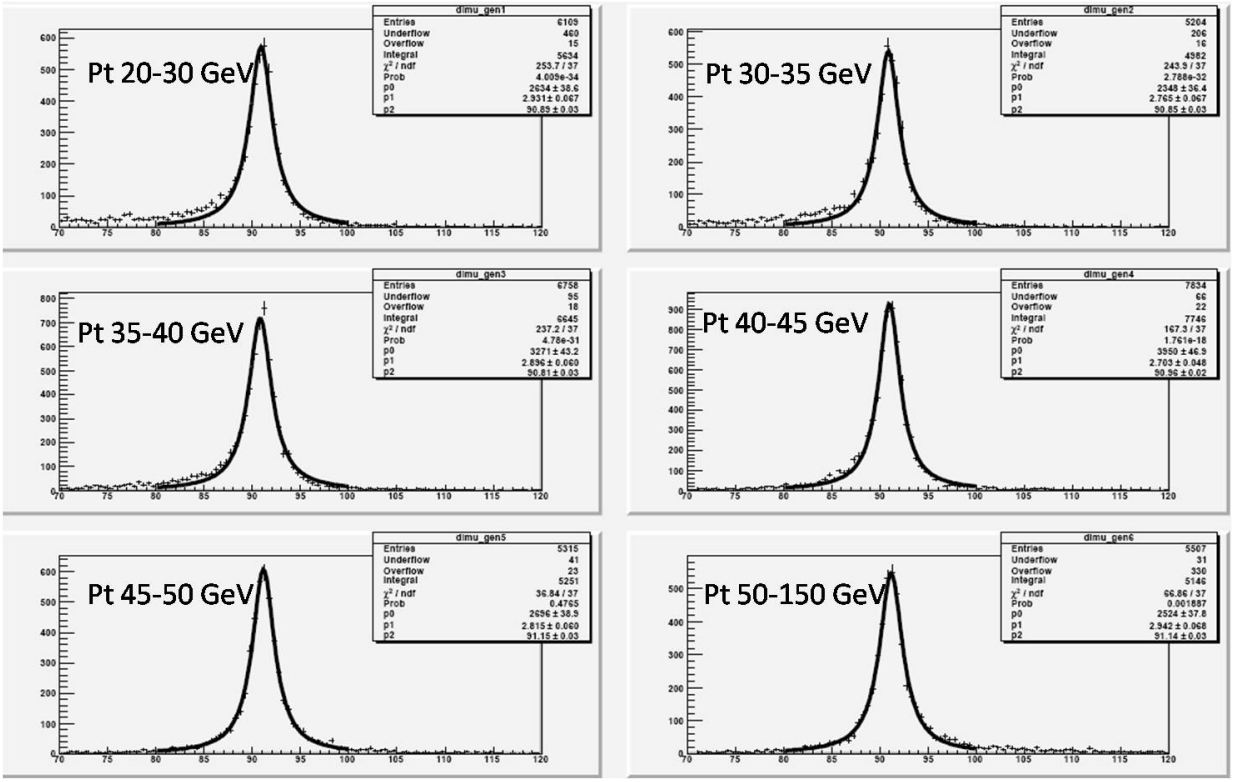

Figure 2.21: Truth dimuon mass for Z events in bins of probe p_T fitted to Breit-Wigner shape

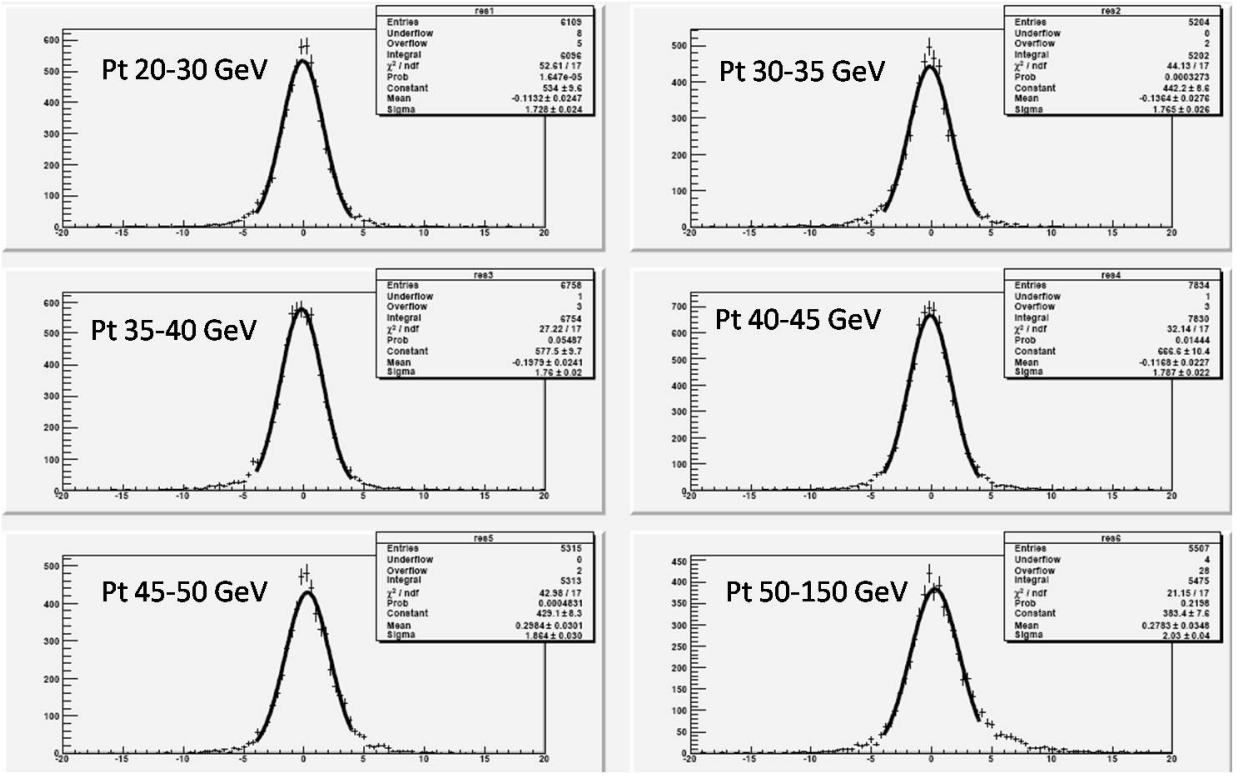

Figure 2.22: M_{Ztruth} - $M_{\mu\mu truth}$ for Z events in bins of probe p_T fitted to gaussian shape

to compare the 'truth tag and probe efficiency' to the overall fraction of muons from Z decay that are reconstructed as combined muons. This 'truth tag and probe efficiency' is given by selecting events where one muon from Z decay is reconstructed and measuring the efficiency of reconstructing the second muon from Z decay as a function of p_T (one tag and one probe per event, both matching truth muons from Z decay). These efficiencies are consistent, as seen in Figure 2.23.

Other than exotic signals, $t\bar{t}$ events are the primary background to Z in the muon channel with such a high p_T requirement on the muon tag. Z and $t\bar{t}$ samples of 200 pb^{-1} integrated luminosity were examined to estimate the performance of the tag and probe muon reconstruction efficiency measurement in data. The reconstructed tag-probe mass for both Z and $t\bar{t}$ is separated into two groups, tag-probe pairs in which the probe matches a combined muon and those that do not. These groups are then sliced in bins of probe p_T and fits are performed to determine the number of tag-probe pairs in the Z peak as a function of p_T as seen in Figures 2.24-2.26. The ratio of combined probes in the peak for a particular bin to the total number of probes in the Z peak yields the reconstruction efficiency for that bin.

Finally, the reconstruction algorithm is tested in a data scenario by applying it to a mixed Monte Carlo sample, created by combining all SM signals without any truth information and applying streaming algorithms (to give a sample as close to real data as possible). Although improvements in fits are needed, the efficiencies obtained are fairly consistent with truth, as seen in Figure 2.27.

2.6 TRIGGER AND DATA ACQUISITION

At LHC design luminosity, the interaction rates inside ATLAS will approach 10^9 Hz, many orders of magnitude greater than what can be accommodated by event builders. ATLAS front-end systems can only accept level-1 (LVL1) triggers at a rate of 75 kHz, and this must be further reduced to 100 Hz before permanent storage. In general, the LVL1 trigger selection is based on reduced granularity information from a subset of detectors. Summarized information from LVL1 hardware in the calorimeters and MS are sent to the central trigger

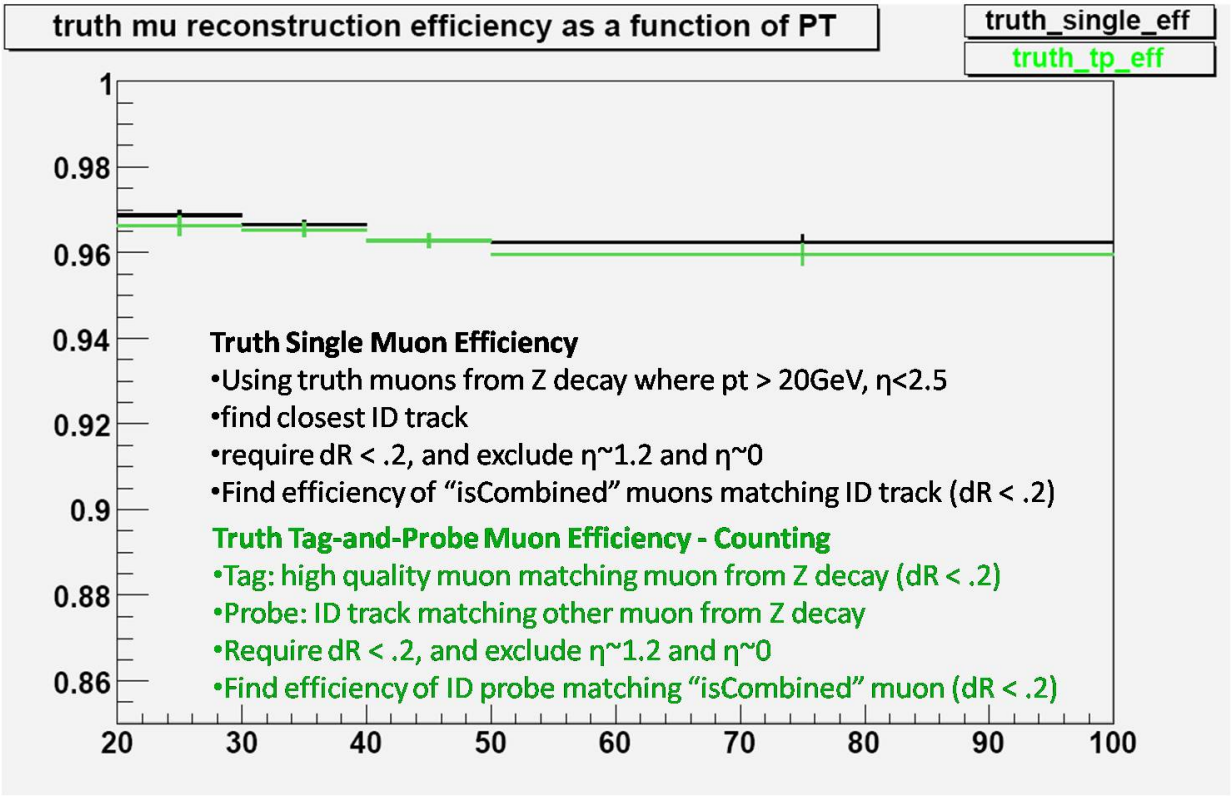

Figure 2.23: True single (black) and tag and probe (green) muon reconstruction efficiency as a function of probe p_T

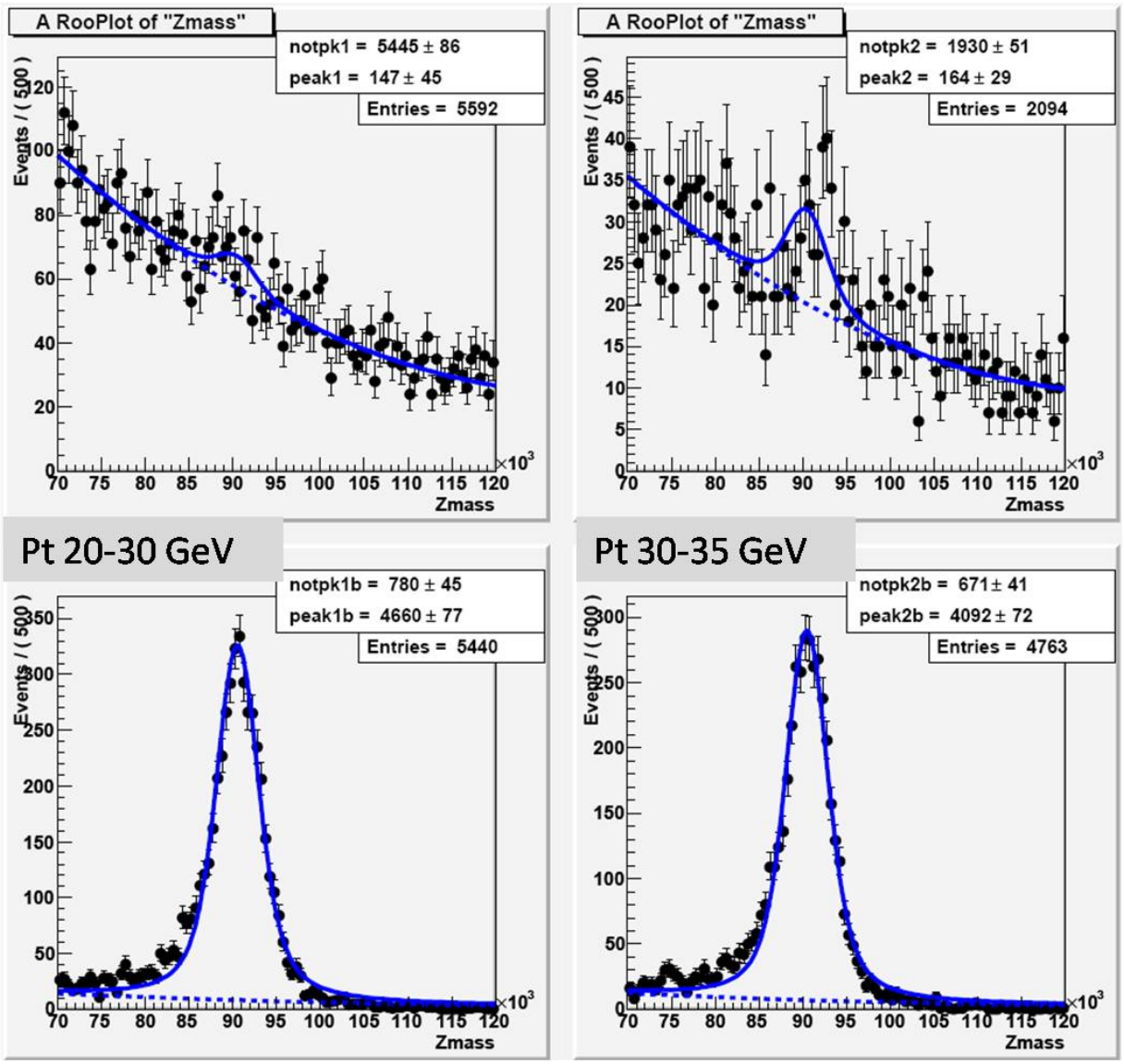

Figure 2.24: $M_{\mu\mu}$ for tag-probe pairs where probe has 20 GeV $< p_T <$ 30 GeV (left) and 30 GeV $< p_T <$ 35 GeV (right) and probe matches combined muon (bottom) or does not match combined muon (top)

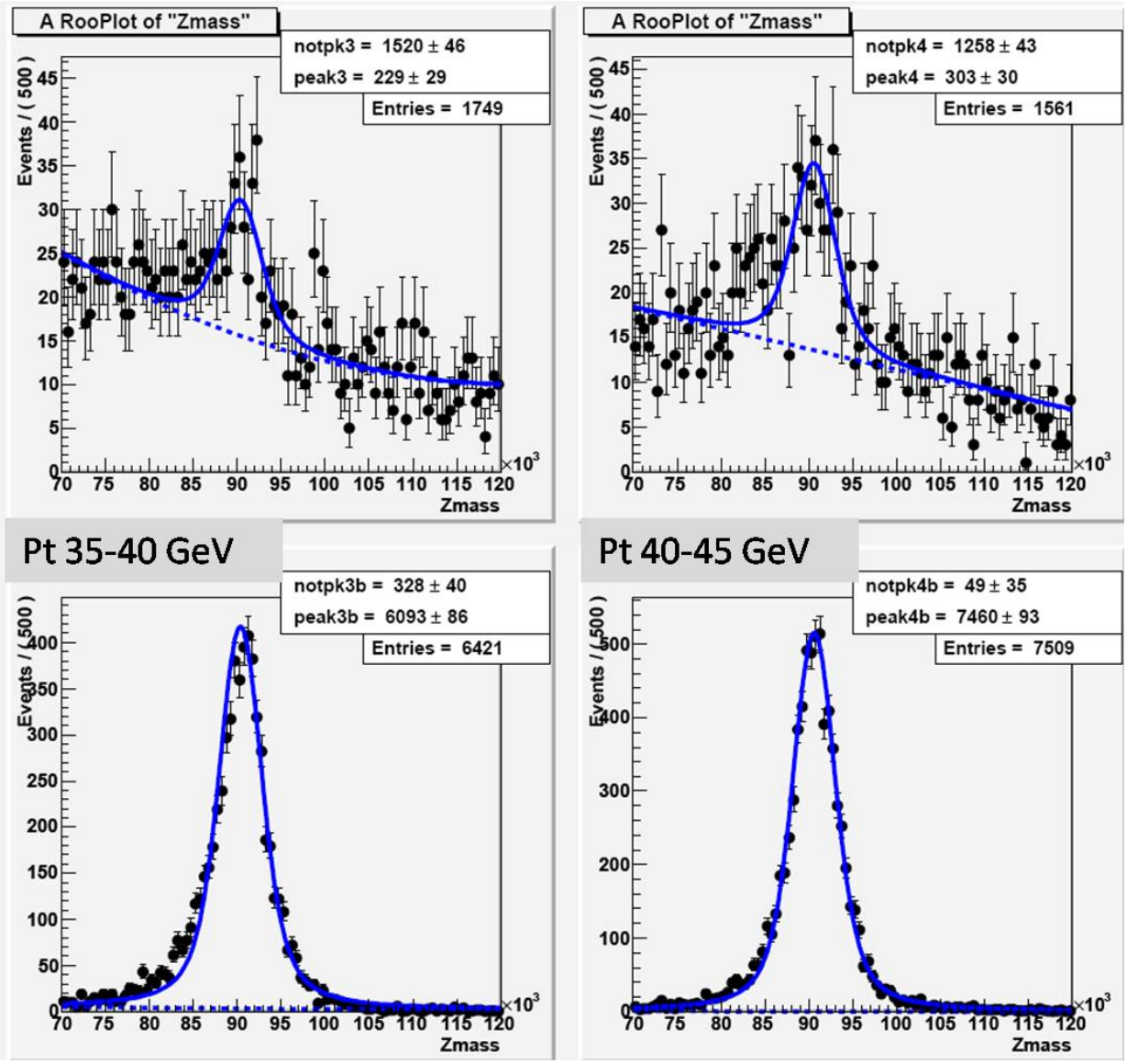

Figure 2.25: $M_{\mu\mu}$ for tag-probe pairs where probe has 35 GeV $< p_T <$ 40 GeV (left) and 40 GeV $< p_T <$ 45 GeV (right) and probe matches combined muon (bottom) or does not match combined muon (top)

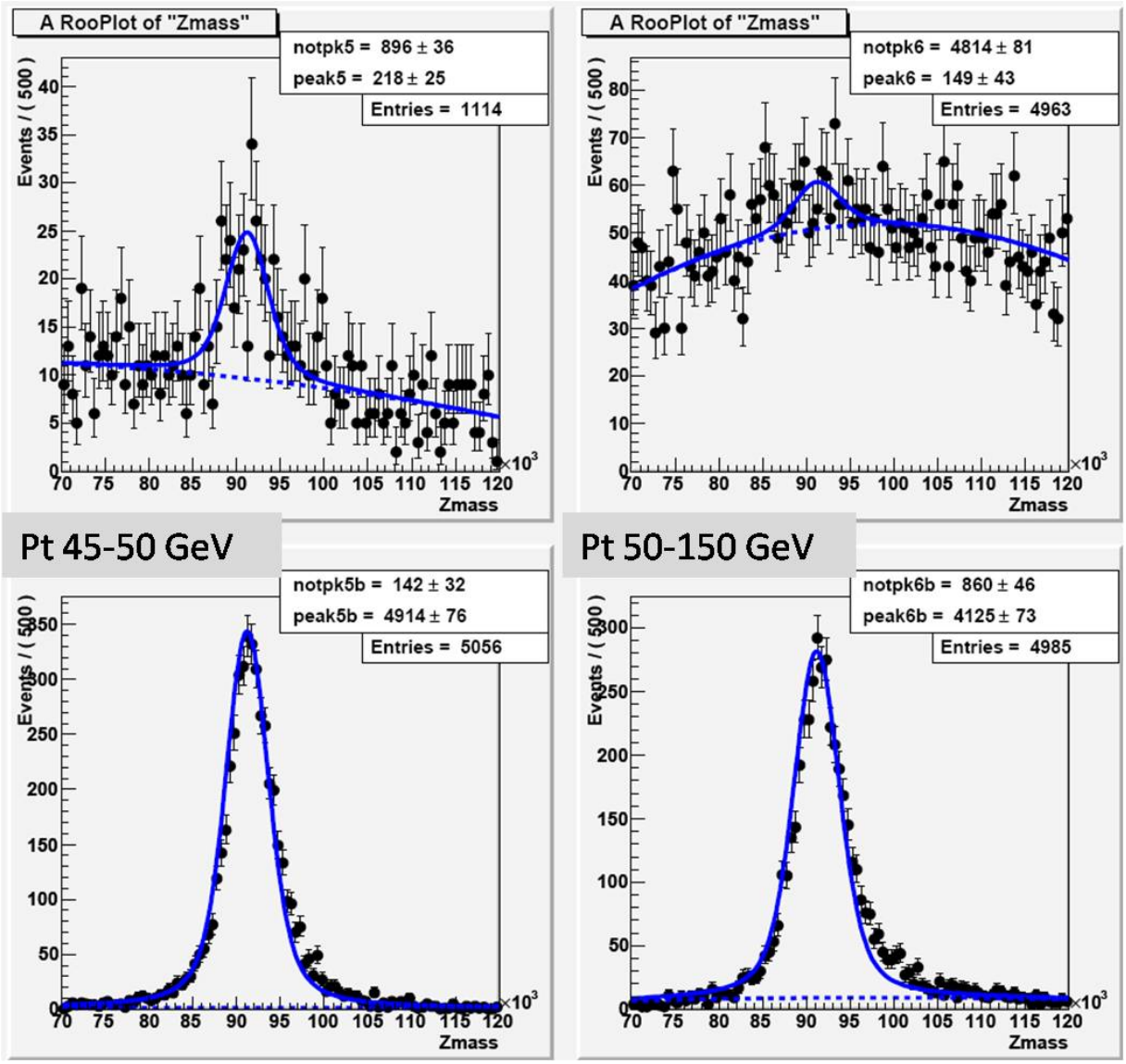

Figure 2.26: $M_{\mu\mu}$ for tag-probe pairs where probe has 45 GeV $< p_T <$ 50 GeV (left) and 50 GeV $< p_T <$ 150 GeV (right) and probe matches combined muon (bottom) or does not match combined muon (top)

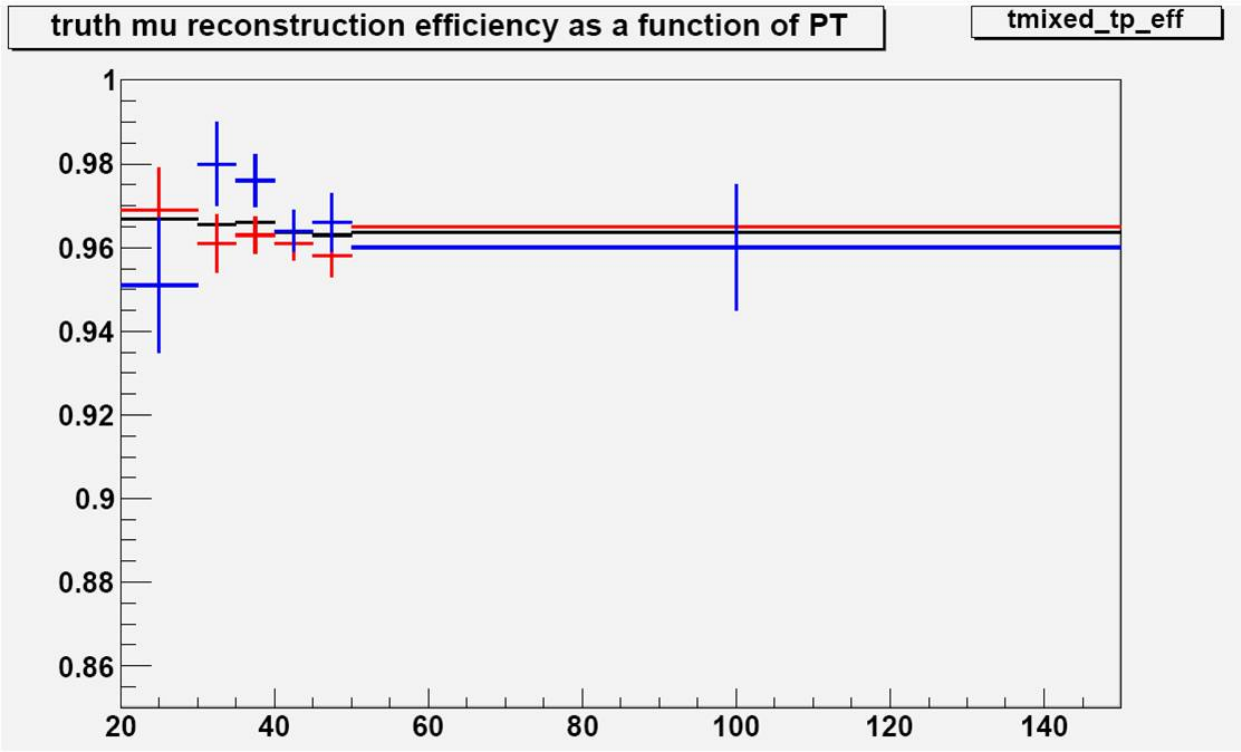

Figure 2.27: Single true muon efficiency (black), tag-and-probe muon reconstruction efficiency in Z+$t\bar{t}$ at 100 pb^{-1} (red), and tag and probe muon reconstruction efficiency in mixed MC sample of SM events in the muon channel at 150 pb^{-1}(blue)

processor (CTP), which combines the information and makes the overall LVL1 decision.

The time taken to determine and distribute the LVL1 trigger decision must be kept to a minimum, since all of the information from the detector must be stored in pipeline memories during this latency. This LVL1 latency, from proton-proton collision to LVL1 decision, is designed to be less than 2 μs. If the LVL1 trigger is passed, information is read out into readout drivers and then readout buffers. Since the pipeline memories vary widely across and even within subdetectors, and a large number of front-end electronics channels must be multiplexed to a single readout buffer, intermediate buffers called derandomizers average out the instantaneous output rates from the front-end electronics to match the bandwidth available at the input of the readout drivers. In events selected by LVL1, regions of interest (ROIs) are passed to the level-2 trigger (LVL2) containing position and p_T information for candidate objects (or energy sums in the case of missing, scalar, and vector E_T triggers). Information remains in the readout buffers until the LVL2 decision is made, so LVL2 has access to all of the event information, although generally only a small fraction is accessed in order to make the LVL2 decision. At this point, the data rate is expected to be $\sim$1 kHz, and events passing LVL2 are sent by the DAQ system to storage for Event Filter (EF) processing. This movement of information from the readout buffers to the EF is termed event building, since this is where fragments of information about the same event are assembled together in the same memory, which will be accessed by EF processors.

Rates from the calorimeters dominate total information rates, and all calorimeters are employed by the level-1 trigger in search of high p_T electrons, photons, and jets, as well as large missing and total E_T . In addition to p_T threshold requirements, isolation cuts are applied in order to trigger on possible electron, photon, or jet candidates. Layers are summed in coarse ($\Delta\eta \times \Delta\phi = 0.1 \times 0.1$) segments referred to as trigger towers. A total of 7200 tower signals are sent separately by electromagnetic and hadronic calorimeters, formed by analogue summation in the front-end electronics before transmission to the trigger system outside the detector cavern. While tile signals are sent directly to the trigger preprocessing, liquid argon calorimeter signals are sent to receiver stations, and the output of the receivers are sent to the trigger preprocessor. This enables the liquid argon calorimeter experts to analyze the analogue signals without the data acquisition system. The receiver stations were

designed, built, installed, and maintained by the University of Pittsburgh ATLAS group. All trigger tower layers are summed on the front-end electronics, except for the transition region between the barrel and end-cap calorimeters, where layers from each subdetector must be summed in the same trigger tower. These signals are summed in the receiver modules, after barrel signals are delivered from their receiver crate to the corresponding end-cap crate. The cables delivering barrel signals to the end-cap crate will correct for any relative timing difference between the two. Total energy measured in the calorimeter cells must be converted to transverse energy, which is also done in the receiver modules before being sent to the trigger preprocessor.

Eight sets of thresholds can be programmed for electron/photon triggers, with each set consisting of an E_T threshold for the cluster, an isolation threshold on the surrounding E_T in the calorimeter, and a hadron veto threshold on the E_T in the associated hadronic layers. Hadron/tau triggers have eight sets of thresholds as well, which consist of E_T and isolation thresholds. Jet triggers also have eight sets of thresholds in which the E_T in jet 'windows' are compared, where each set has a programmable E_T threshold and window size. Missing E_T (MET) scalar and vector quantities are calculated after summing all calorimeter trigger towers. Eight thresholds can be programmed for the vector MET and four thresholds for the scalar MET. The multiplicity for objects passing electron/photon, hadron/tau, and jet triggers is sent to the CTP, as well as which thresholds have passed the MET triggers.

Hit patterns from the MS trigger hardware are sent to LVL1 which searches for patterns consistent with high or low p_T muons originating from the IP. Six thresholds can be programmed for the muon system, and the multiplicities of objects passing each threshold are sent to the CTP.

Another essential role of the level-1 trigger is to identify the corresponding bunch crossing, an interval of approximately 25 ns. Since times-of-flight in the muon spectrometer and the rise-time of the LAr calorimeter pulses are comparable to 25 ns, this is not a trivial task. Although calorimeter signals are relatively slow, the final analogue signals have a very constant shape, regardless of amplitude, which allows for fairly precise timing ($\leq$ 1 ns). Signals from the muon spectrometer have intrinsically excellent timing characteristics. However, since a single muon may travel for longer than a single bunch crossing within the

spectrometer, careful calibration of the muon system is required and must be done with real collisions. All bunch crossings occurring during the LVL1 latency (∼50 bunch crossings) must be stored in the detector information pipelines, so subsystems have access to all the information required to assign candidates to the proper beam crossing [17].

2.6.1 Trigger Performance in Early Data

Due to the low luminosity running of the LHC in the first year of data collection, demands on the LVL1 trigger system are greatly reduced. Particularly for muon triggers, which are used in the following leptoquark analysis, rates are such that the lowest threshold requirements are acceptable and will not require prescaling. In the case of muon triggers, offline trigger reconstruction efficiency can be calculated using events where two muon objects have been reconstructed. In such events, the tag-and-probe trigger efficiency can be calculated as a function of position and p_T . This trigger efficiency with respect to reconstruction will be discussed in more detail in section 4.5.1.

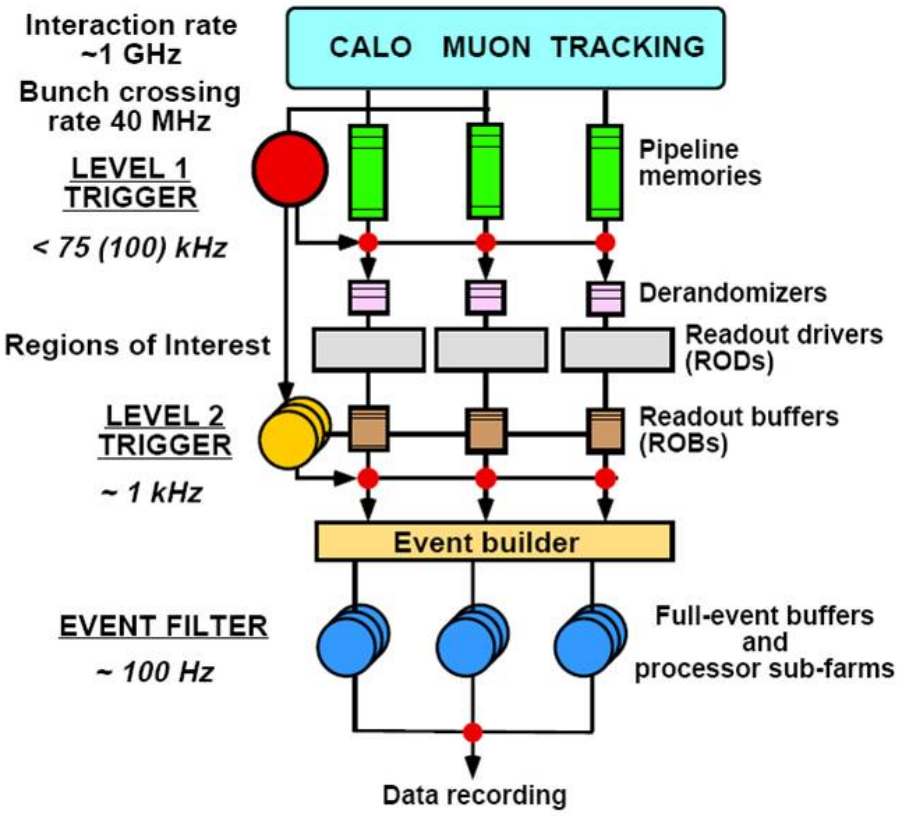

Figure 2.28: Diagram of ATLAS dataflow and information rates at various stages of data acquisition

3.0 SIMULATION OF DETECTOR RESPONSE

The ATLAS simulation can be considered in three separate stages, event generation, detector simulation, and digitization. Monte Carlo event generators provide the physics calculations for the primary interactions, essentially providing the event topology for an ideal detector. GEANT [18] is then used to propagate particles through the detector, interacting with material along the way. Information about the response of sensitive materials is then used to simulate the digitized response of the ATLAS subdetectors during data acquisition. While simulating an experiment of this size, a wide range of energy levels and physics processes must be included. Ideally, interactions ranging from the eV scale (i.e. ionization energy of active gases in some detectors) to the TeV scale (i.e. catastrophic bremsstrahlung of muons in the calorimeters) would be encompassed by the simulation, but time constraints require a much more economic use of computing power. Detector simulation consumes the most CPU time, due to the demanding task of simulating showers in the calorimeters. Although several "fast simulation" alternatives have been developed to allow for the production of large datasets in a short time (as will be required by high statistics studies), the analyses presented here are based on the fully simulated detector response [19].

3.1 EVENT GENERATION

Several different Monte Carlo event generators, such as Pythia [20], MC@NLO [21], and Herwig [22], are used to simulate the physics processes that produce the slew of particles following pp collisions. Each generator simulates a final state given by a particular model of the underlying physics, and although each generator is different in its implementation, the

underlying principles are often the same. Pythia is one of the more detailed examples in its exhaustive treatment of hadronic interactions. Therefore the following discussion will be specific to Pythia event generation.

The initial hard process is given by the parton interaction between quarks and/or gluons from incoming proton beams and is calculated in perturbative QCD using initial states given by the parton distribution functions (PDFs) of the incoming protons. Initial state radiation from a parton in each beam triggers an initial-state parton shower, and partons from each shower interact in the hard process. Elementary particles emerging from the hard process begin the final state parton showers, giving off QCD radiation that will participate in the basic scattering processes of the event. Additional semi-hard processes from other partons in the incoming protons, or beam fragments, may also occur and are referred to as the "underlying event'. These parton showers continue until some energy cutoff is reached, when finally, the quarks and gluons must be hadronized into colorless mesons and baryons [20].

3.1.1 Initial and Final State Radiation

In any process involving particles with color or electric charge, corrections from photon or gluon radiation in the initial and final states can become quite large. One may calculate these corrections exactly using matrix elements, calculating Feynman diagrams order by order, but this becomes increasingly difficult at higher orders. Another option is the parton shower method, which approximates the full matrix element by simplifying kinematics, interference, and helicity structure. The branchings of one parton into two (or more) are combined to build jets. Generally speaking, first order matrix elements are generated and then complemented with parton showers to describe softer radiation.

Parton showers describe electromagnetic and QCD initial- and final-state radiation and develop according to a branching structure $a \to bc$, i.e. $e \to e\gamma, q \to q\gamma, q \to qg, g \to gg, g \to q\bar{q}$. Branching rates for each process, $a \to bc$, are characterized by a splitting function $P_{a\to bc}(z)$, where z describes the energy sharing of daughter particles. Daughter particles are then allowed to branch, and the parton shower begins to develop, with each parton

characterized by some virtuality, Q^2, which is m^2 of the branching parton and determines the time ordering of the shower. The shower is limited such that at some Q^2_{max}, the shower is matched to the hard process, and at some Q^2_{min}, where QCD is no longer perturbative ($\sim$1 GeV), the shower is cut off and hadronization begins.

Final-state showers evolve in time (i.e. parton $Q^2 = m^2 > 0$) and with decreasing Q^2. Beginning with Q^2_{max}, a parton from the hard process branches, with the Q^2 of the branched parton determined by the energy splitting in the kernel function. Daughters may now branch also, and so on until the Q^2_{min} cutoff is reached.

Initial-state shower evolution is space-like. An incoming parton may initiate a shower where each branching parton becomes increasingly off mass shell, according to some allowed range of virtuality determined by the energy of the parton, and these virtual particles may interact in the hard process. In the branching that leads from the initiator parton to the parton that participates in the hard process, i.e. $q \to q'g$, q and q' have $m^2 < 0$. The shower is developed in a backward evolution with decreasing $Q^2 = -m^2 > 0$ from the hard process to the initiator parton. Space-like partons in the initial-state shower may interact in the hard process and also develop a time-like evolution as in final-state showers [20].

3.1.2 Beam Remnants

In proton-proton collisions, the initial-state shower develops from an initiator in each proton, but the remnant still carries a significant fraction of the original energy. This beam fragment is color-connected to the initiator and the hard process, so it is part of the same hadronization system. In addition, beam remnants may contribute interactions other than those resulting from the two initiator partons. Pythia accounts for the $2 \to 2$ scattering processes from beam remnants, which builds the underlying event [20].

3.1.3 Hadronization

Numerical simulation of QCD perturbation theory is handled by the parton showers described previously, but as the energy of the constituent partons decreases below the threshold Q^2_{min} $\sim$1 GeV, QCD becomes strongly interacting and perturbation theory is no longer valid.

Color confinement requires that these colored partons be transformed into colorless hadrons, either recombining with each other or interacting with sea particles in the process known as hadronization. The process that renders the shower colorless is not understood from first principles, i.e. the QCD Lagrangian, but several phenomenological models exist. All of them are probabilistic and iterative, therefore relying on only a few simple branchings, i.e. jet $\rightarrow$ hadron+remainder-jet. Pythia adopts the string fragmentation model, or the Lund model (string $\rightarrow$ hadron+remainder-string), for this process. For example, consider a 2-jet system $q\bar{q}$. As a starting point for the string fragmentation model, assume linear confinement such that the energy stored in color dipole field between the two charges increases linearly with their separation, about 1GeV/fm. Consider a color flux tube stretched between the partons, with transverse dimensions of QCD scale ($\sim$1 fm), where the mathematical, one-dimensional string parameterizes its axis. The energy stored in the string increases, and the string may break with the production of a $q'\bar{q}'$ pair, resulting $q\bar{q}'\bar{q}q'$ color-singlets, which may fragment further with some energy threshold. String breaks will continue until only on-mass-shell hadrons remain, each corresponding to a piece of string with a quark in one end and an antiquark in the other. With each step, a fraction of the original energy is used to produce the $q'\bar{q}'$ until all available energy is used, with some small modifications at the end to arrive at the correct total energy and momentum for the system.

The Lund model employs quantum mechanical tunneling to produce the $q\bar{q}'\bar{q}q'$ pairs from string breaks, resulting in a Gaussian spectrum for their p_T , regardless of flavor. This p_T is balanced between the $q\bar{q}$ produced in the string break, roughly resulting in a cone shape for the evolving jet. Tunneling also suppresses heavy-quark production, with u:d:s:c $\approx$ 1:1:0.3:10^{-11}, such that charm, top, and bottom quarks are produced only in hard processes and the perturbative parton showers (g $\rightarrow$ $q\bar{q}$). When a quark-antiquark pair combine, an algorithm chooses between scalar and vector mesons with a 1:3 ratio for spin multiplicity, multiplied by some wavefunction normalization factor that will favor lighter states. Baryon formation is similar to meson formation with the exception of replacing the initial quark-antiquark with a diquark-antidiquark and proceeding with the hadronization described previously [20].

3.2 DETECTOR SIMULATION AND DIGITIZATION

Particles as documented by the event generation are now propagated through the detector using GEANT. Naturally, the efficiency of computing power in this step is largely determined by the level of detail in the geometry description of the detector, and it is a constant compromise between accuracy and performance. Particle momenta, as given by the event generation step, are provided to GEANT which will track them through the various subdetectors, recording information about interactions in sensitive elements along the way (i.e. light produced in scintillating plastic, dE/dx in silicon or active gases) in the GEANT HITS banks. Hit-types are predefined along with information needed to digitize the response for HITS in a particular sensitive volume. So, for example, the HITS bank would consist of hit positions for trackers and energy deposits for calorimeters. At this point, only the physics processes that produce the particles and the physical material in the ATLAS detector description have been accounted for, with no regard to the readout systems in the data acquisition phase. It is at this level that HITS banks for different events can be added together to simulate pile-up in the detector.

Finally, information from the HITS in the simulation stage is processed to simulate the detector output from the readout electronics and is recorded in GEANT DIGI hits for input into the reconstruction programs. At this stage, effects of changes in electronic readout can be studied, additional noise can be added to the signals, etc.

At this point, simulated datasets can be treated as real data, and after reconstruction algorithms are applied, analysis data is produced in two formats, event summary data (ESD) and analysis object data (AOD). ESD datasets contain detailed output from reconstruction algorithms as well as the raw data input, such that ESDs can be used to test and re-tune reconstruction algorithms. AODs are produced from ESDs and are a summary of the reconstructed event, requiring only 20% of the disk space needed for ESDs. They contain enough information to perform physics analyses, but not enough information to re-run reconstruction algorithms. Finally, various analysis groups produce their own derived physics data, or DPDs, which take only analysis-specific information from ESD or AOD datasets. DPD datasets are generally produced once and moved a local disk, the goal being reduced demand

on GRID resources from analysis jobs [19].

3.3 PARAMETERIZATIONS FOR FAST SIMULATION

In the year leading up to the initial turn-on of the LHC, it became apparent that global computing resources were insufficient to produce the amount of Monte Carlo needed for high statistics studies. Fast alternatives to the simulation step described above generally involve a parameterization of the detector response, which is used to smear truth particles' energy and momentum according to some resolution function, which varies as a function of position and energy. ATLFAST-II was an attempt to reach a compromise between the full simulation and a fully parameterized fast simulation.

In the spring of 2008, ATLFAST-II consisted of the fully simulated response of the ATLAS detector, except in the calorimeters, where a parameterization was applied. Since simulating the showers in calorimeters consumes a significant portion of the total time taken to simulate a full event, such a method was able to decrease the simulation time by a factor of 10 compared to the full simulation. In contrast, the fully parameterized ATLFAST-I delivers a factor of 50 increase in performance. While still in development, it became apparent that the relative p_T resolution for high p_T egamma objects suffered a shift in the mean resolution that varied as a function of both position and p_T . This shift can be seen in the relative p_T resolution as a function of η in Figure 3.1, where the blue distribution represents the fully simulated response of the ATLAS detector, and the red distribution represents ATLFAST-II. If limited ranges of η and p_T were considered, the relative resolution function became Gaussian again, only with a mean shifted up to more than a full standard deviation from zero. In order to correct for this shift in resolution, the "good barrel" region ($|\eta| < 0.75$) was divided into 10 sections, and the end-cap was considered in its entirety ($1.6 < |\eta| < 2.5$). Two more regions that showed large difference are the so-called "crack" region between the barrel and end-cap LArg calorimeters about $|\eta| \sim 1.5$, and the "tile gap" at $|\eta| \sim 0.8$, where the central barrel tile calorimeter transitions to the extended tile barrel. These regions were not considered due to the fact that the geometry descriptions used for these areas in ATLFAST-

II were out of date. In each of these η regions, egamma objects were separated into 7 bins of p_T for all objects with $p_T \geq 20$ GeV. Finally, the relative p_T resolution distribution in each η-p_T bin was fit to a Gaussian. The mean of each Gaussian fit was plotted as a function of $|\eta|$ for these 7 p_T ranges, as seen in Figure 3.2. The shift in the mean for each p_T range, as a function of η, was fit to a line, yielding the final correction needed as a function of η and p_T . For $|\eta| < 0.75$:

$$\text{correction}(\eta, p_T) = a(p_T) * \eta + b(p_T) \tag{3.1}$$

$$a(p_T) = 0.01664 + 2.198 \times 10^{-5} p_T \tag{3.2}$$

$$b(p_T) = -0.0279 - 1.142 \times 10^{-5} p_T \tag{3.3}$$

In the endcap, the shift in resolution was only p_T dependent, requiring a correction of:

$$\text{correction}(p_T) = -0.0206 + 6.436 \times 10^{-6} p_T \tag{3.4}$$

Finally, these parameterized corrections were applied to the truth particles' p_T , and the resulting relative p_T resolution agrees with the full simulation, as shown in Figures 3.3 and 3.4.

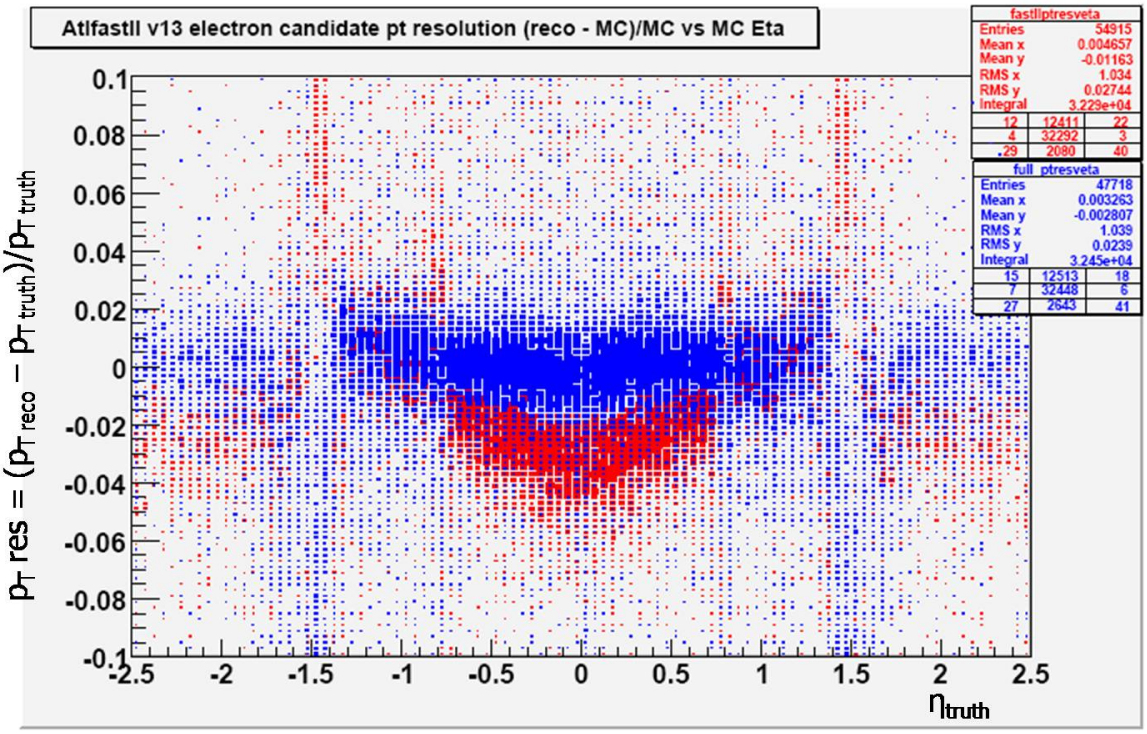

Figure 3.1: Relative p_T resolution of egamma objects vs. η in fully simulated events (blue) and ATLFAST-II events (red).

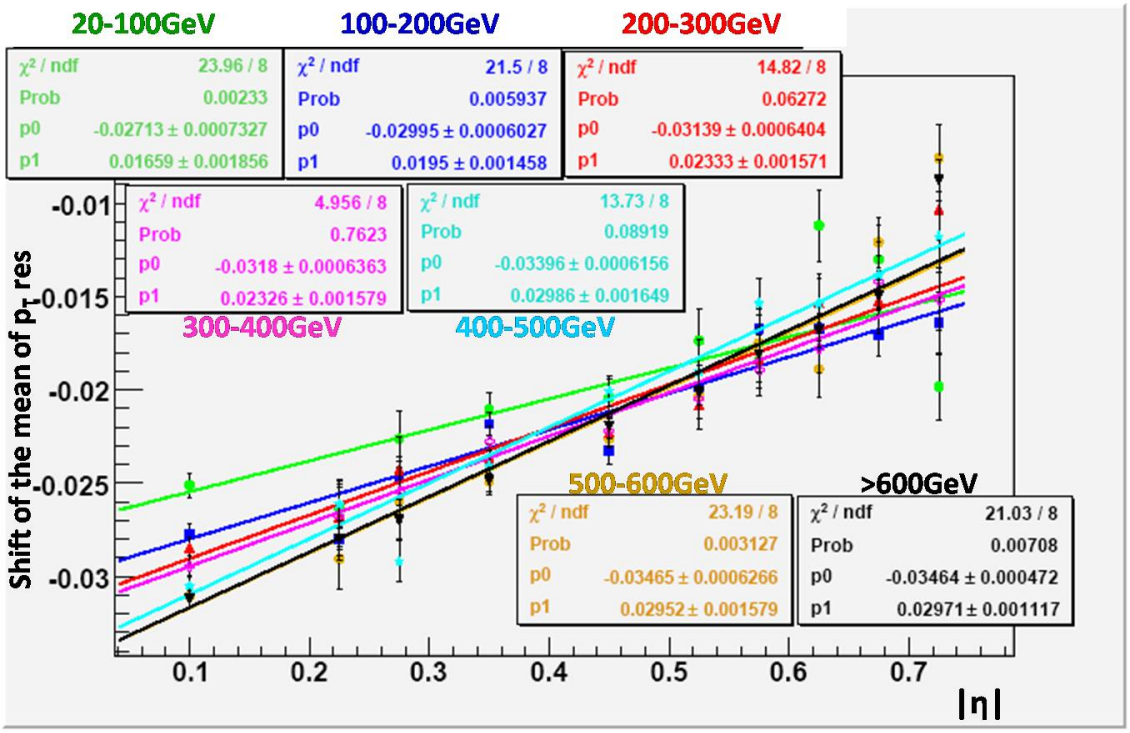

Figure 3.2: Shift from zero of the mean in the Gaussian relative p_T resolution of egamma objects as a function of η in 7 p_T ranges in ATLFAST-II simulated events.

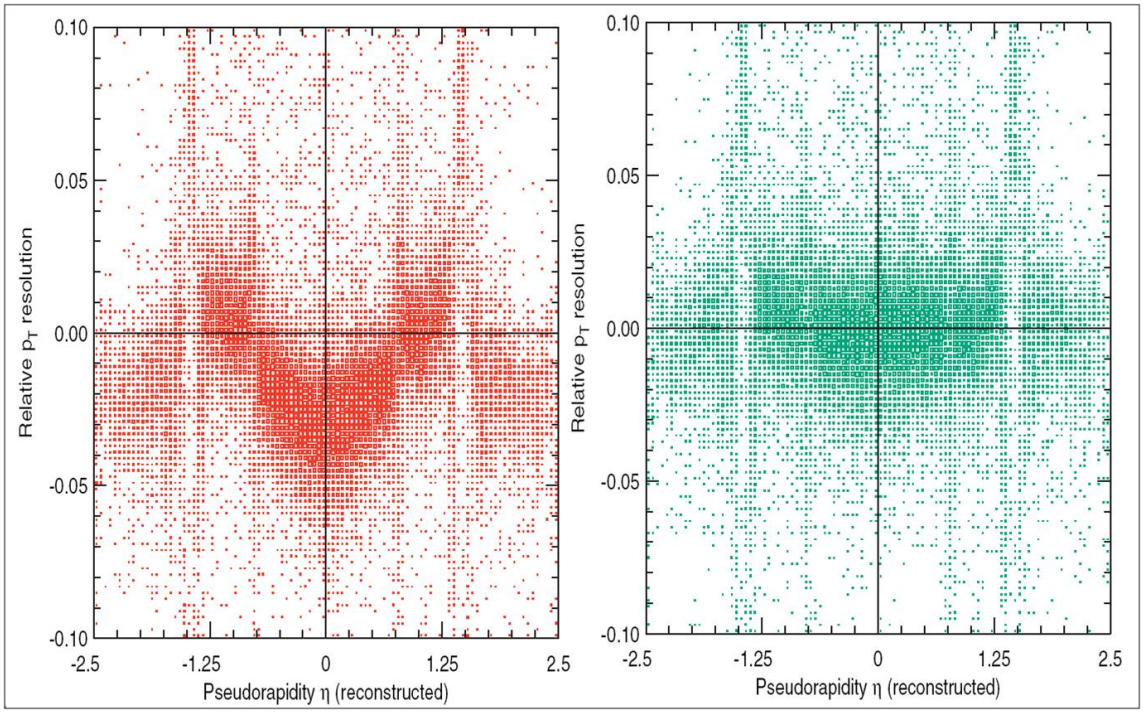

Figure 3.3: Relative p_T resolution of egamma objects vs. η in ATLFAST-II events before correction is applied (left) and after (right).

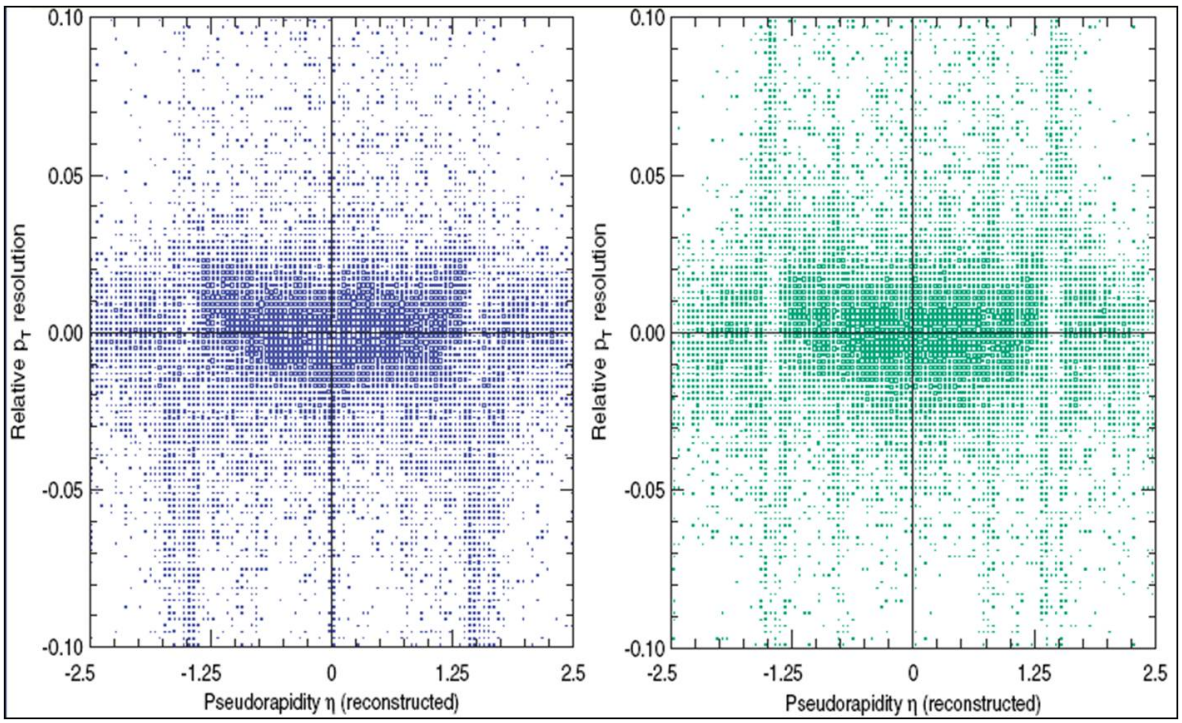

Figure 3.4: Relative p_T resolution of egamma objects vs. η in fully simulated events (left) and ATLFAST-II events after correction is applied (right).

4.0 LEPTOQUARK ANALYSIS

In the Standard Model (SM), leptons and quarks appear as independent fields, but there are indications of a more intimate relationship. For example, the SM would not be consistent without the cancellation of lepton and quark contributions to triangle anomalies of gauge currents, suggesting that the two types of fermionic matter could be unified in a single multiplet [1]. In the framework of Grand Unified Theories (GUTs), theoretical bosons called leptoquarks mediate transitions between leptons and quarks. Such particles appear naturally in all unified theories such as SU(5), Pati-Salam SU(4), supersymmetric extensions to the SM, as well as compositeness models, and more.

In general, leptoquark interactions need not conserve baryon number. However, baryon number violating leptoquarks can have two undesirable results: rapid proton decay and flavor changing neutral currents. Since both are constrained by experiment, such leptoquarks must be very heavy ($\geq$10 TeV) in order to be consistent with current limits and would not be accessible at the LHC. However, if leptoquarks do not couple to quark-quark, leptoquarks could be as light as a few hundred GeV without causing rapid proton decay. In addition, if leptoquark couplings are flavor diagonal, there are no leptoquark mediated flavor changing neutral currents. Consequently, leptoquark species are often designated by the generation of fermions that they couple to, and the following analysis will concentrate on second generation leptoquarks decaying to dimuon+dijet final states.

In such scenarios, leptoquarks could have masses accessible at the LHC, and the production processes are shown in Figure 4.1. Proton-proton collisions allow leptoquark pair production via gluon fusion, a process that is independent of the leptoquark-lepton-quark Yukawa coupling λ and the leptoquark generation. This process, with a cross section depending only on the strong coupling, leptoquark mass, and center of mass energy of the collider,

dominates the cross section for leptoquark production and is essentially model independent. ATLAS would be sensitive to such leptoquarks even within the first year of continuous data collection.

In addition to pair production, single leptoquarks could also be produced at the LHC, as shown in Figure 4.1. However, reconstructing single leptoquark events requires a different approach. Since the production mechanism for single leptoquarks requires a second generation sea quark from one of the incoming protons, and the cross section is proportional to λ^2, the total cross section will be dominated by the contribution from scalar leptoquark pairs. Consequently, only leptoquark pair events are considered here.

In the following analysis, high p_T dimuon+dijet final states are examined to quantify any excess compared to what is expected from SM processes. All results are a function of the branching ratio $\beta(LQ \to \mu q)$, and for a given branching fraction, the signal cross section for this analysis becomes $\beta^2 \sigma_{LQ}$. Signal event candidates are selected by requiring two high p_T muons and two high p_T jets. A leptoquark candidate is reconstructed by adding the four momenta of a muon and jet. Since there are two possible ways to combine the final state particles, the combination which yields the smallest difference between the two reconstructed leptoquark candidate masses is selected (i.e. $|(M_{\mu 1 j 1} - M_{\mu 2 j 2})| < |(M_{\mu 1 j 2} - M_{\mu 2 j 1})|$). This method of reconstruction was chosen because, although it creates a bias toward similar reconstructed mass in the two leptoquark candidates, it does not create a bias toward *higher* reconstructed mass where signal is expected.

4.1 LEPTOQUARK MODEL

The leptoquark model from Buchmuller, Ruckl, and Wyler is commonly used to classify potential leptoquark species. Such BRW leptoquarks couple to a single generation of fermions via chiral Yukawa couplings which are invariant under SU(3) X SU(2) X U(1), and interactions conserve baryon and lepton numbers [23]. Although leptoquarks are predicted by many BSM scenarios, the analysis presented here seeks to be as general as possible, searching for the phenomenological effects of a high mass resonance that decays to lepton-quark.

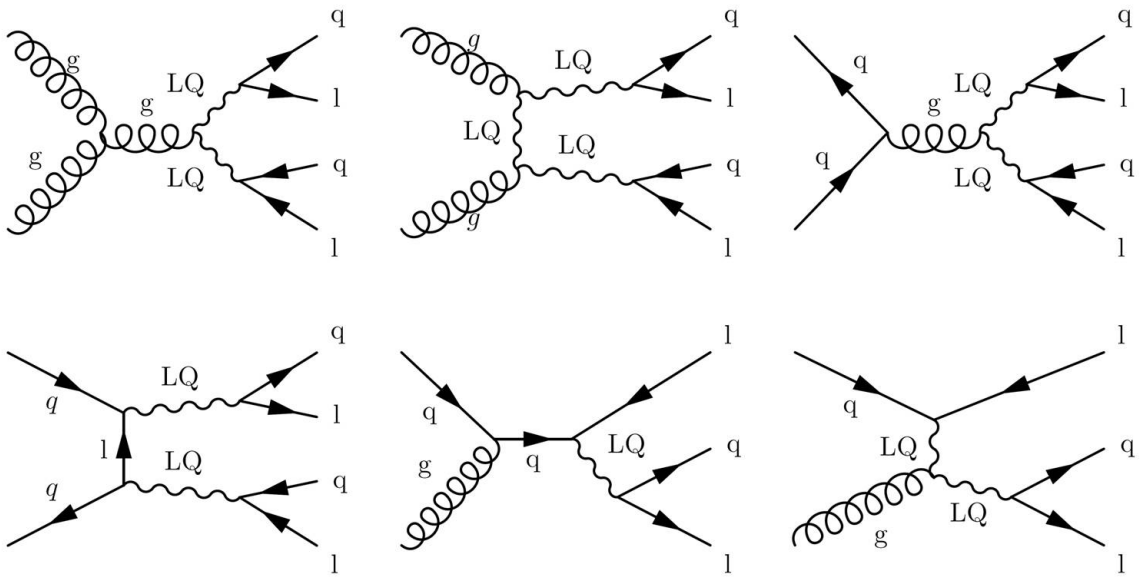

Figure 4.1: Feynman diagrams for leptoquark production at the LHC

Since leptoquark production at the LHC would be dominated by pair production via strong interactions, the BRW model provides a sufficiently general framework to study possible leptoquark production in ATLAS. The Lagrangian used to calculate the leptoquark pair production cross section is given by:

$$\mathcal{L} = \mathcal{L}^f_{|F|=0} + \mathcal{L}^f_{|F|=2} + \mathcal{L}^V \tag{4.1}$$

where the lagrangian is separated into two fermionic parts and one bosonic part. The Yukawa type leptoquark interactions with fermion number (F=3B + L) equal to 0 or ± 2 are given by:

$$\begin{aligned}\mathcal{L}^f_{|F|=0} = (h_{2L}\bar{c}_R l_L + h_{2R}\bar{q}_L i\tau_2 \mu_R)R_2 + \tilde{h}_{2L}\bar{s}_R l_L \tilde{R}_2 + (h_{1L}\bar{q}_L l_L + \\ h_{1R}\bar{s}_R \gamma^\sigma \mu_R)U_{1\sigma} + \tilde{h}_{1R}\bar{c}_R \gamma^\sigma \mu_R U_{1\sigma} + h_{3L}\bar{q}_L \vec{\tau}\gamma^\sigma l_L \vec{U}_{3\sigma} + h.c.\end{aligned} \tag{4.2}$$

$$\begin{aligned}\mathcal{L}^f_{|F|=2} = (g_{1L}\bar{q}^c_L i\tau_2 l_L + g_{1R}\bar{c}^c_R \mu_R)S_1 + \tilde{g}_{1R}\bar{s}^c_R \mu_R \tilde{S}_1 + g_{3L}\bar{q}^c_L i\tau_2 \vec{\tau} l_L \vec{S}_3 \\ +(g_{2L}\bar{s}^c_R \gamma^\sigma l_L + g_{2R}\bar{q}^c_L \gamma^\sigma \mu_R)V_{2\sigma} + \tilde{g}_{2R}\bar{c}^c_R \gamma^\sigma l_L \tilde{V}_2 \sigma + h.c.\end{aligned} \tag{4.3}$$

where τ_i are Pauli matrices, q_L and l_L are $SU(2)_L$ doublets, c_R, s_R, and μ_R are singlet fields, and the Yukawa couplings of leptoquarks to lepton-quark fields are given by $g_{1(L,R)}$, $\tilde{g}_{1R}$, g_{3L}, $h_{2(L,R)}$, and $\tilde{h}_{2L}$. The different leptoquark fields and their corresponding couplings and quantum numbers are summarized in Table 4.1.

Leptoquark interactions with gauge bosons are dominated by gluon contributions, so the U(1) X SU(2) part of gauge interactions are omitted here. The gauge interaction in SU(3) can be divided into scalar and vector leptoquark contributions as follows:

$$\mathcal{L}_S^g = \sum_{scalars} [(D_{ij}^{\mu}\Phi^j)^{\dagger}(D_{\mu}^{ik}\Phi_k) - M_S^2\Phi^{i\dagger}\Phi_i] \tag{4.4}$$

$$\begin{aligned}\mathcal{L}_V^g = \sum_{vectors} (\frac{1}{2}V_{\mu\nu}^{i\dagger}V_i^{\mu\nu} + M_V^2\Phi_{\mu}^{i\dagger}\Phi_i^{\mu} - ig_s[(1-\kappa_G)\Phi_{\mu}^{i\dagger}t_{ij}^a\Phi_{\nu}^j\mathcal{G}_a^{\mu\nu} \\ + \frac{\lambda_G}{M_V^2}V_{\sigma\mu}^{i\dagger}t_{ij}^aV_{\nu}^{j\mu}\mathcal{G}_a^{\nu\sigma}])\end{aligned} \tag{4.5}$$

where g_s is the strong coupling, t_a are the generators of $\mathrm{SU}(3)_c$, M_S and M_V are the scalar (vector) leptoquark masses, κ_G and λ_G are the anomalous couplings of anomalous magnetic and quadrupole moments of vector leptoquarks, and $\Phi(\Phi^{\mu})$ are scalar (vector) leptoquark fields. The gluon field tensor is given by

$$\mathcal{G}_{\mu\nu}^a = \partial_{\mu}G_{\nu}^a - \partial_{\nu}G_{\mu}^a + g_s f^{abc}G_{\mu b}G_{\nu c}. \tag{4.6}$$

Vector leptoquark field tensors are

$$V_{\mu\nu}^i = D_{\mu}^{ik}\Phi_{\nu k} - D_{\mu}^{ik}\Phi_{\nu k}, \tag{4.7}$$

where the covariant derivative is

$$D_{\mu}^{ij} = \partial_{\mu}\delta^{ij} - ig_s t_a^{ij}G_{\mu}^a. \tag{4.8}$$

This model has been implemented in CompHEP and CalcHEP [24], and agrees with leading order calculations from [25].

LQ	Spin	F	Color	T_3	Q_{em}	$\lambda_L(lq)$	$\lambda_R(lq)$	$\lambda_L(\nu q)$
S_1	0	-2	$\bar{3}$	0	+1/3	g_{1L}	g_{1R}	$-g_{1L}$
$\tilde{S}_1$	0	-2	$\bar{3}$	0	+4/3	0	$\tilde{g}_{1R}$	0
$\vec{S}_3$	0	-2	$\bar{3}$	+1 0 -1	+4/3 +1/3 -2/3	$-\sqrt{2}g_{3L}$ $-g_{3L}$ 0	0 0 0	0 $-g_{3L}$ $\sqrt{2}g_{3L}$
R_2	0	0	3	+1/2 -1/2	+5/3 +2/3	h_{2L} 0	h_{2R} $-h_{2R}$	0 h_{2L}
$\tilde{R}_2$	0	0	3	+1/2 -1/2	+2/3 -1/3	$\tilde{h}_{2L}$ 0	0 0	0 $\tilde{h}_{2L}$
$V_{2\mu}$	1	-2	$\bar{3}$	+1/2 -1/2	+4/3 +1/3	g_{2L} 0	g_{2R} g_{2R}	0 g_{2L}
$\tilde{V_{2\mu}}$	1	-2	$\bar{3}$	+1/2 -1/2	+1/3 -2/3	$\tilde{g}_{2L}$ 0	0 0	0 $\tilde{g}_{2L}$
$U_{1\mu}$	1	0	3	0	+2/3	h_{1L}	h_{1R}	h_{1L}
$\tilde{U_{1\mu}}$	1	0	3	0	+5/3	0	$\tilde{h}_{1R}$	0
$\vec{U_{3\mu}}$	1	0	3	+1 0 -1	+5/3 +2/3 -1/3	$\sqrt{2}h_{3L}$ $-h_{3L}$ 0	0 0 0	0 h_{3L} $\sqrt{2}h_{3L}$

Table 4.1: Quantum numbers for the Leptoquark fields appearing in the Lagrangian in Eq. 4.2, 4.3, 4.4, and 4.5

4.2 CURRENT LIMITS

Tevatron experiments have produced limits on leptoquark masses, based on studies of $p\bar{p}$ collisions at 1.96 TeV center of mass energy. The CDF and D0 experiments have analyzed 198 pb^{-1} and 1.0 fb^{-1}, respectively, for second generation leptoquark pair production in the $\mu\mu jj$ and $\mu\nu jj$ channels, obtaining limits on the leptoquark mass as a function of the branching fraction for a leptoquark to decay to a charged lepton and quark, $\beta(LQ \to \mu q)$. For β=1, CDF and D0 have excluded second generation leptoquark masses up to 226 GeV and 316 GeV, respectively, at a confidence level of 95% [26, 27].

Many leptoquark analyses from HERA experiments have also been published, searching for various effects associated with leptoquark production. Since HERA is an ep collider, possible leptoquark production is limited to first generation. In addition, leptoquark production mechanisms are dependent on the lepton-quark-leptoquark coupling λ. As a result, HERA experiments are able to extract limits on the leptoquark mass as a function of λ. Even for Yukawa couplings of $\lambda = 0.1$, HERA experiments have excluded first generation leptoquarks with masses of approximately 275 GeV at 95% CL [28, 29].

4.3 SIMULATION OF LEPTOQUARK SIGNAL

Studies presented here are limited to second generation leptoquark pair production. Although the Yukawa couplings of different generations of leptoquarks will likely vary, the dominant contributions to the production cross sections are independent of such a coupling. Therefore, differences in discovery potential between generations is primarily affected by particle reconstruction efficiencies that vary among the three generations of leptons. In addition, depending on the nature of the analysis, resolution effects from reconstruction would differ between the electron channel and the muon channel, for example. The width of the reconstructed leptoquark mass resolution should be dominated by detector and reconstruction effects (rather than the Yukawa coupling λ), and combinatorial effects associated with reconstructing the leptoquark pair, which will be discussed in more detail in Section 4.7.

M_{LQ} [GeV]	cross section [pb]
200	0.123E+02
300	0.125E+01
400	0.211E+00
500	0.470E−01
600	0.125E−01
800	0.121E−02
1200	0.204E−04

Table 4.2: Leptoquark pair production cross sections for pp collisions at center of mass energy of 7 TeV

Four leptoquark mass points, which may be accessible with the first few hundred inverse picobarns of LHC data, are examined. Pair production cross sections, found in Table 4.2, were calculated according the the BRW model at next-to-leading order as in [25], using the renormalization and factorization scale, $\mu = M_{LQ}$, and NLO parton distribution functions CTEQ6M.

Individual events were generated using Pythia, the output of which is sent through simulation and digitization as described in previous sections. Although the leptoquark is likely to undergo color interactions before decay, this effect is not simulated as it presents additional complexity in computation and should not significantly affect the resulting analysis [30]. Within Pythia, the leptoquark is treated as a resonance and decays as a contact interaction in order to avoid complications in the hadronization phase. Pythia samples were simulated using the MRST parton distribution function, which uses the leading order (LO) parton matrix element with a combination of LO and next-to-leading-order (NLO) parton distributions as discussed in [31].

4.4 SIMULATION OF SM BACKGROUNDS

Since the primary event signature for leptoquark pair production is two final-state, high p_T muons, the dominant SM backgrounds are $t\bar{t}$, Z/Drell-Yan (Z/DY), and diboson events. Other background sources considered here are single top, W+jets, and QCD events, although their contribution to the signal region was found to be small. All backgrounds, excluding QCD, were studied using a sample corresponding to 163.5 pb^{-1} of integrated luminosity for pp collisions at 7 TeV center of mass energy. Streaming algorithms were then applied to obtain a Monte Carlo sample that resembles, as much as possible, data from the muon stream. The original dataset (before streaming) contained samples from other leptonic channels also (i.e. electron, tau). However, the cross section information given below refers only to the muon contribution of such processes, although a few events from other lepton generation samples may make it into the muon stream.

The QCD sample analyzed here corresponds to only 0.6 pb^{-1} of integrated luminosity at 7 TeV center of mass energy. Since the following analysis requires more than 10 pb^{-1} to produce an interesting result, the QCD sample must be scaled up by large factors for many of the figures below. For this reason, as analysis cuts are applied, the few surviving QCD events have large statistical errors, so they are not included in many of the figures below. As more MC statistics are accumulated and QCD contributions are measured from data, it is probable that additional requirements on muon isolation will be needed to properly suppress multijet events. Such isolation requirements place restrictions on the maximum energy deposited in the calorimeter near the muon track and are very effective at rejecting QCD contributions. However, since muon isolation cuts do affect signal efficiency, and there are not sufficient MC statistics to properly determine how tight the cut needs to be, the use of muon isolation can not be justified in the following study. The details of the simulated backgrounds are listed below.

- The $t\bar{t}$ sample was generated using the LO POWHEG matrix element generator, which was input to Pythia for parton shower generation. The CTEQ6L1 LO parton distribution was used, and the resulting cross section was scaled by the appropriate k-factor. At the generator level, events were selected where the at least one W boson (from either t or

$\bar{t}$ decay) decayed leptonically, with an efficiency of approximately 54%, resulting in an overall effective NLO cross section of 87.03 pb.

- Single top samples were generated for s and t channels using the MC@NLO matrix element generator, which was input to HERWIG for parton shower generation. The NLO parton distribution function CTEQ6.6 was used, and only events where the W boson (from top quark decay) decays leptonically were selected, resulting in an effective cross section of 7.64 pb.
- Samples for W+jets were generated using the Alpgen matrix element generator and the HERWIG parton shower generator, where only events where the W decays leptonically are selected. The LO parton distribution function CTEQ6L1 was used. The total cross section for all W+jets samples is 10.65 fb.
- Samples for Z+jets were generated using the Alpgen matrix element generator and the HERWIG parton shower generator. The LO parton distribution function CTEQ6L1 was used. The total cross section for all Z+jets samples is 1.03 fb.
- Samples for W+jets, were the W decays to two b-jets, were generated using the Alpgen matrix element generator and the HERWIG parton shower generator. The LO parton distribution function CTEQ6L1 was used, and the total cross section is 9.52 pb.
- The diboson samples were generated using HERWIG. At the generator level, events with $Z/\gamma*$ masses greater than 20 GeV were selected. With this requirement, the partial cross-sections for WW, WZ, and ZZ boson pair production processes were 29.60 pb, 11.2 pb, and 4.59 respectively. The NLO MRST parton distribution functions [31] were used for event generation. A lepton filter was applied, with a transverse momentum threshold of $p_T > 10$ GeV and a maximum absolute pseudo-rapidity of $|\eta| < 2.8$, resulting in effective cross sections of 11.75 pb, 3.43 pb, and 0.977 pb for WW, WZ, and ZZ production processes, respectively.
- The QCD sample used was generated using HERWIG, using the NLO MRST parton distribution functions [31], and resulting in a cross section of 44 μb. A filter was applied at the generator level, requiring at least one jet with $p_T > 35$ GeV and $|\eta| < 2.7$, resulting in an effective cross section of 8.33 μb.

4.5 TRIGGER REQUIREMENTS

In order to ensure high trigger efficiencies in the dimuon signal, a single muon trigger with a p_T threshold of 10 GeV is employed. Due to the holes in the geometric acceptance of the LVL1 muon trigger system, which can be seen in Figure 2.14, LVL1 single muon trigger efficiency is only 87%. However, the LVL2 and EF trigger efficiencies with respect to LVL1 are high, and at least one muon generally has p_T much greater than 20 GeV, resulting in an overall EF trigger efficiency of greater than 98% for the dimuon leptoquark signal. A tag and probe method can be used to measure the offline trigger efficiency in events with 2 or more reconstructed muons. The two highest p_T muons in such an event are selected, where one muon is considered the "tag" and the other muon is the "probe". In events where the tag muon matches an ROI from the LVL1 muon trigger, the fraction of events where the probe also matches a LVL1 ROI gives the offline trigger efficiency, and is shown in Figures 4.2, 4.3, and 4.4 as a function of η, ϕ, and p_T , respectively.

This single muon offline trigger efficiency gives the event decision trigger efficiency for dimuon events (i.e. $\epsilon_{\text{Evt. Dec.}} = 1-(1-\epsilon_{\text{single}\mu})^2$). The inefficiencies due to holes in the muon LVL1 hardware coverage can be see in Figure 4.2, with drops in efficiency due to the service gap centered at $\eta = 0$, the support structures about $|\eta| = 0.4$ and $|\eta| = 1.0$, and the magnet legs about $|\eta| = 0.75$ (more apparent in the ϕ distribution). In the region $|\eta| > 2.4$, there are only two layers of TGCs, resulting in a lower efficiency between $2.4 < |\eta| < 2.5$. Low p_T thresholds in the LVL1 muon trigger only require information from two layers of LVL1 hardware, while high p_T triggers require information from three layers (see Figure 2.13). The 10 GeV trigger is the highest threshold that only requires information from two RPC/TGC layers. In Figure 4.3, the inefficiencies due to the structure of the toroid magnets can be seen with the positions of the eight toroid ribs. Even more pronounced is the drop in efficiency between $-2.0 < \phi < -1.2$, where the magnet support legs interfere with coverage, and the smallest efficiencies, centered at $\phi = -1.2$ and $\phi = -2.0$, are due to the added effect of the toroid ribs.

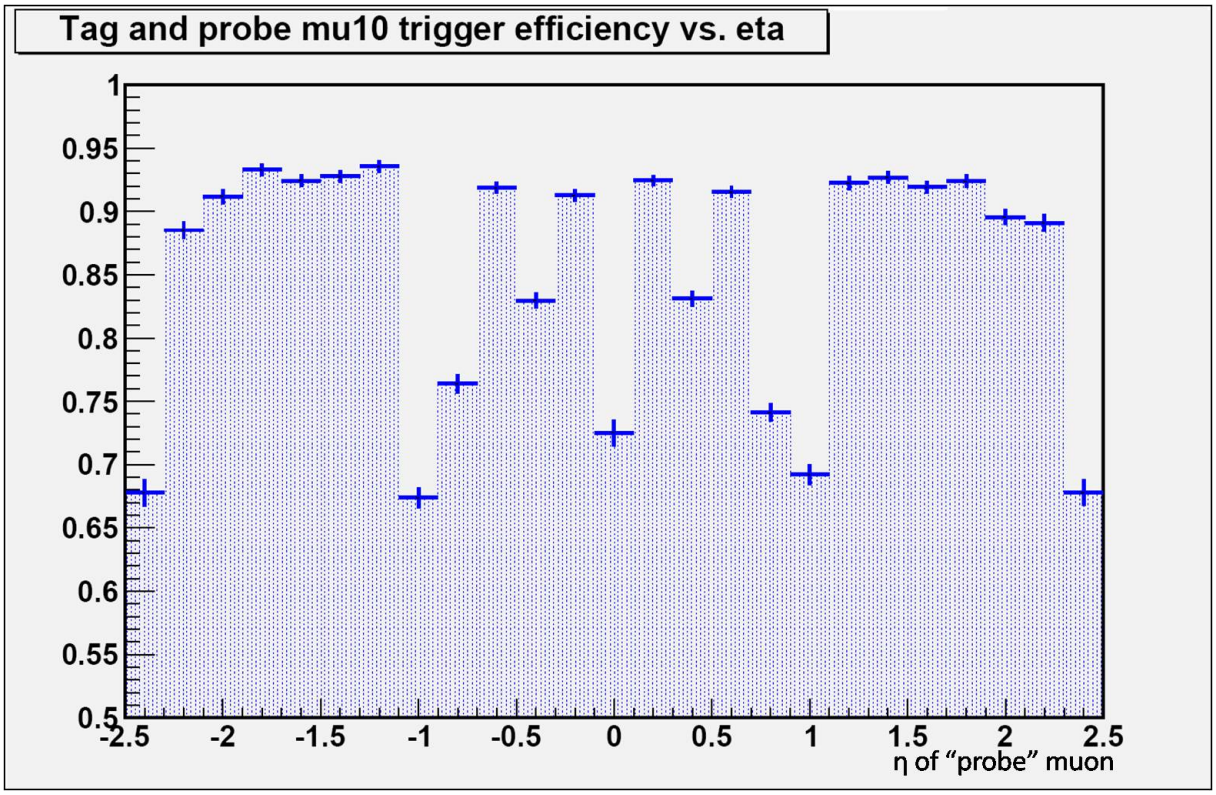

Figure 4.2: Tag and probe trigger efficiency as a function of the probe muon's η in SM background Monte Carlo events with 163.5 pb^{-1} of integrated luminosity.

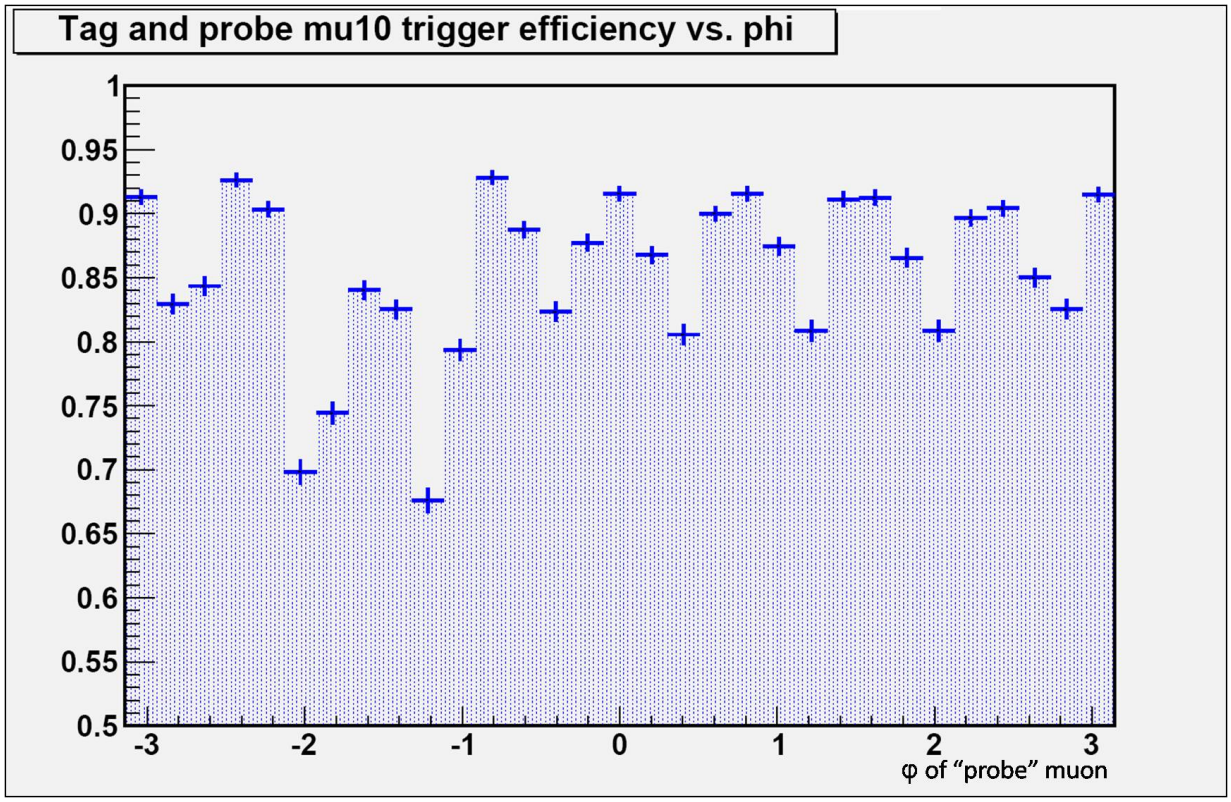

Figure 4.3: Tag and probe trigger efficiency as a function of the probe muon's ϕ in SM background Monte Carlo events with 163.5 pb^{-1} of integrated luminosity.

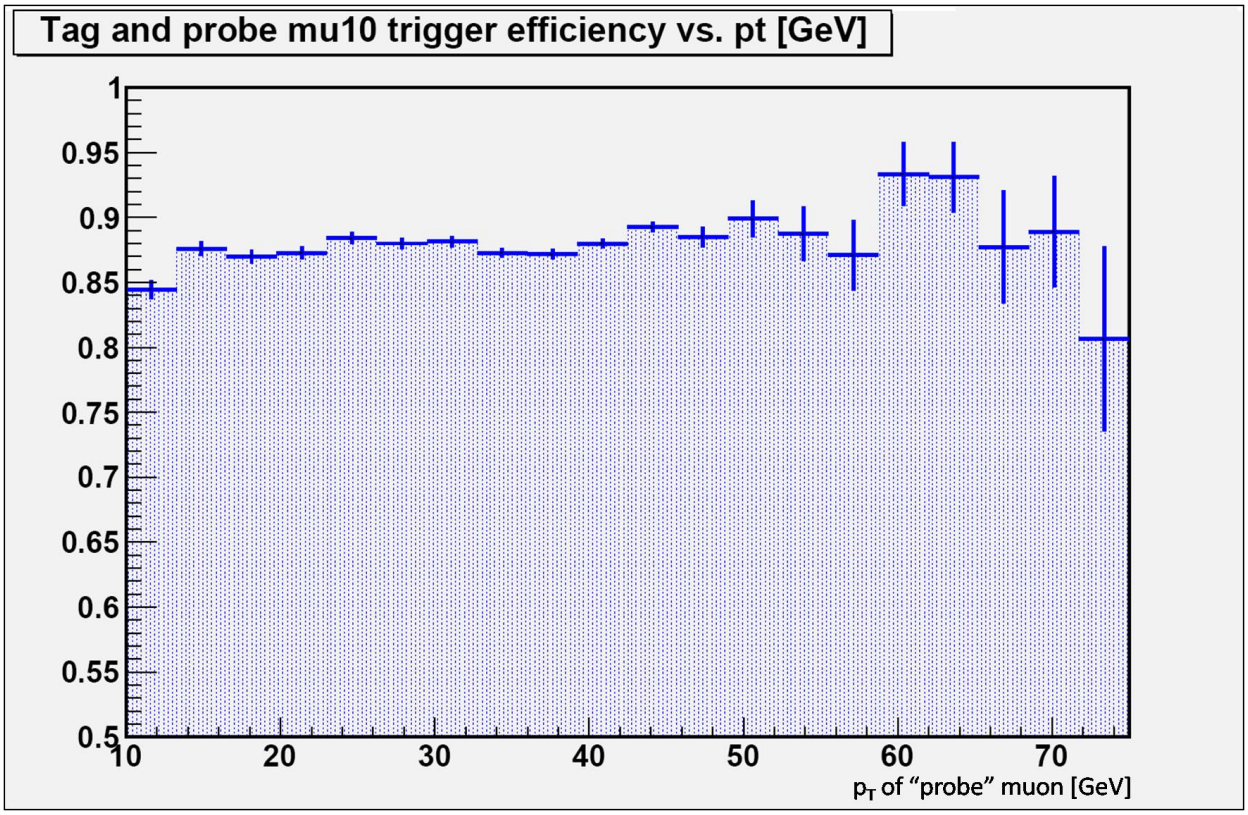

Figure 4.4: Tag and probe trigger efficiency as a function of the probe muon's p_T [GeV] in SM background Monte Carlo events with 163.5 pb^{-1} of integrated luminosity.

4.6 BASELINE EVENT SELECTION AND SIGNAL RECONSTRUCTION

In addition to the trigger requirements, candidate events must contain at least two reconstructed high p_T muons and two high p_T jets. Muons are required to have matching MS and ID tracks to eliminate muons that were not produced in the primary interaction. Particles as referred to in this analysis are defined as follows:

Muons:

- $p_T \geq 5$ GeV
- $|\eta| \leq 2.5$
- Combined muon (as defined in previous section) with $0 \leq \chi^2 \leq 100$ for both the combined track fit and match between MS and ID tracks

Jets:

- $p_T \geq 5$ GeV
- $|\eta| \leq 4.5$

Since event selection is based on the muon trigger, only events with two muons satisfying the above criteria are selected for analysis and recorded in DPDs, while jet requirements are imposed after the baseline selection. In addition to the criteria listed above, other quality cuts are placed on final state objects to insure only signal muons and jets, produced at the interaction point in high p_T events, are selected before background suppression is applied. These selections are summarized, along with signal and background efficiencies, in Tables 4.3-4.8.

First, only events with oppositely charged muons, as defined above, are accepted. The SM background of same-sign muons from the primary interaction is essentially zero, although events selected according to the above criteria can have same sign muons as a result of heavy flavor decays, pion decays, or muons produced as a result of interactions in the calorimeter and which happen to match a track from the inner detector. There is also a small contribution due to muon charge misidentification, although this effect is extremely small ($< 0.5\%$).

Next, selections are made based on the longitudinal and transverse impact parameters of the muon tracks with respect to the primary vertices with which they are associated. The

ratio of the impact parameter and its associated error is required to be less than 5. As shown in Figures 4.5 and 4.6, this helps to eliminate the QCD background, where high p_T muons can be produced in association with heavy flavor decays from displaced secondary vertices.

Finally, muons are required to have $p_T > 10$ GeV, which most signal events will pass and most QCD events will not. The dominant SM backgrounds mentioned above (Z/DY, WW, WZ, ZZ, $t\bar{t}$) that pass baseline selection will generally also survive these muon selections, as they *do* have two high-quality, high-p_T muons coming from the primary interaction. However, these backgrounds are more sensitive to jet selection, as many of the jets produced in these background interactions are of lower p_T and more of them are produced in the forward region of the detector than signal events, as seen in Table 4.7. Therefore, the two selected signal jets are required to have $p_T > 30$ GeV and $|\eta| < 2.5$. Muon and jet p_T distributions for signal and background can be seen in Figures 4.7 and 4.8.

At this point it is useful to examine the reconstructed leptoquark candidate mass distribution, which is shown in Figure 4.9 for signal events with a generated leptoquark mass of 300 GeV and background events, normalized to 25 pb^{-1} of integrated luminosity. In order to properly visualize the separation between signal and background, the two-dimensional leptoquark mass distribution is shown in Figure 4.10. Now selection criteria can be applied in order to suppress the dominant SM backgrounds, the most significant of which is the Z/DY contribution. Requiring $M_{\mu\mu} > 110$ GeV eliminates the majority of Z/DY events. This has a dramatic effect on the reconstructed leptoquark mass distribution in backgrounds, as seen in Figure 4.14.

In addition, the scalar sum of the final state particles' p_T ($S_T = p_{T\mu 1}+p_{T\mu 2}+p_{Tjet1}+p_{Tjet2}$) can be used to discriminate between signal and background. Since this analysis seeks to isolate a resonance of large mass, S_T is a useful variable to probe regions of larger reconstructed mass without selecting higher reconstructed $M_{\mu j}$ a priori. Values of S_T and $M_{\mu\mu}$ cuts were optimized after all final state particle cuts. Tevatron experiments have excluded leptoquark masses less than 150 GeV for all values of the branching fraction $\beta(LQ \to \mu q)$. Therefore, in order to maximize sensitivity in the signal region, only events with both reconstructed leptoquark candidate masses greater than 150 GeV were used for optimization. The distributions for S_T and $M_{\mu\mu}$ for signal and background events can be seen in Figures 4.11 and 4.12, where

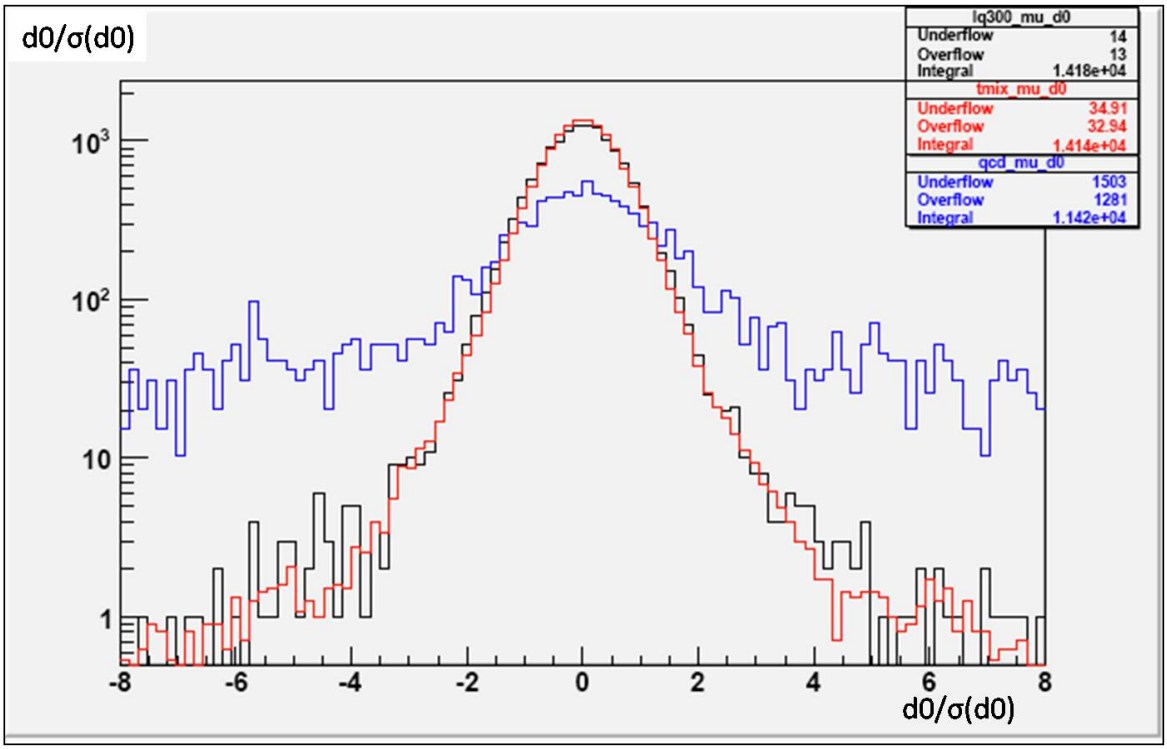

Figure 4.5: Muon transverse impact parameter (with respect to the primary vertex) divided by its error in signal and background events with two oppositely charged muons. All histograms are scaled to the same number of entries, dominant backgrounds - Z/DY, WW, WZ, ZZ, $t\bar{t}$ - (red), QCD (blue), and signal $M_{LQ} = 300$ (black).

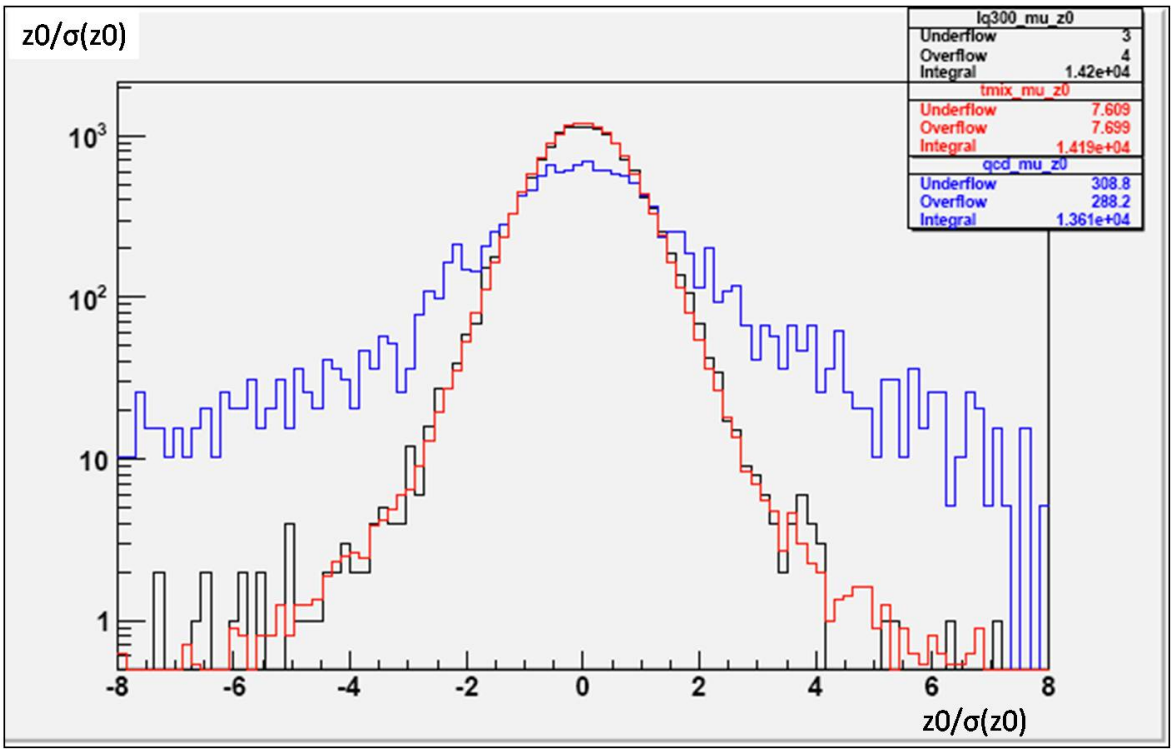

Figure 4.6: Muon longitudinal impact parameter (with respect to the primary vertex) divided by its error in signal and background events with two oppositely charged muons. All histograms are scaled to the same number of entries, dominant backgrounds - Z/DY, WW, WZ, ZZ, $t\bar{t}$ - (red), QCD (blue), and signal $M_{LQ} = 300$ (black).

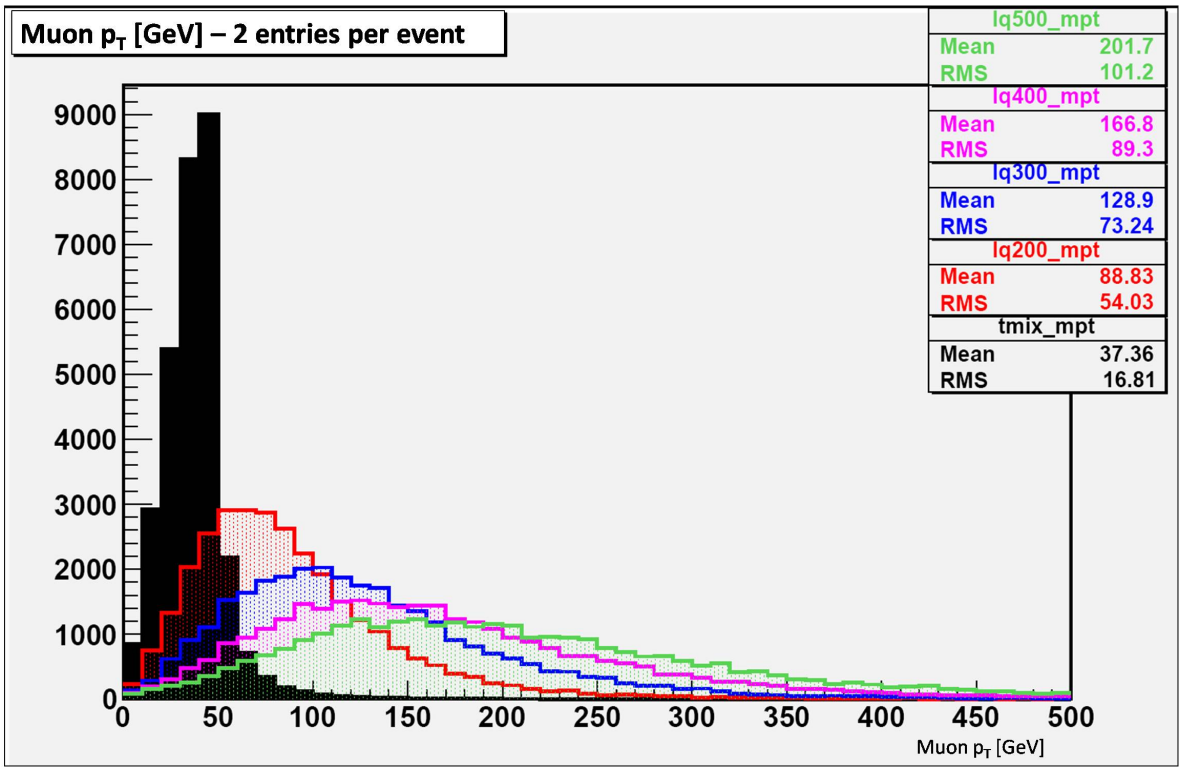

Figure 4.7: Muon p_T [GeV] in signal and background events after all final state particle cuts. All histograms are scaled to the same number of entries, SM backgrounds (black), signal $M_{LQ} = 200$ (red), signal $M_{LQ} = 300$ (blue), signal $M_{LQ} = 400$ (magenta), signal $M_{LQ} = 500$ (green).

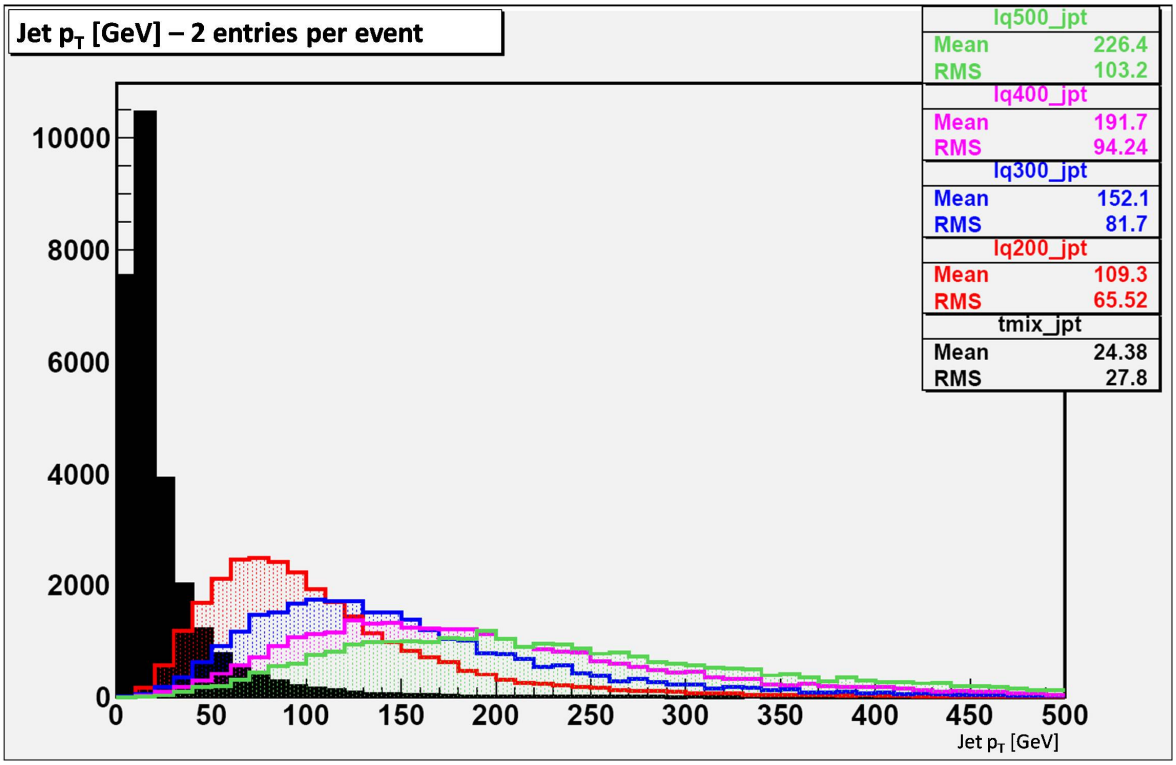

Figure 4.8: Jet p_T [GeV] in signal and background events after all final state particle cuts. All histograms are scaled to the same number of entries, SM backgrounds (black), signal $M_{LQ} = 200$ (red), signal $M_{LQ} = 300$ (blue), signal $M_{LQ} = 400$ (magenta), signal $M_{LQ} = 500$ (green).

only events passing all final state particle cuts are shown. While one dimuon mass cut effectively suppresses Z/DY contributions for searches of all leptoquark masses, increasing cuts on S_T are used to probe higher mass ranges for the leptoquark signal. At this point, almost no backgrounds to the signal remain in Monte Carlo events, as seen in Figure 4.15. However, Figure 4.15 is a one-dimensional projection of a two-dimensional distribution (shown in Figure 4.16), which more clearly shows the separation between signal and background events at this point in the analysis. Figure 4.17 shows the one dimensional projection when events where both leptoquark candidates are not greater than 150 GeV are eliminated.

4.7 DISTORTIONS IN SIGNAL SHAPE

When reconstructing the leptoquark pair from two muons and two jets, there are several effects that distort the Gaussian shape of the reconstructed leptoquark mass. In some cases, poor reconstruction of the jet energy smears the distribution. However, combinatorial effects dominate the distortion in the low mass shoulder and high mass tail of the distribution. In some events, the wrong mu-jet pairing is chosen by the analysis algorithm. Alternatively, sometimes one or both of the two highest p_T jets in the event are not products of leptoquark decay. Both of the combinatorial contributions have a similar effect on the shape of the reconstructed leptoquark mass, and this effect is more frequent as jet multiplicity increases.

This combinatorial effect can be seen in Figure 4.18. The black distribution shows all reconstructed leptoquark events where both muons match truth muons from leptoquark decay, and both jets match truth particle jets, with red + blue = black. The red distribution includes events where the analysis algorithm for reconstructing the leptoquark pair chooses a jet for one leptoquark but the jet is actually closer to the quark from the other leptoquark decay, and the jet assignment is labeled as 'mismatched'. The blue distribution shows events where the jet assignment appears to be correct for both leptoquark candidates, i.e. the truth quark from a leptoquark decay is closest to the jets that was assigned to reconstruct it. The apparent bump in the signal region in the 'mismatched' distribution comes from events where only one jet appears to be 'mismatched' - where one jet is chosen to be reconstructed with

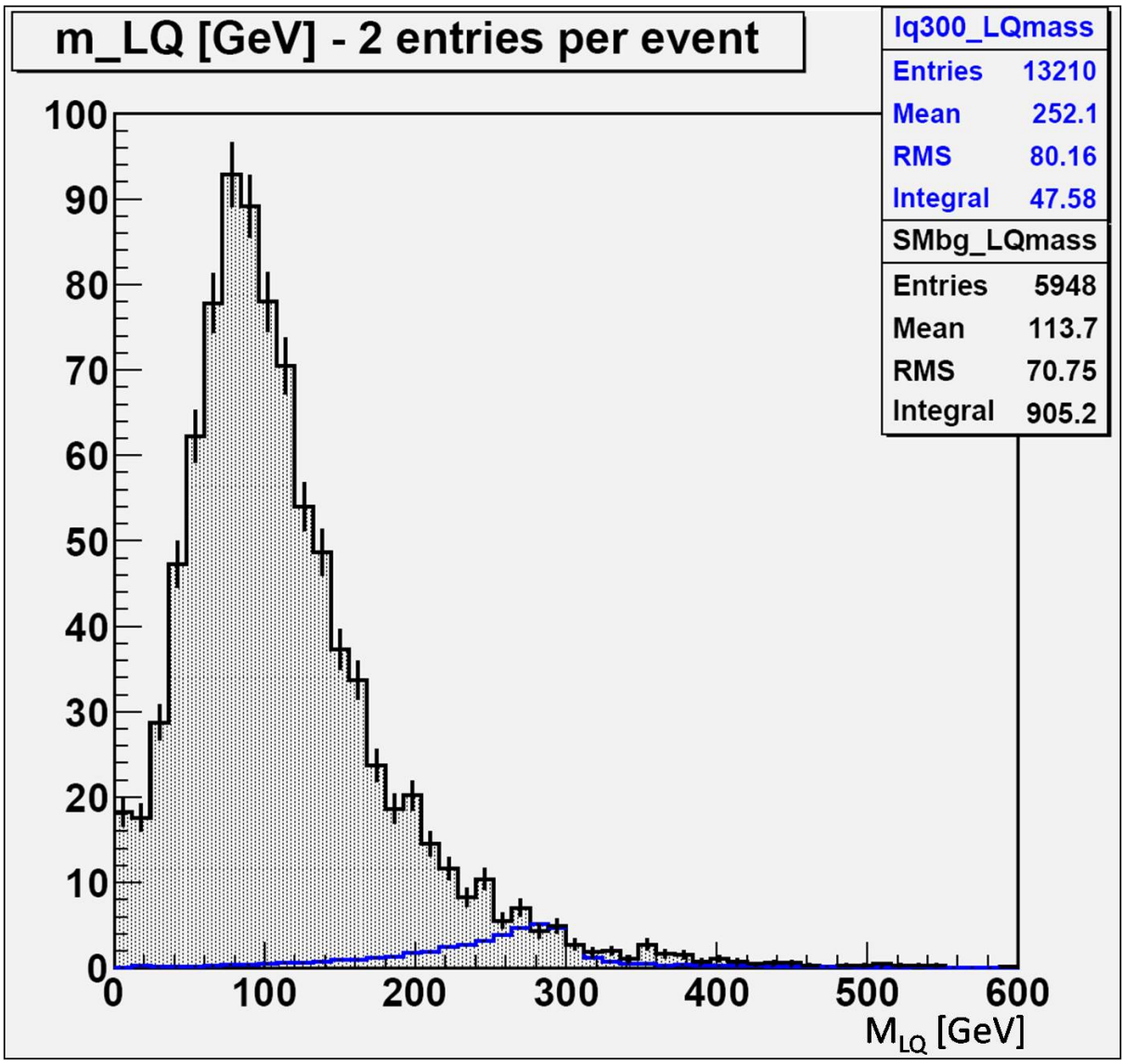

Figure 4.9: Reconstructed leptoquark mass [GeV] in events that pass all final state particle cuts in signal (blue) and background (black) for 25 pb^{-1}. Note: two entries per event, one for each leptoquark candidate.

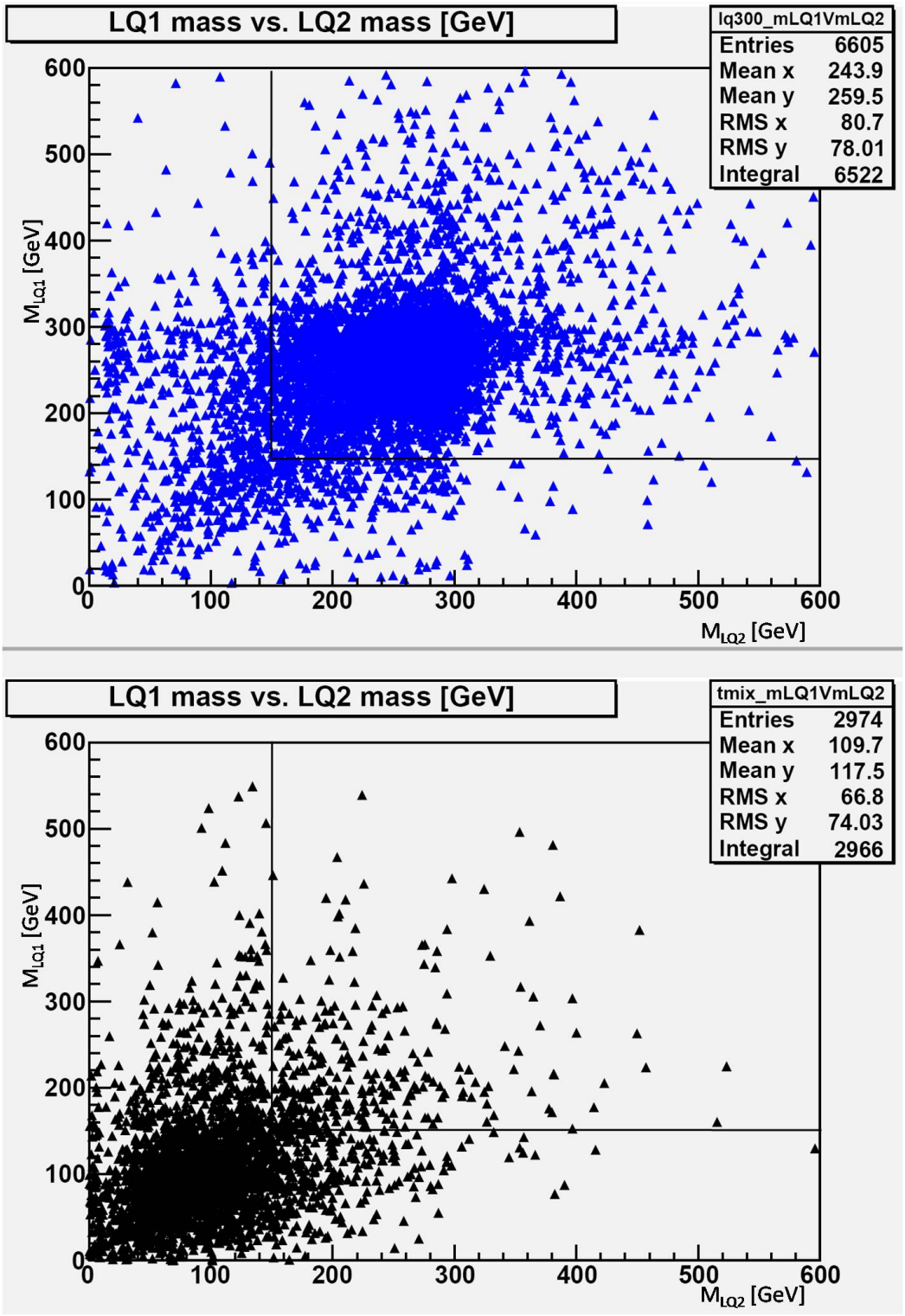

Figure 4.10: Two dimensional reconstructed leptoquark mass [GeV] distribution in events that pass all final state particle cuts in signal events with $M_{LQ} = 300$ GeV (blue) and background events (black). Red line indicates region where S_T and $M_{\mu\mu}$ selection was optimized.

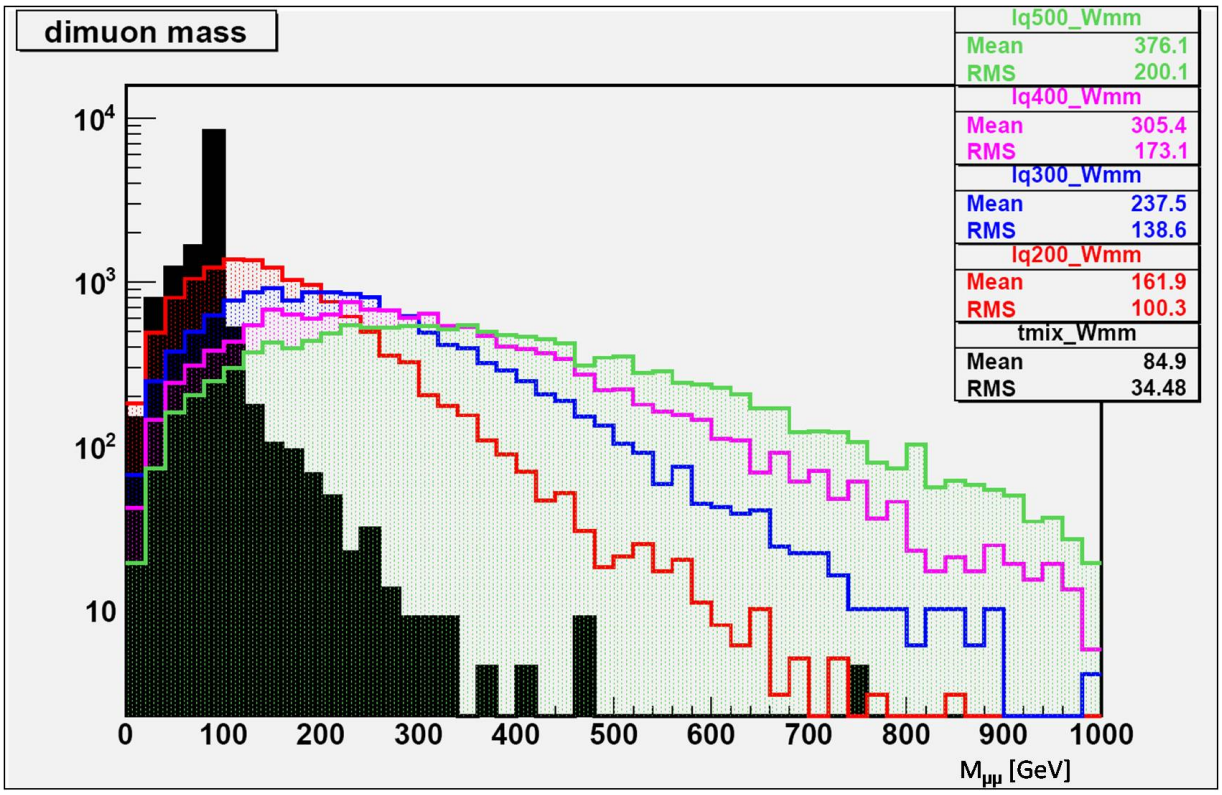

Figure 4.11: Dimuon mass [GeV] in signal and background events after all final state particle cuts. All histograms are scaled to the same number of entries, SM backgrounds (black), signal $M_{LQ} = 200$ (red), signal $M_{LQ} = 300$ (blue), signal $M_{LQ} = 400$ (magenta), signal $M_{LQ} = 500$ (green).

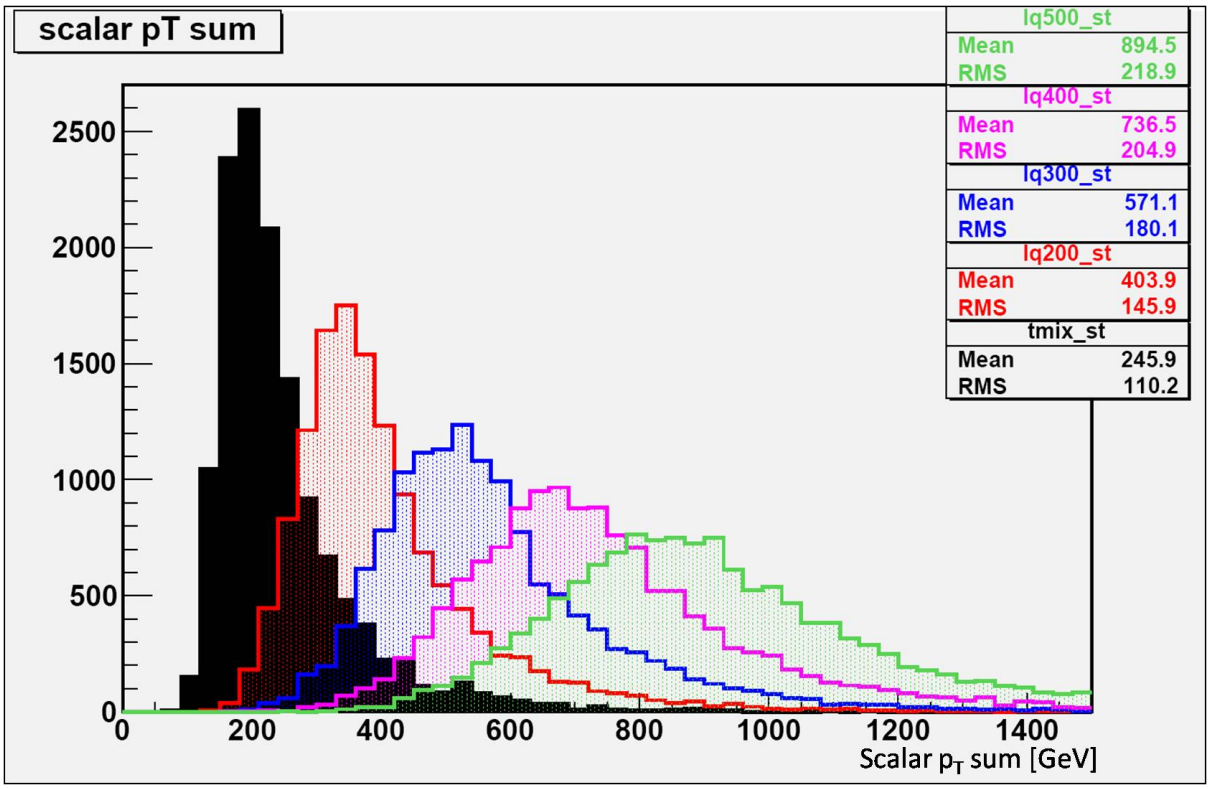

Figure 4.12: S_T [GeV] (scalar p_T sum of all final state particles) in signal and background events after all final state particle cuts. All histograms are scaled to the same number of entries, SM backgrounds (black), signal $M_{LQ} = 200$ (red), signal $M_{LQ} = 300$ (blue), signal $M_{LQ} = 400$ (magenta), signal $M_{LQ} = 500$ (green).

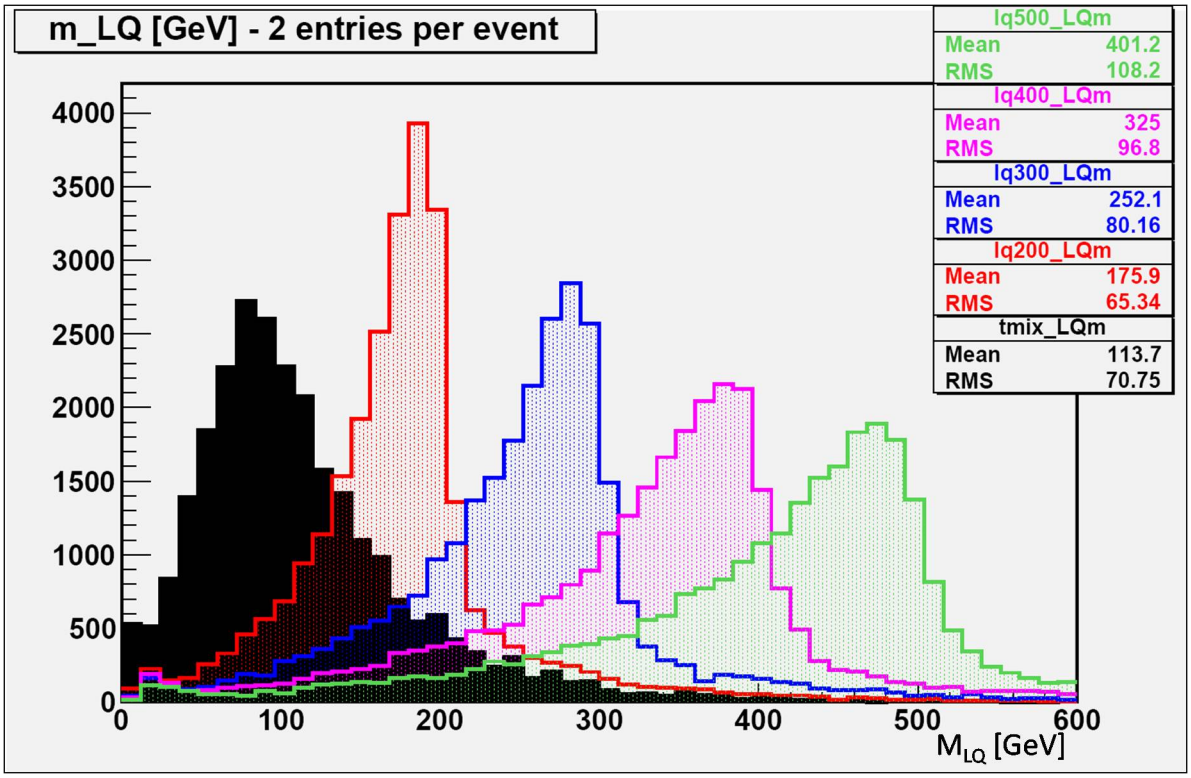

Figure 4.13: Reconstructed leptoquark candidate masses [GeV] in signals and SM background after all final state particle cuts. Note: 2 entries per event, one for each leptoquark candidate. All histograms are scaled to the same number of entries, SM backgrounds (black), signal $M_{LQ} = 200$ (red), signal $M_{LQ} = 300$ (blue), signal $M_{LQ} = 400$ (magenta), signal $M_{LQ} = 500$ (green).

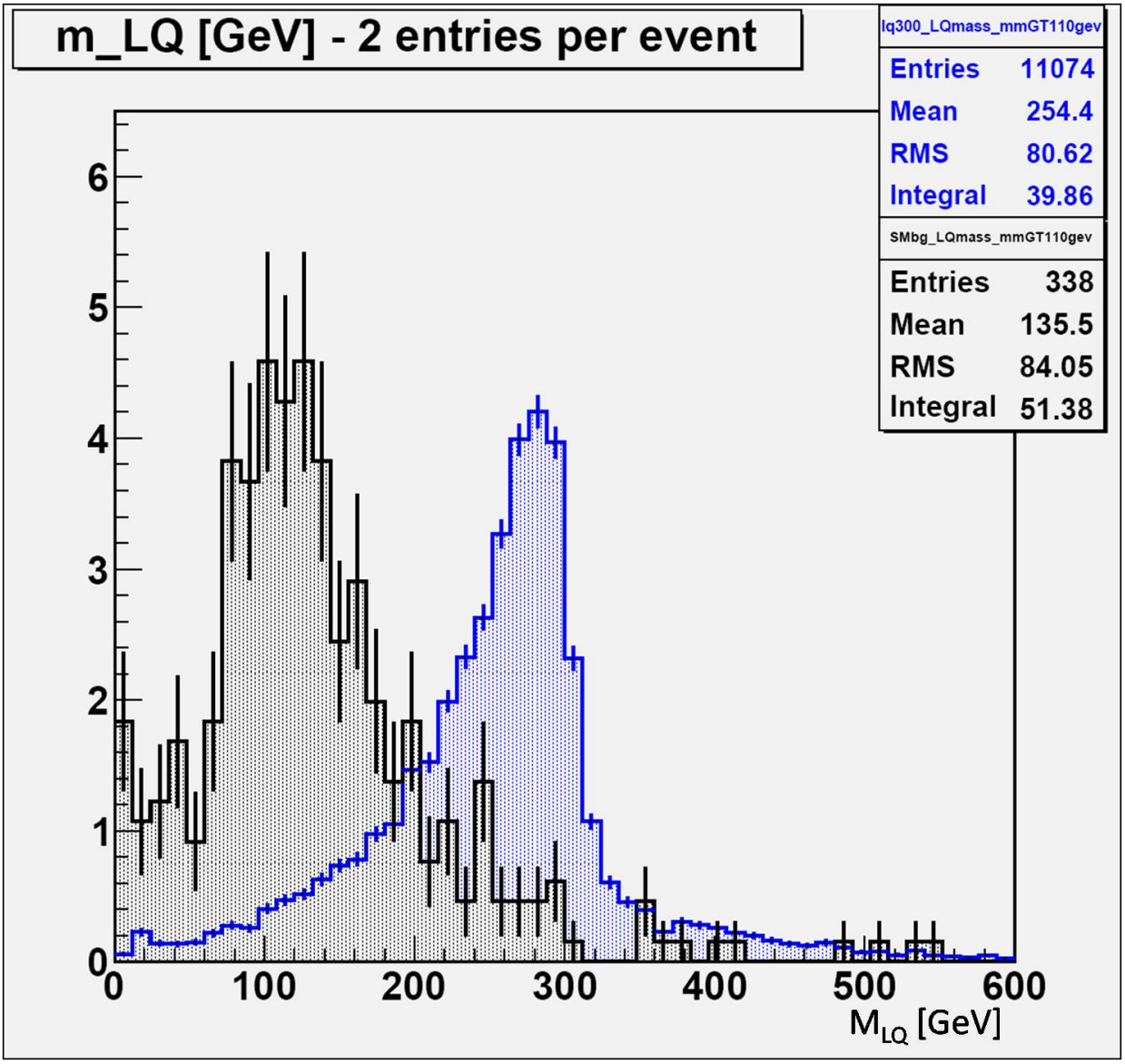

Figure 4.14: Reconstructed leptoquark mass [GeV] in events that pass all final state particle cuts and $M_{\mu\mu} > 110$ GeV in signal (blue) and background (black) for 25 pb^{-1}. Note: two entries per event, one for each leptoquark candidate.

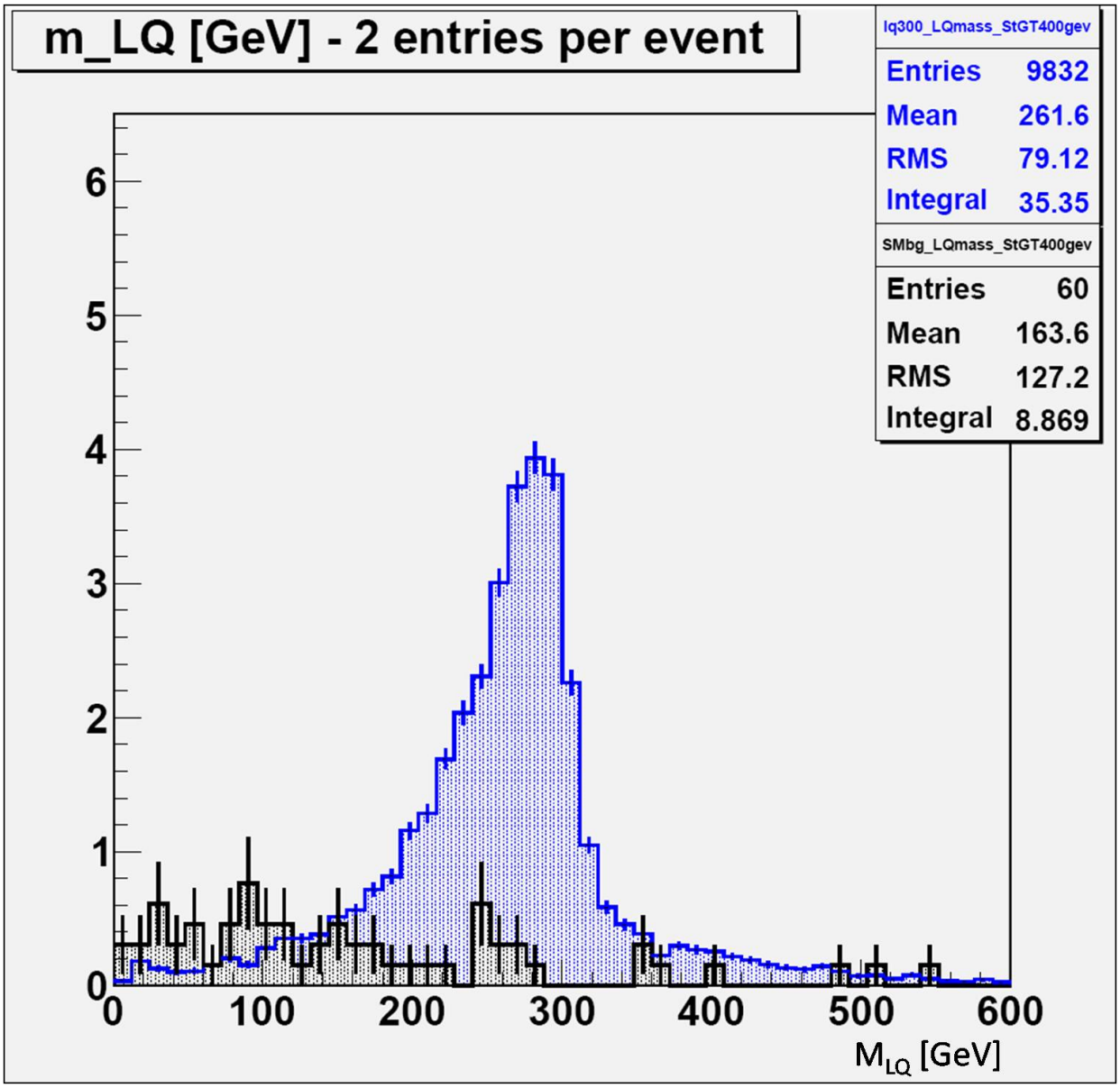

Figure 4.15: Reconstructed leptoquark mass [GeV] in events that pass all final state particle cuts, $M_{\mu\mu} > 110$ GeV, and $S_T > 400$ GeV in signal (blue) and background (black) for 25 pb^{-1}. Note: two entries per event, one for each leptoquark candidate.

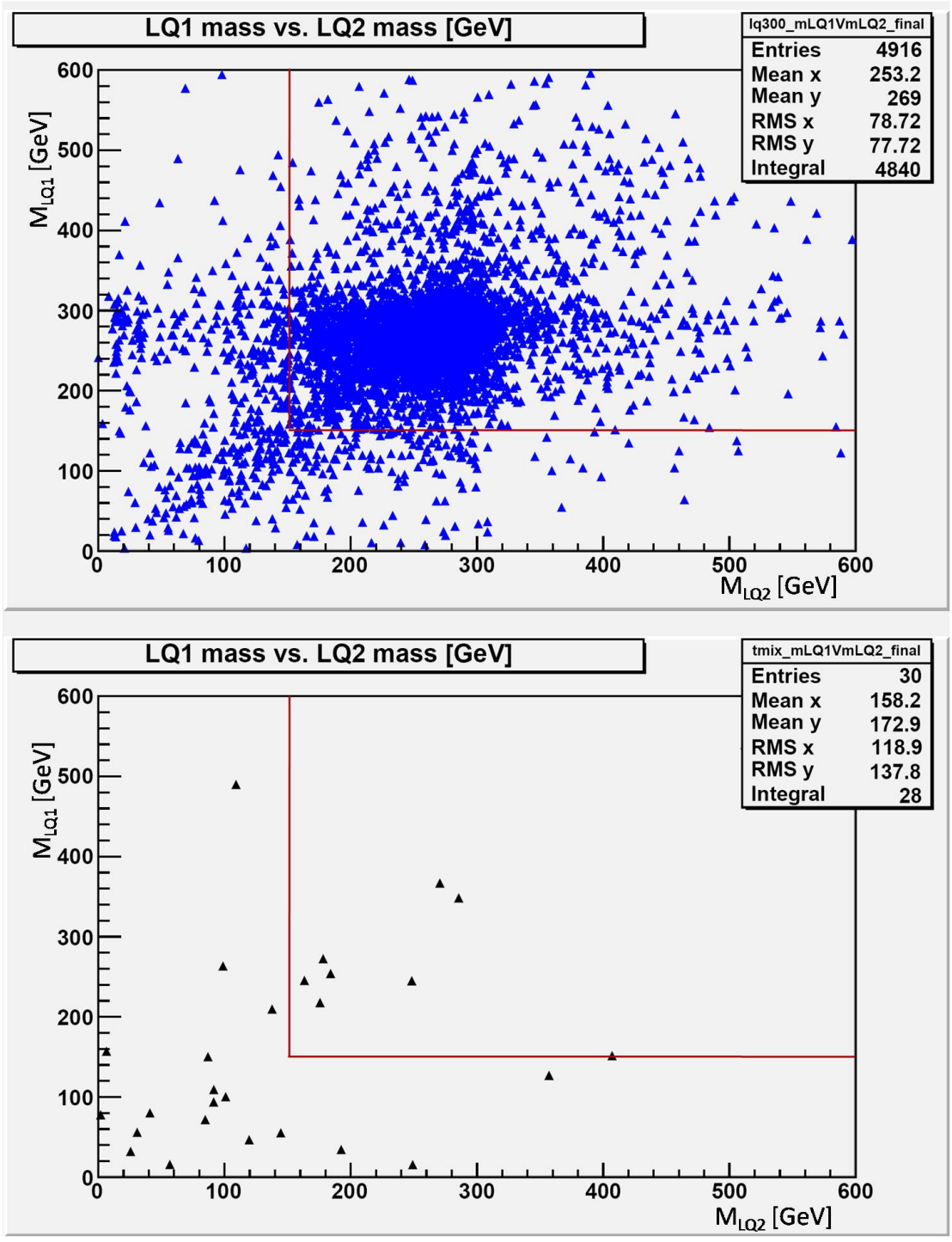

Figure 4.16: Two dimensional reconstructed leptoquark mass [GeV] distribution in events that pass all final state particle cuts, $M_{\mu\mu} > 110$ GeV, and $S_T > 400$ GeV in signal events, with $M_{LQ} = 300$ GeV (blue), and background events (black). Red line indicates region where both leptoquark candidate masses are greater than 150 GeV.

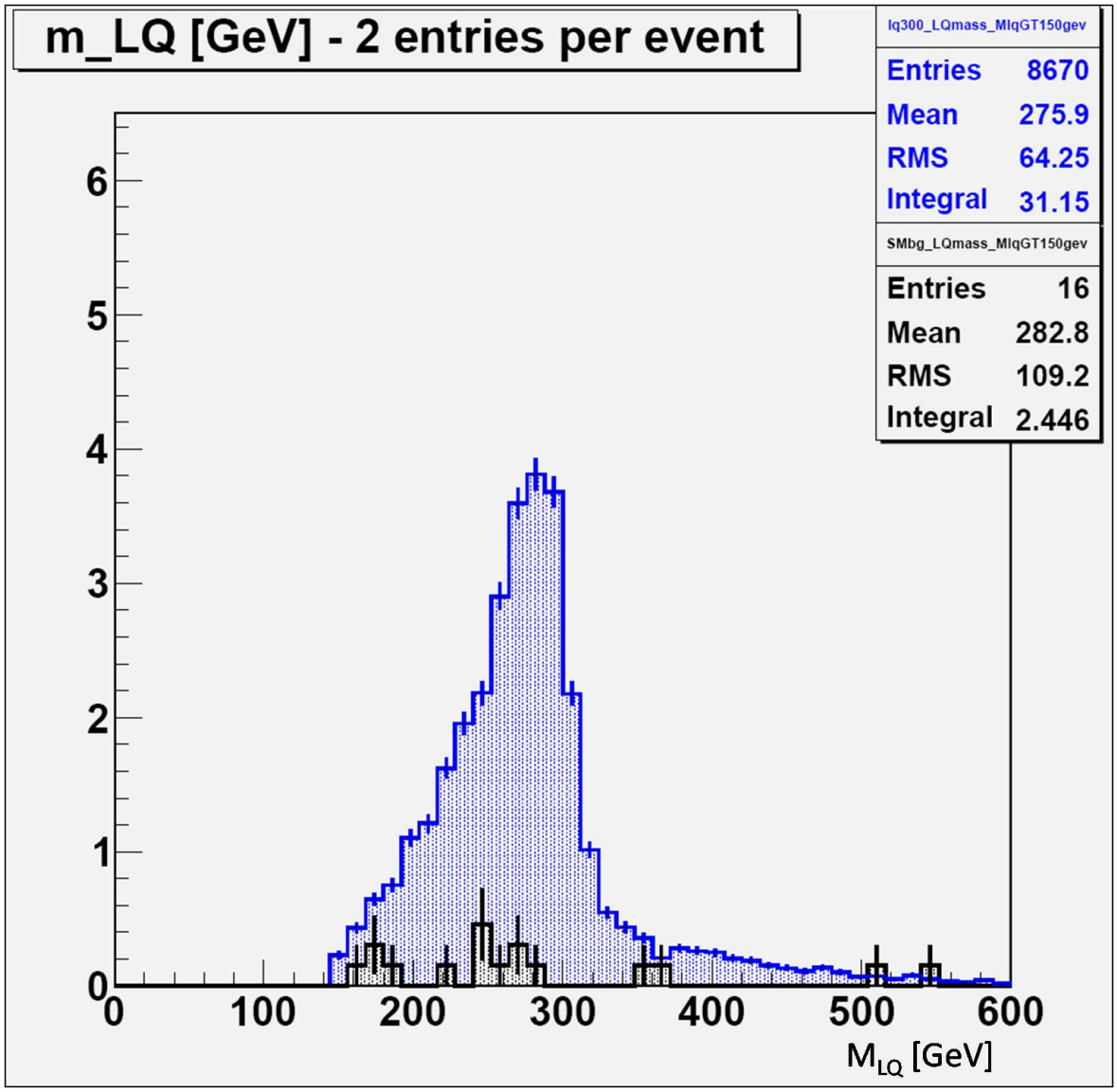

Figure 4.17: Reconstructed leptoquark mass [GeV] in events that pass all final state particle cuts, $M_{\mu\mu} > 110$ GeV, $S_T > 400$ GeV, and have two leptoquark candidates with $M_{LQ} > 150$ GeV in signal (blue) and background (black) for 25 pb^{-1}. Note: two entries per event, one for each leptoquark candidate.

Selection criteria	# events passed	Cum eff	Eff wrt last
N sample	18744	1.0	
2 or more muons	15589	0.83	0.83
Muons oppositely charged	15270	0.81	0.98
$\|z0\|/\sigma_{z0} < 5.0$	15230	0.81	1.00
$\|d0\|/\sigma_{d0} < 5.0$	15125	0.81	0.99
Muon $p_T > 10$ GeV	14900	0.79	0.99
2 or more jets	14900	0.79	1.00
2 highest p_T jets' $\|\eta\| < 2.5$	14015	0.75	0.94
Jet $p_T > 30$ GeV	13290	0.71	0.95
$M_{\mu\mu} > 110$ GeV	8912	0.48	0.67
Scalar p_T sum > 200 GeV	8865	0.47	0.99
Both $M_{LQ} > 150$ GeV	5502	0.29	0.62

Table 4.3: Efficiency of signal selection and background suppression criteria for signal MC sample ($M_{LQ} = 200$ GeV). Column 1: selection, Column 2: number of events in the Monte Carlo sample passing the selection (cumulative down the table), Column 3: fraction of events in the sample passing the cumulative cuts, Column 4: fraction of events passing the previous selection that pass the current one

Selection criteria	# events passed	Cum eff	Eff wrt last
N sample	8615	1.0	
2 or more muons	7280	0.85	0.85
Muons oppositely charged	7102	0.82	0.98
$\|z0\|/\sigma_{z0} < 5.0$	7079	0.82	1.00
$\|d0\|/\sigma_{d0} < 5.0$	7025	0.82	0.99
Muon $p_T > 10$ GeV	6962	0.81	0.99
2 or more jets	6962	0.81	1.00
2 highest p_T jets' $\|\eta\| < 2.5$	6716	0.78	0.96
Jet $p_T > 30$ GeV	6605	0.77	0.98
$M_{\mu\mu} > 110$ GeV	5537	0.64	0.84
Scalar p_T sum > 400 GeV	4916	0.57	0.89
Both $M_{LQ} > 150$ GeV	4335	0.50	0.88

Table 4.4: Efficiency of signal selection and background suppression criteria for signal MC sample ($M_{LQ} = 300$ GeV). Column 1: selection, Column 2: number of events in the Monte Carlo sample passing the selection (cumulative down the table), Column 3: fraction of events in the sample passing the cumulative cuts, Column 4: fraction of events passing the previous selection that pass the current one

Selection criteria	# events passed	Cum eff	Eff wrt last
N sample	8952	1.0	
2 or more muons	7605	0.85	0.85
Muons oppositely charged	7422	0.83	0.98
$\|z0\|/\sigma_{z0} < 5.0$	7386	0.83	1.00
$\|d0\|/\sigma_{d0} < 5.0$	7303	0.82	0.99
Muon $p_T > 10$ GeV	7257	0.81	0.99
2 or more jets	7257	0.81	1.00
2 highest p_T jets' $\|\eta\| < 2.5$	7091	0.79	0.98
Jet $p_T > 30$ GeV	7027	0.78	0.99
$M_{\mu\mu} > 110$ GeV	6336	0.71	0.90
Scalar p_T sum > 500 GeV	5814	0.65	0.92
Both $M_{LQ} > 150$ GeV	5353	0.60	0.92

Table 4.5: Efficiency of signal selection and background suppression criteria for signal MC sample ($M_{LQ} = 400$ GeV). Column 1: selection, Column 2: number of events in the Monte Carlo sample passing the selection (cumulative down the table), Column 3: fraction of events in the sample passing the cumulative cuts, Column 4: fraction of events passing the previous selection that pass the current one

Selection criteria	# events passed	Cum eff	Eff wrt last
N sample	8733	1.0	
2 or more muons	7451	0.85	0.85
Muons oppositely charged	7244	0.83	0.97
$\|z0\|/\sigma_{z0} < 5.0$	7209	0.83	1.00
$\|d0\|/\sigma_{d0} < 5.0$	7144	0.82	0.99
Muon $p_T > 10$ GeV	7106	0.81	0.99
2 or more jets	7106	0.81	1.00
2 highest p_T jets' $\|\eta\| < 2.5$	6978	0.80	0.98
Jet $p_T > 30$ GeV	6956	0.80	1.00
$M_{\mu\mu} > 110$ GeV	6508	0.75	0.94
Scalar p_T sum > 650 GeV	5787	0.66	0.89
Both $M_{LQ} > 150$ GeV	5485	0.63	0.95

Table 4.6: Efficiency of signal selection and background suppression criteria for signal MC sample ($M_{LQ} = 500$ GeV). Column 1: selection, Column 2: number of events in the Monte Carlo sample passing the selection (cumulative down the table), Column 3: fraction of events in the sample passing the cumulative cuts, Column 4: fraction of events passing the previous selection that pass the current one

Selection criteria	# events passed	Cum eff	Eff wrt last
N sample	1498783	1.0	
2 or more muons	87288	5.8E−02	0.06
Muons oppositely charged	85245	5.7E−02	0.98
$\|z0\|/\sigma_{z0} < 5.0$	84893	5.7E−02	1.00
$\|d0\|/\sigma_{d0} < 5.0$	83832	5.6E−02	0.99
Muon $p_T > 10$ GeV	79451	5.3E−02	0.95
2 or more jets	42466	2.8E−02	0.53
2 highest p_T jets' $\|\eta\| < 2.5$	28096	1.9E−02	0.66
Jet $p_T > 30$ GeV	2964	2.0E−03	0.11
$M_{\mu\mu} > 110$ GeV	169	1.1E−04	0.06
Scalar p_T sum > 200 GeV	152	1.0E−04	0.90
Both $M_{LQ} > 150$ GeV	28	1.9E−05	0.18
Scalar p_T sum > 400 GeV	30	2.0E−05	0.18
Both $M_{LQ} > 150$ GeV	8	5.3E−06	0.27
Scalar p_T sum > 500 GeV	14	9.3E−06	0.08
Both $M_{LQ} > 150$ GeV	3	2.0E−06	0.21
Scalar p_T sum > 650 GeV	4	2.7E−06	0.02
Both $M_{LQ} > 150$ GeV	0	0.0E+00	0.00

Table 4.7: Efficiency of signal selection and background suppression criteria for dominant SM backgrounds (Z/DY, WW, WZ, ZZ, $t\bar{t}$) MC sample. Column 1: selection, Column 2: number of events in the Monte Carlo sample passing the selection (cumulative down the table), Column 3: fraction of events in the sample passing the cumulative cuts, Column 4: fraction of events passing the previous selection that pass the current one

Selection criteria	# events passed	Cum eff	Eff wrt last
N sample	4971564	1.0	
2 or more muons	2209	4.4E−04	0.00
Muons oppositely charged	1380	2.8E−04	0.62
$\|z0\|/\sigma_{z0} < 5.0$	1171	2.4E−04	0.85
$\|d0\|/\sigma_{d0} < 5.0$	738	1.5E−04	0.63
Muon $p_T > 10$ GeV	123	2.5E−05	0.17
2 or more jets	123	2.5E−05	1.00
2 highest p_T jets' $\|\eta\| < 2.5$	111	2.2E−05	0.90
Jet $p_T > 30$ GeV	89	1.8E−05	0.80
$M_{\mu\mu} > 110$ GeV	1	2.0E−07	0.01
Scalar p_T sum > 200 GeV	1	2.0E−07	1.00
Both $M_{LQ} > 150$ GeV	0	0.0E+00	0.00
Scalar p_T sum > 400 GeV	0	0.0E+00	–
Both $M_{LQ} > 150$ GeV	0	0.0E+00	–
Scalar p_T sum > 500 GeV	0	0.0E+00	–
Both $M_{LQ} > 150$ GeV	0	0.0E+00	–
Scalar p_T sum > 650 GeV	0	0.0E+00	–
Both $M_{LQ} > 150$ GeV	0	0.0E+00	–

Table 4.8: Efficiency of signal selection and background suppression criteria for QCD MC sample. Column 1: selection, Column 2: number of events in the Monte Carlo sample passing the selection (cumulative down the table), Column 3: fraction of events in the sample passing the cumulative cuts, Column 4: fraction of events passing the previous selection that pass the current one

M_{LQ} GeV	Total SM background	Z/DY	$t\bar{t}$	single top
200	28	17	10	1
300	8	7	1	0
400	3	3	0	0
500	0	0	0	0

Table 4.9: Number of SM background events surviving final signal selection and background suppression criteria for various leptoquark mass hypotheses and the sources for those events.

the muon from the same leptoquark decay, and the other jet comes from the underlying event, resulting in one good leptoquark candidate and one bad. This effect can be seen when the blue distribution is broken down into components as in Figure 4.19, where both jets appear to be mismatched (in magenta) and where only one is mismatched (green).

While other kinematic variables, such as mu-jet angular separation, can be used to select such 'mismatched' events, they can not be recovered by switching jet assignment without also moving background events into the signal region. It is important to understand the source of these shapes, but combinatorial effects at this level should not significantly affect the discovery potential for leptoquarks in a counting analysis.

4.8 BACKGROUND SUPPRESSION EFFECTS ON $t\bar{t}$ SHAPES

As background suppression is applied, an irregular shape begins to appear in the reconstructed leptoquark candidate mass distribution for $t\bar{t}$ events, specifically when selecting events with higher S_T , as can be seen in the 1-D projections in Figures 4.20-4.23. This is due to the reconstruction algorithm, which chooses mu-jet combinations according to the mass difference between the reconstructed leptoquark pair. This leads to a few possible scenarios when reconstructing $M_{\mu j}$. The two most common possibilities are that a muon

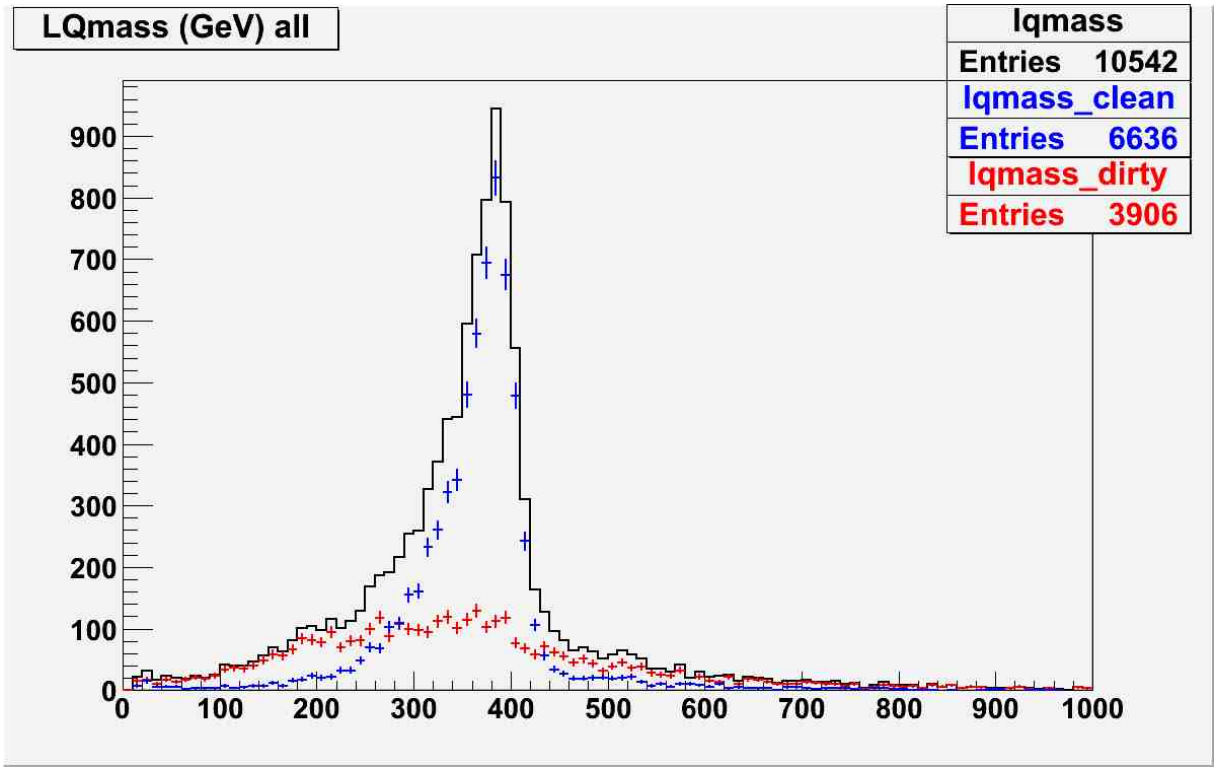

Figure 4.18: Reconstructed leptoquark pair masses in signal events ($M_{LQ} = 400$ GeV) where both jets and both muons match truth particles from leptoquark decay: all such events (black), where jet assignment is 'mismatched' (red), where jet assignment is 'correct' (blue). MC events were generated at 10 TeV center of mass energy. Note: 2 entries per event

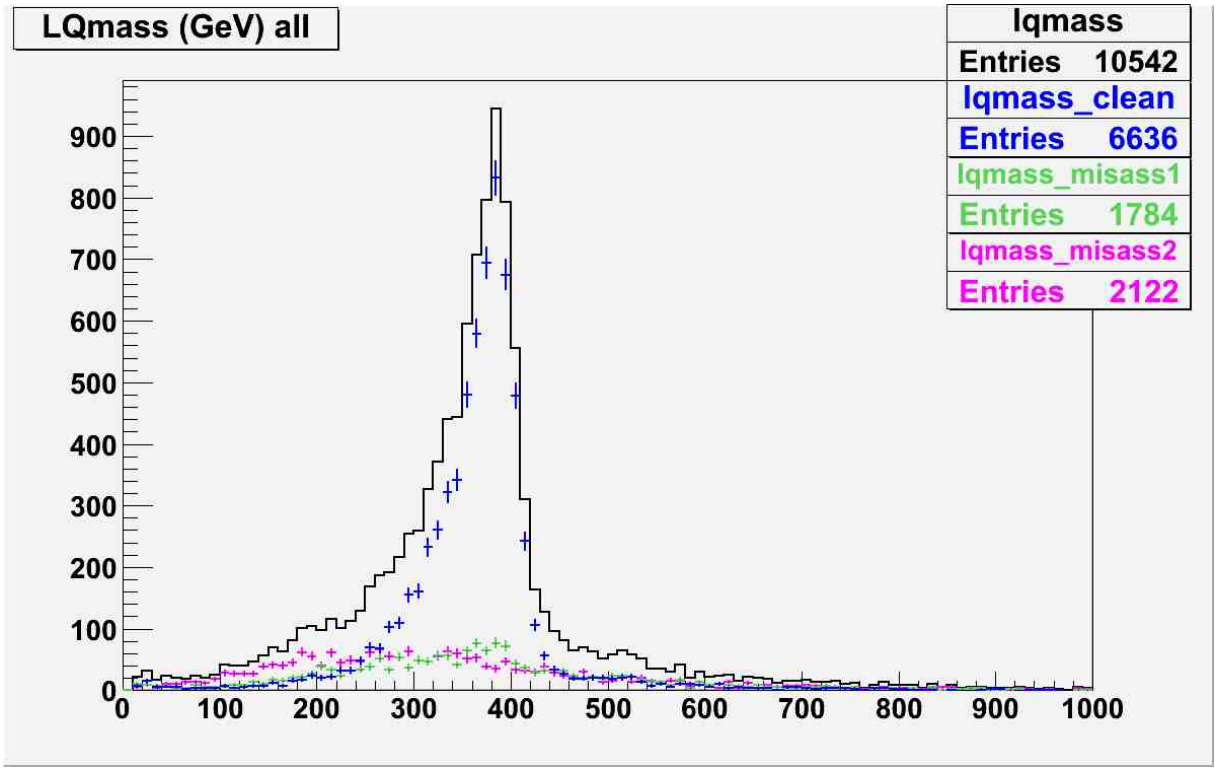

Figure 4.19: Reconstructed leptoquark pair masses in signal events ($M_{LQ} = 400$ GeV) where both jets and both muons match truth particles from leptoquark decay: all such events (black), where both jet assignments are 'mismatched' (magenta), where one jet assignment is 'mismatched' and one jet assignment is 'correct' (green), where both jet assignments are 'correct' (blue). MC events were generated at 10 TeV center of mass energy. Note: 2 entries per event

and a jet from top quark decay are reconstructed together, resulting in a bump below the top quark mass (due to the missing neutrino), and that a muon from one top quark and the jet from the other top quark are reconstructed together, resulting in a higher mass. As higher S_T events are selected, meaning more back-to-back decays, this effect becomes more distinct as the high-mass scenario is shifted further from the top quark peak. This effect becomes much less apparent as more cuts are imposed to suppress background. In addition to those two scenarios, there are many $t\bar{t}$ events passing baseline selection where one muon is produced inside a b-jet. The effect of this can be seen in the bump near zero in $t\bar{t}$ events in Figure 4.21, when the muon is produced inside the jet with which it is paired to reconstruct the leptoquark candidate, but there is also a high-mass scenario associated with this effect. However, such events are more sensitive to the impact parameter cuts imposed on muons in the above analysis. Signal selection and background suppression criteria reduce all of these effects, such that they may only be apparent if selections are made in a particular order. However, it is important to keep such features of the reconstructed mass distribution in mind when selecting events based on a variable like S_T .

4.9 SYSTEMATIC ERRORS

Systematic uncertainties in this physics channel have been studied in detail with Monte Carlo data simulated at 14 TeV center of mass energy [32]. Current estimates for the values of dominant systematic errors at 7 TeV center of mass energy are equivalent or very similar to estimates for first data in 14 TeV collisions. Although the effect of systematic errors on signal and background selection efficiencies are also dependent on the pp center of mass energy, selection criteria have been adjusted to give similar selection efficiencies as the analysis developed for 14 TeV. In addition, the systematic error estimates listed below are extremely conservative, as they are meant to be considered for early data-taking only. As a result, some errors have not been propagated to uncertainties on selection efficiency in 7 TeV Monte Carlo, but rather the effect has been assumed to be the same as in [32]. The dominant errors are assumed to be:

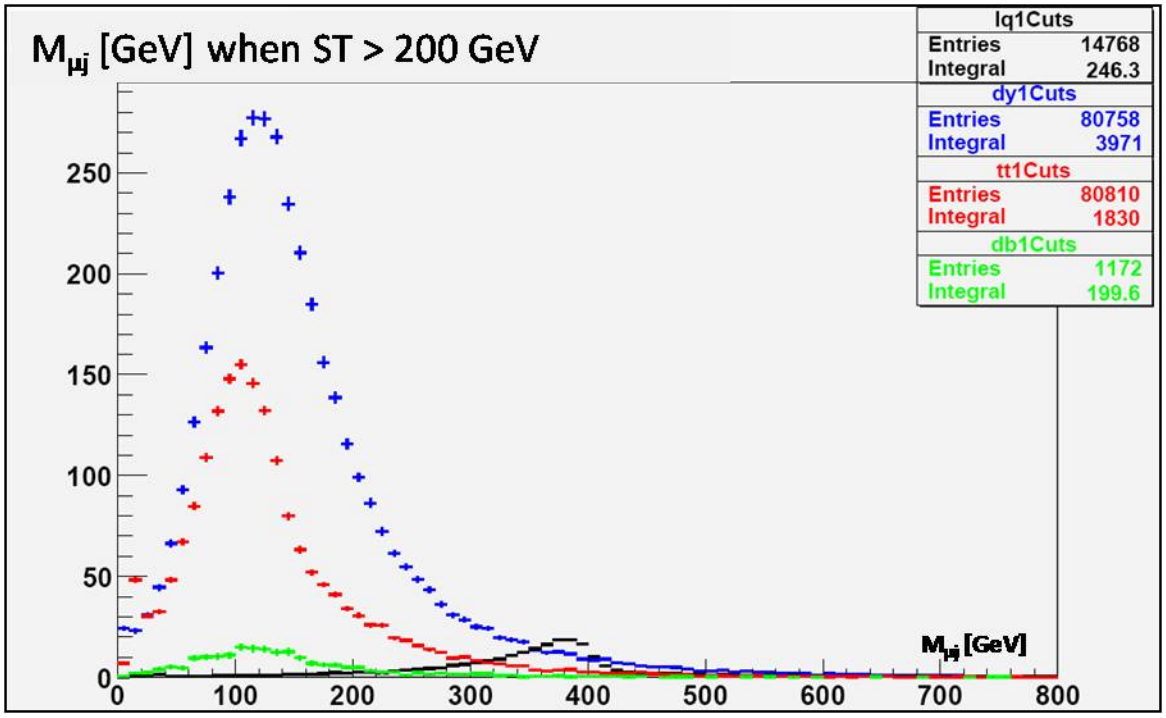

Figure 4.20: Reconstructed leptoquark pair masses in signal events (M_{LQ} = 400 GeV) (black), $t\bar{t}$ (red), Diboson (green), and Z/DY (blue). Note: 2 entries per event plotted for events with two muons and two jets with $p_T > 20$ GeV, and the scalar sum of final state objects' p_T is greater than 200 GeV. MC events were generated at 10 TeV center of mass energy.

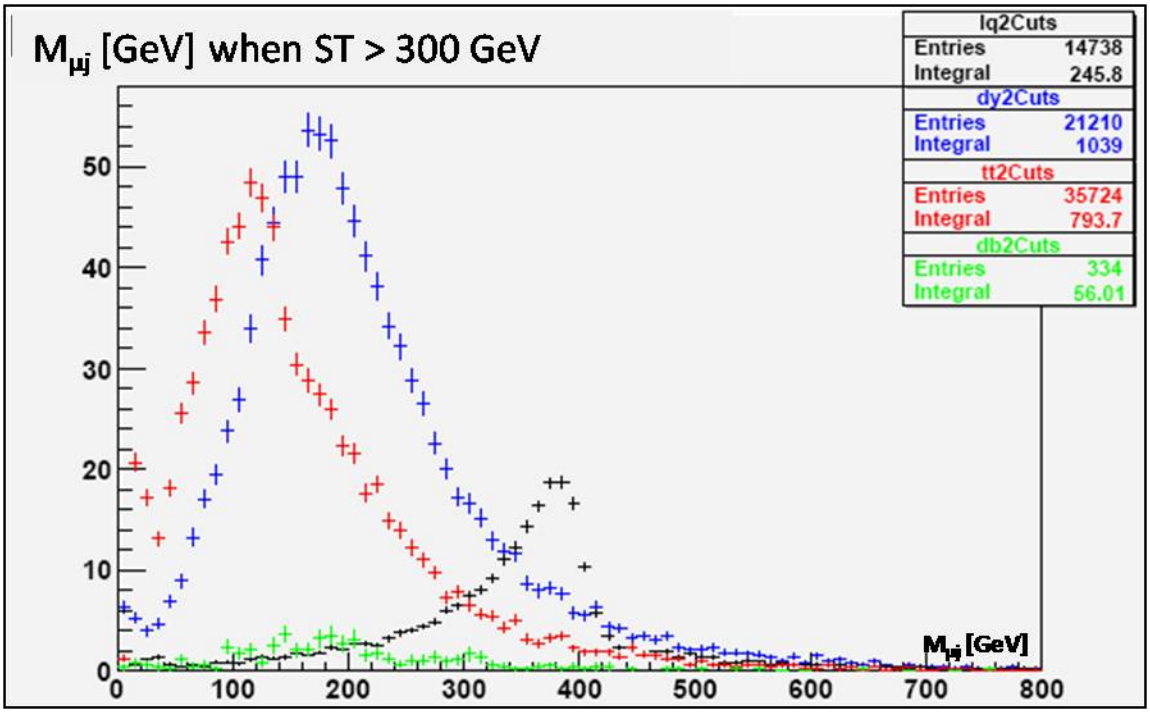

Figure 4.21: Reconstructed leptoquark pair masses in signal events (M_{LQ} = 400 GeV) (black), $t\bar{t}$ (red), Diboson (green), and Z/DY (blue). Note: 2 entries per event plotted for events with two muons and two jets with $p_T > 20$ GeV, and the scalar sum of final state objects' p_T is greater than 300 GeV. MC events were generated at 10 TeV center of mass energy.

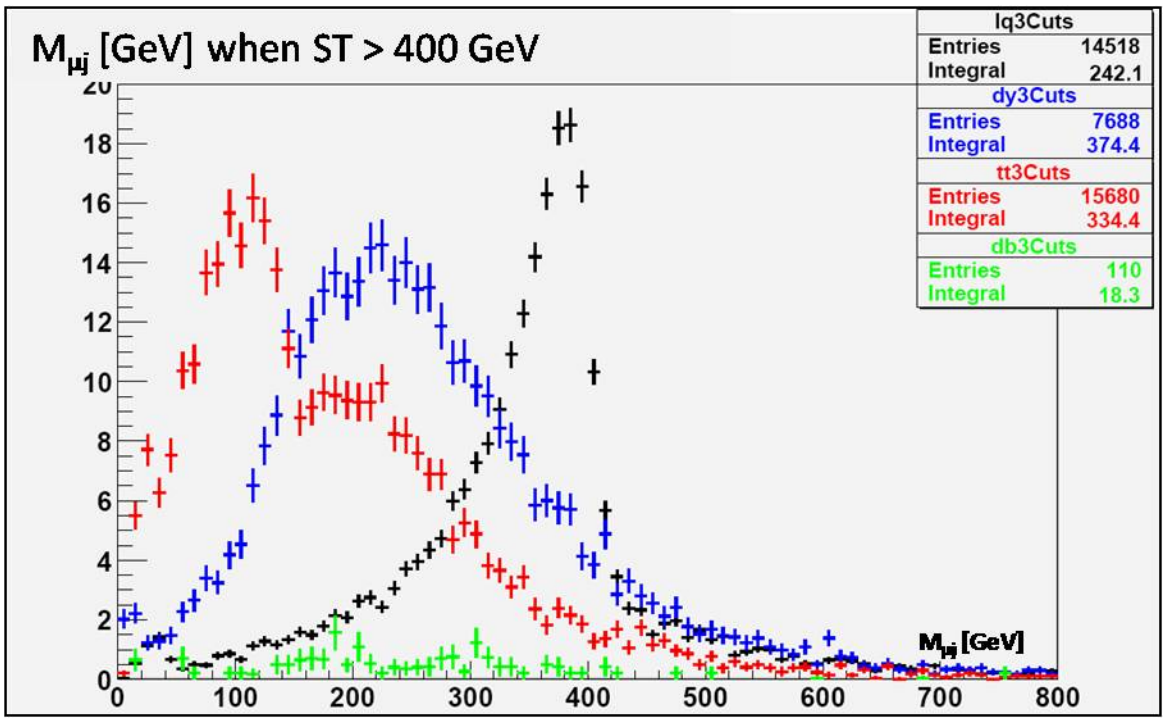

Figure 4.22: Reconstructed leptoquark pair masses in signal events (M_{LQ} = 400 GeV) (black), $t\bar{t}$ (red), Diboson (green), and Z/DY (blue). Note: 2 entries per event plotted for events with two muons and two jets with $p_T > 20$ GeV, and the scalar sum of final state objects' p_T is greater than 400 GeV. MC events were generated at 10 TeV center of mass energy.

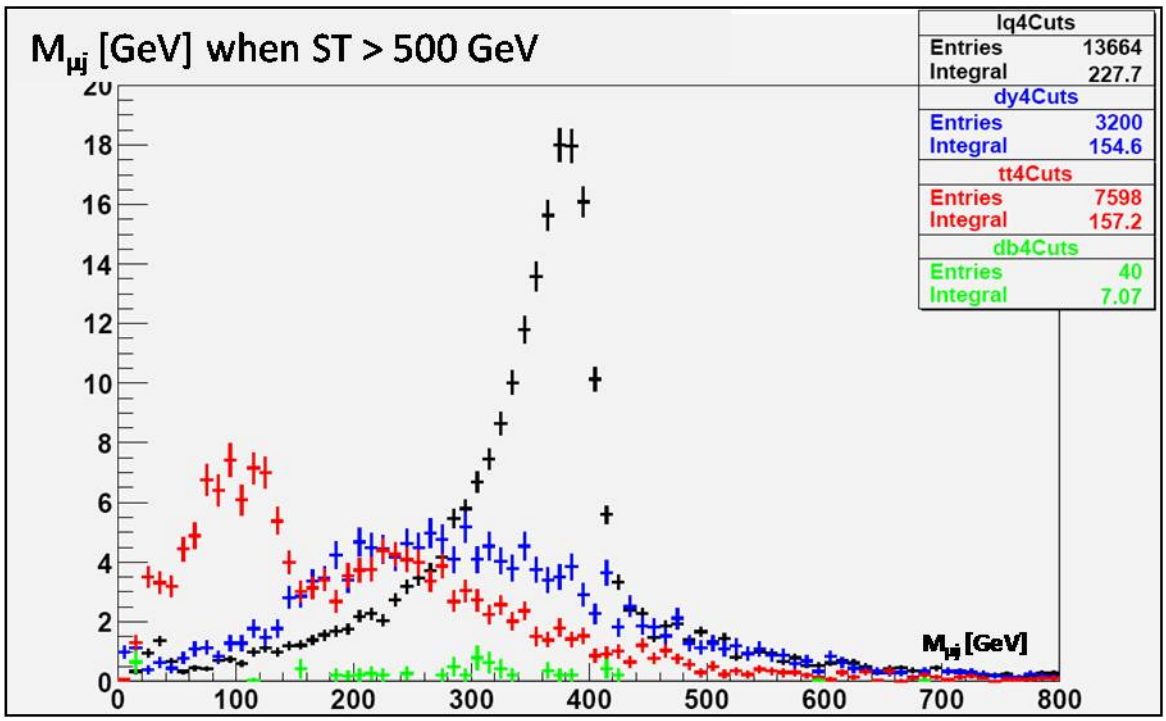

Figure 4.23: Reconstructed leptoquark pair masses in signal events (M_{LQ} = 400 GeV) (black), $t\bar{t}$ (red), Diboson (green), and Z/DY (blue). Note: 2 entries per event plotted for events with two muons and two jets with $p_T > 20$ GeV, and the scalar sum of final state objects' p_T is greater than 500 GeV. MC events were generated at 10 TeV center of mass energy.

- 20% uncertainty on the integrated luminosity
- An uncertainty of 12% on the $t\bar{t}$ cross section
- An uncertainty of 10% on the Z/DY cross section
- An uncertainty of 50% on the QCD cross section
- Statistical uncertainties on the number of background MC events were considered as systematic uncertainties on the number of background events
- The systematic uncertainty on the NLO leptoquark cross section [25] was calculated using the 40 PDF CTEQ6M tables (two per eigenvector of PDF variations) provided by the CTEQ group for calculating uncertainties [33]. Cross sections were recalculated using these tables, two variations for each of the 20 eigenvectors. For each eigenvector, the variation that yielded the largest difference in cross section from the standard CTEQ6M table was taken. The quadratic sum of these differences and the relative differences obtained by varying the renormalization and factorization scale by a factor of 2 (from $\mu = M_{LQ}$) was taken as the systematic uncertainty in the leptoquark pair production cross section.
- An uncertainty of 5% for muon identification, including trigger and reconstruction efficiencies
- Uncertainty on the jet energy scale was estimated by varying the energies of all jets simultaneously by a factor given by a Gaussian distribution centered at 1.0 with a width of 10%
- The uncertainty due to muon $1/p_T$ resolution was estimated using a Gaussian smearing of $1/p_T$ [GeV^{-1}] with a width of $0.011/p_T \oplus 0.00017$
- The uncertainty due to jet energy resolution was estimated using a Gaussian smearing of jet energies such that the relative jet energy resolution widens from $0.60/\sqrt{E} \oplus 0.05$ to $0.75/\sqrt{E} \oplus 0.07$, where E is in GeV

The effect of these uncertainties on signal and background selection efficiencies is summarized in Tables 4.10 and 4.12. The uncertainty on the signal is dominated by the uncertainty associated with muon reconstruction and the leptoquark cross section, while the uncertainty on background is dominated by limited MC statistics and the uncertainty on the jet energy scale.

Source of uncertainty	% Effect on signal	% Effect on background
Leptoquark cross section	15	–
Muon resolution	8	8
Jet energy scale	4.8	35
Jet resolution	1.5	16

Table 4.10: Relative systematic uncertainties for 400 GeV leptoquark mass hypothesis at 100 pb^{-1} integrated luminosity and 14 TeV center of mass energy [32].

Source of uncertainty	% Effect on signal				% Effect on background			
LQ mass hypothesis [GeV]	200	300	400	500	200	300	400	500
Integrated luminosity	20	20	20	20	20	20	20	20
$t\bar{t}$ cross section	–	–	–	–	4.7	1.5	3	12
Z/DY cross section	–	–	–	–	6	8.8	10	10
QCD cross section	–	–	–	–	1.7	5.6	12.5	50
Limited MC statistics	1.3	1.5	1.3	1.4	18.9	35.4	57.8	100
Muon reconstruction/trigger	10	10	10	10	10	10	10	10

Table 4.11: Relative systematic uncertainties for various leptoquark mass hypothesis at 7 TeV center of mass energy.

M_{LQ} [GeV]	% Effect on signal	% Effect on background
200	28.6	49.6
300	28.6	58.4
400	28.6	75.2
500	28.6	121.6

Table 4.12: Total relative systematic effect for signal and background for various leptoquark mass hypotheses.

4.10 RESULTS

Since leptoquark masses less than 150 GeV have been excluded by previous experiment for all branching fractions $\beta(LQ \to \mu q)$, only events where both leptoquark candidate masses are greater than 150 GeV are counted when calculating sensitivity. Exclusion confidence levels are evaluated as $(1 - CL_s)$, where $CL_s = CL_{s+b}(N_b)/CL_b(N_b)$, CL_{s+b} is the probability of observing a certain number of events or less, given a signal+background hypothesis, CL_b is the probability of observing a certain number of events or less, given the background-only hypothesis, and N_b is the expected number of background events. Discovery sensitivity is evaluated as $(1 - CL_b(N_s + N_b))$, where N_s is the expected number of signal events and N_b is the expected number of background events. This probability of $(1 - CL_b)$ is given in units of Gaussian standard deviations. CL_s is calculated with the TLimit package in ROOT [34], which uses a semi-Bayesian likelihood ratio method adapted from [35], and CL_b is calculated using S_{cp} [36].

Neglecting systematic uncertainties and using a branching fraction $\beta = 1$, the luminosities required to exclude various leptoquark masses at the 95% confidence level with this analysis are shown in Table 4.13, luminosities required to exclude masses at the 99% confidence level are shown in Table 4.14, and finally, the luminosities required to discover leptoquark masses at the 5σ level are shown in Table 4.15. These results are also summa-

rized in Figure 4.24. Exclusion limits can only be calculated for integer values of N_{obs}, so $N_{obs} = <N_b>$ is rounded up. Due to the high signal to background ratio in this analysis, this generally results in N_{obs} =1, and the exclusion limits for this calculation becomes a simple limit calculation in Poisson statistics, looking for the probability distribution whose lower limit corresponds to an observed value of 1, as can be seen in Tables 4.13 and 4.14. When comparing exclusion and discovery limits, one must compare the widths of the N_{s+b} distribution and N_b distribution. The decreasing signal to background ratio Tables 4.13 and 4.14 is due to the fact that the leptoquark cross section drops more quickly than the efficiency of background for selection criteria at higher mass hypotheses. As a result, the width of the N_b distribution becomes more comparable to the width of the N_{s+b} distribution with increasing leptoquark mass, and discovery limits will diverge from exclusion limits, as seen in Figure 4.15.

In addition, discovery and exclusion potential may be considered as a function of β for a given luminosity. The minimum branching fractions that can be probed with 100 pb^{-1} of integrated luminosity are shown as a function of leptoquark mass in Tables 4.16, 4.17, and 4.18. These results are also summarized in Figure 4.25. In contrast to the previous exclusion calculations, at a constant luminosity and varying β, various leptoquark hypotheses yield different numbers background events, which are determined solely by the luminosity and background suppression efficiencies for each set of selection criteria. Finding the corresponding number of signal events that yields an exclusion limit brings the widths of N_{s+b} and N_b as close as possible while still satisfying the discovery and exclusion criteria. This results in an increasing signal to background ratio with increasing leptoquark mass (and decreasing number of background events). Consequently, discovery limits converge with exclusion limits toward higher mass, as seen in Figure 4.25.

Inclusion of systematic errors will obviously reduce the sensitivity of the analysis and will do so with varying degrees depending on the calculation. With $\beta = 1$, the minimum luminosities required to discover and exclude various leptoquark masses are shown in Tables 4.19, 4.20, and 4.21. These results are also summarized in Figures 4.26, 4.27, and 4.28.

Since CL_s quantities are evaluated with $N_{obs} = <N_b>$, the calculation is driven by location of $<N_b>$ in the Poisson probability distribution P_{s+b}, with expectation value N_{s+b}.

M_{LQ} [GeV]	Luminosity pb^{-1}	# signal events	# background events
200	1.34	4.84	0.229
300	7.70	4.84	0.377
400	38.6	4.87	0.708
500	190	5.61	1.16

Table 4.13: Luminosity required for exclusion at 95% confidence level for various M_{LQ} and the corresponding number of signal and background events

M_{LQ} [GeV]	Luminosity pb^{-1}	# signal events	# background events
200	1.86	6.72	0.319
300	10.7	6.73	0.524
400	54.4	6.86	0.998
500	261	7.70	1.60

Table 4.14: Luminosity required for exclusion at 99% confidence level for various M_{LQ} and the corresponding number of signal and background events

M_{LQ} [GeV]	Luminosity pb^{-1}	# signal events	# background events
200	1.66	5.99	0.284
300	11.5	7.23	0.563
400	76.0	9.59	1.39
500	391	11.5	2.39

Table 4.15: Luminosity required for 5σ discovery for various M_{LQ} and the corresponding number of signal and background events

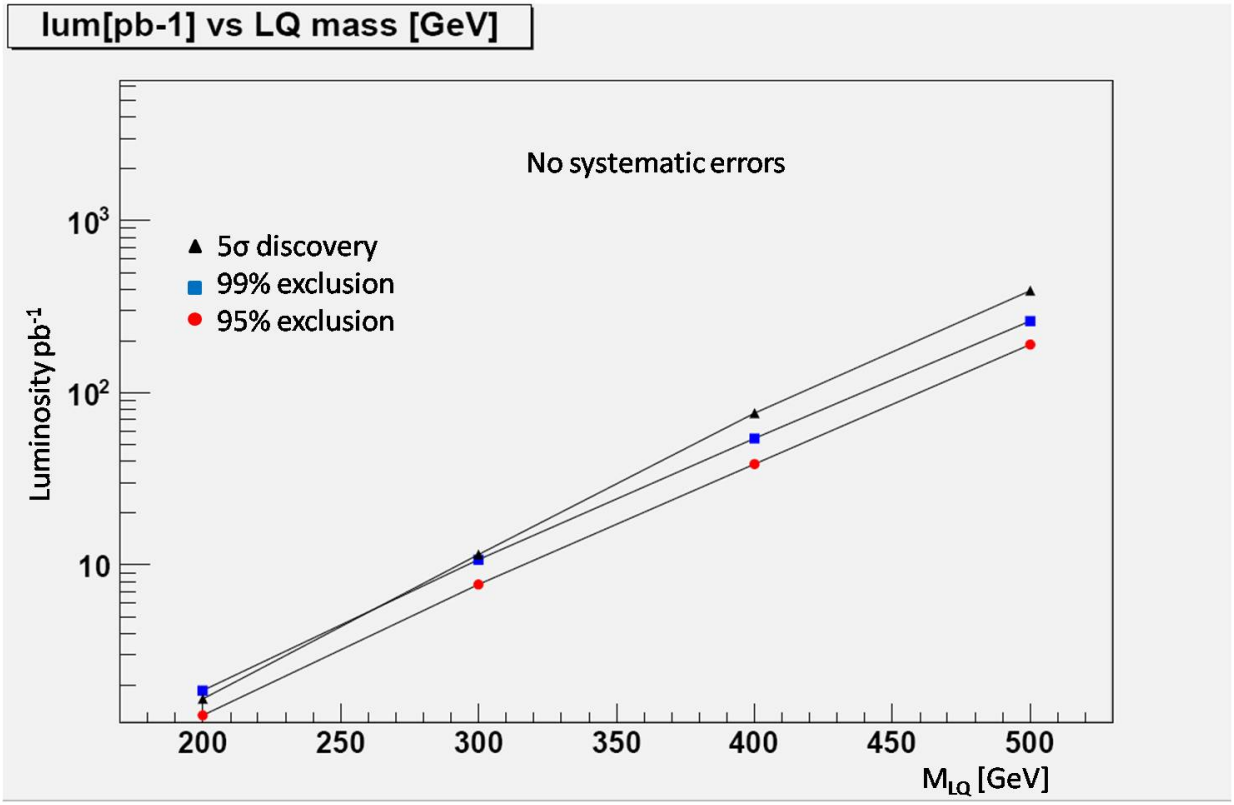

Figure 4.24: Luminosity required for exclusion if $N_{obs} = <N_b>$ at 95% CL (red) and 99% CL (blue) and luminosity required to discover leptoquarks if $N_{obs} = <N_s + N_b>$ (black) as a function of M_{LQ} [GeV].

M_{LQ} [GeV]	$\beta(LQ \to \mu q)$	# signal events	# background events
200	0.176	11.2	17.1
300	0.334	7.0	4.9
400	0.662	5.5	1.8

Table 4.16: Minimum branching fraction required for exclusion at 95% confidence level for various M_{LQ} and the corresponding number of signal and background events

M_{LQ} [GeV]	$\beta(LQ \to \mu q)$	# signal events	# background events
200	0.202	14.7	17.1
300	0.388	9.5	4.9
400	0.790	7.9	1.8

Table 4.17: Minimum branching fraction required for exclusion at 99% confidence level for various M_{LQ} and the corresponding number of signal and background events

M_{LQ} [GeV]	$\beta(LQ \to \mu q)$	# signal events	# background events
200	0.264	25.2	17.1
300	0.490	15.1	4.9
400	0.914	10.5	1.8

Table 4.18: Minimum branching fraction required for 5σ discovery for various M_{LQ} and the corresponding number of signal and background events

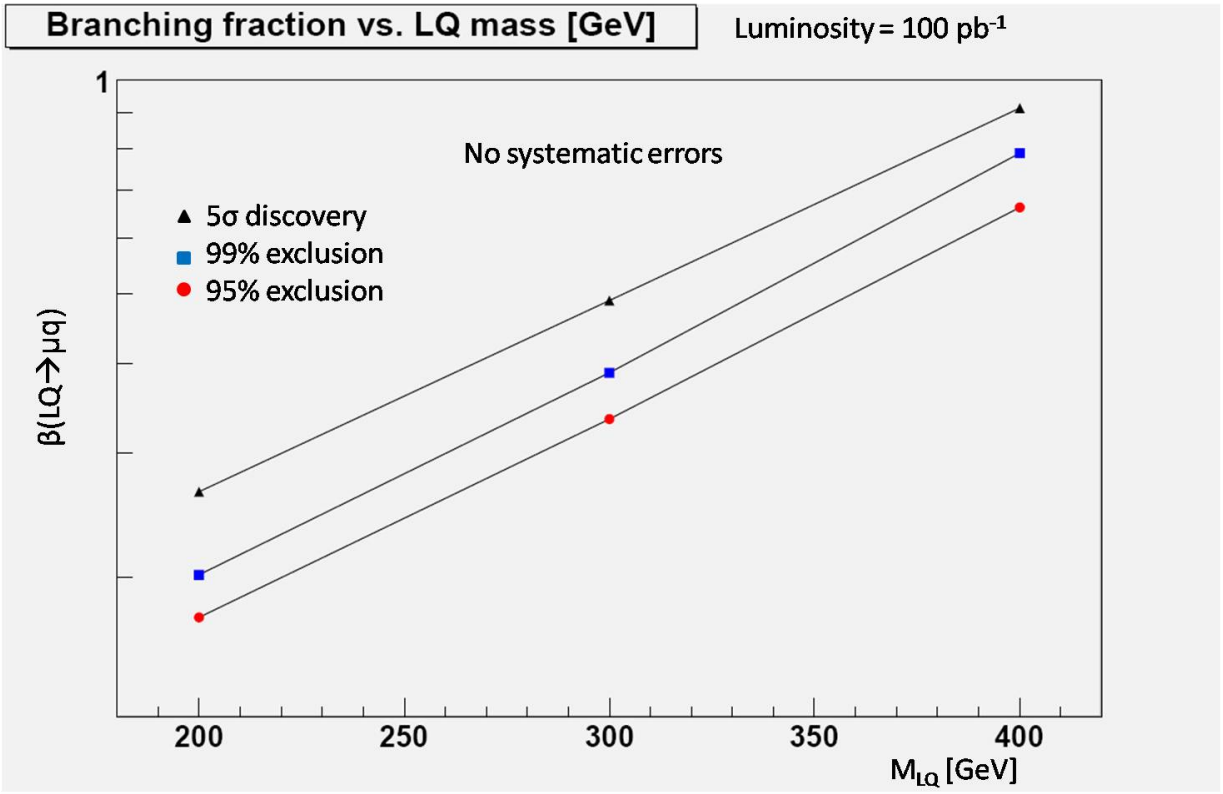

Figure 4.25: Minimum branching fraction $\beta(LQ \rightarrow \mu q)$ that can be excluded if $N_{obs} = <N_b>$ at 95% CL (red) and 99% CL (blue) and minimum branching fraction that could be discovered if $N_{obs} = <N_s + N_b>$ (black) as a function of M_{LQ} [GeV].

Alternatively, CL_b calculations are driven by the location of N_{s+b} in the Poisson probability distribution P_b, with expectation value N_b. As a result, exclusion limits are extremely tolerant of the large errors associated with backgrounds at high leptoquark masses, while discovery limits are not. The small number of events (both signal and background) required for exclusion calculations, and the constant systematic error assumed for all signal mass hypotheses results in a constant effect on exclusion limits as a function of leptoquark mass, as seen in Figure 4.28. In contrast, the large systematic error on backgrounds at high leptoquark mass (due to limited MC statistics), has a rather drastic effect on discovery potential at high masses, as seen in Figure 4.27.

The minimum branching fractions that can be probed with 100 pb^{-1}, when systematic errors are considered, are shown in Tables 4.22, 4.23, and 4.24. These results are also summarized in Figure 4.29. In contrast to the luminosity calculations, systematic errors affect the results of exclusion calculations more in lower mass points than high mass points, as seen in Figures 4.30 and 4.31. This is simply the result of the number of signal and background surviving selection criteria at each mass point. The dropping leptoquark cross section results in fewer signal events at higher masses. The decreasing number of background events surviving tighter selection criteria results in fewer background events at higher mass hypotheses. This results in both Poisson probability distributions with lower expectation values, smaller widths, and smaller absolute errors due to systematics. For example, a relatively large number of background events contributes to the N_{s+b} probability distribution at a leptoquark mass hypothesis of 200 GeV. Even with much smaller relative systematic error, this will have more of an effect on the width of that probability distribution than the background contribution to the $M_{LQ} = 500$ GeV mass hypothesis. This can be seen in the increasing signal to background ratio in Tables 4.22 and 4.23. The same effect is present for discovery potential. Although there is an increase in the relative systematic error for backgrounds between $M_{LQ} = 200$ and $M_{LQ} = 300$, this is overshadowed by the drastic drop in the number of background events surviving selection criteria for these two mass points.

M_{LQ} [GeV]	Luminosity pb^{-1}	# signal events	# background events
200	1.52	5.49	0.260
300	8.70	5.47	0.426
400	42.4	5.35	0.778
500	218	6.44	1.33

Table 4.19: Luminosity required for exclusion at 95% confidence level for various M_{LQ}, when considering systematic errors, and the corresponding number of signal and background events

M_{LQ} [GeV]	Luminosity pb^{-1}	# signal events	# background events
200	2.32	8.38	0.397
300	13.0	8.18	0.636
400	72.8	9.19	1.34
500	312	9.21	1.91

Table 4.20: Luminosity required for exclusion at 99% confidence level for various M_{LQ}, when considering systematic errors, and the corresponding number of signal and background events

M_{LQ} [GeV]	Luminosity pb^{-1}	# signal events	# background events
200	1.96	7.08	0.336
300	15.7	9.88	0.768
400	169	21.3	3.10
500	6140	181	37.6

Table 4.21: Luminosity required for 5σ discovery for various M_{LQ}, when considering systematic errors, and the corresponding number of signal and background events

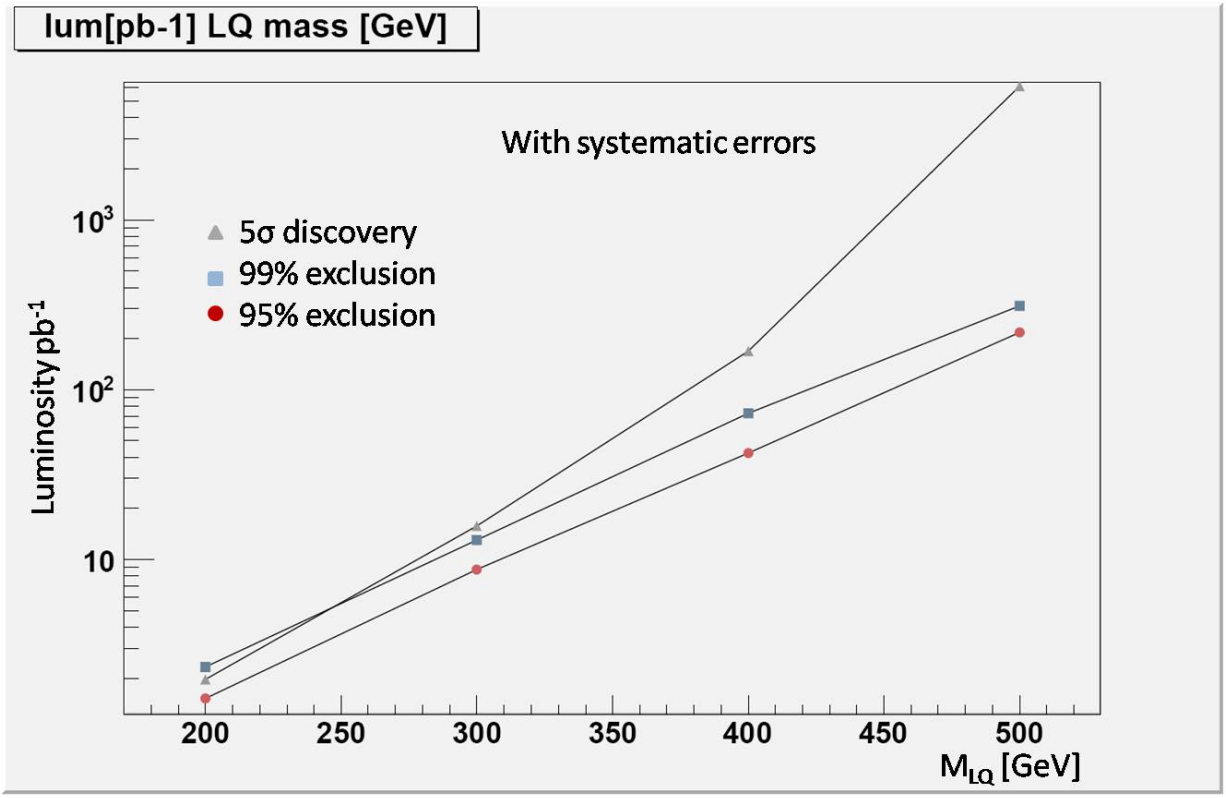

Figure 4.26: Luminosity required for exclusion if $N_{obs} = <N_b>$ at 95% CL (dark red) and 99% CL (light blue) and luminosity required to discover leptoquarks if $N_{obs} = <N_s + N_b>$ (gray) as a function of M_{LQ} [GeV], when systematic errors are included.

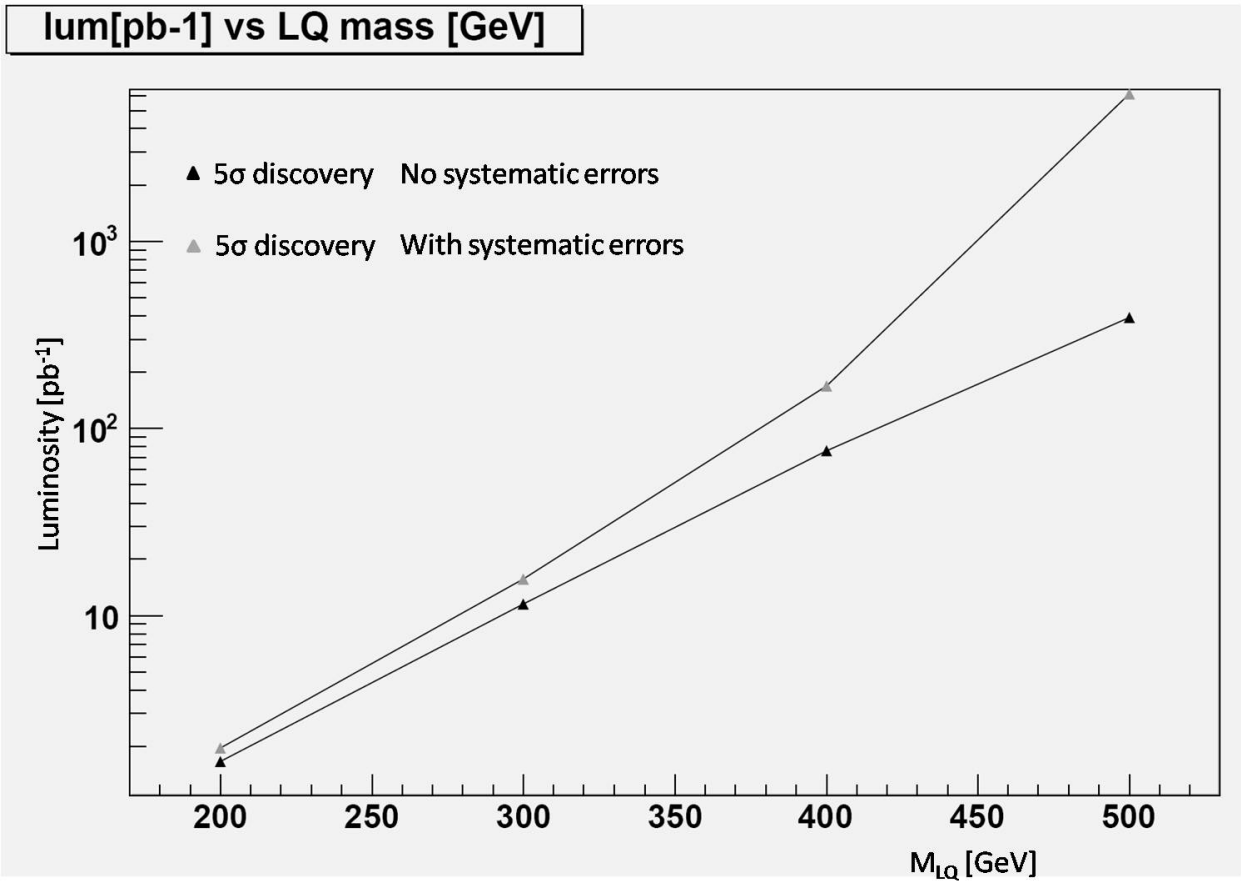

Figure 4.27: Luminosity required to discover leptoquarks if $N_{obs} = <N_s + N_b>$ (gray/black) as a function of M_{LQ} [GeV], when systematic errors are included/ignored.

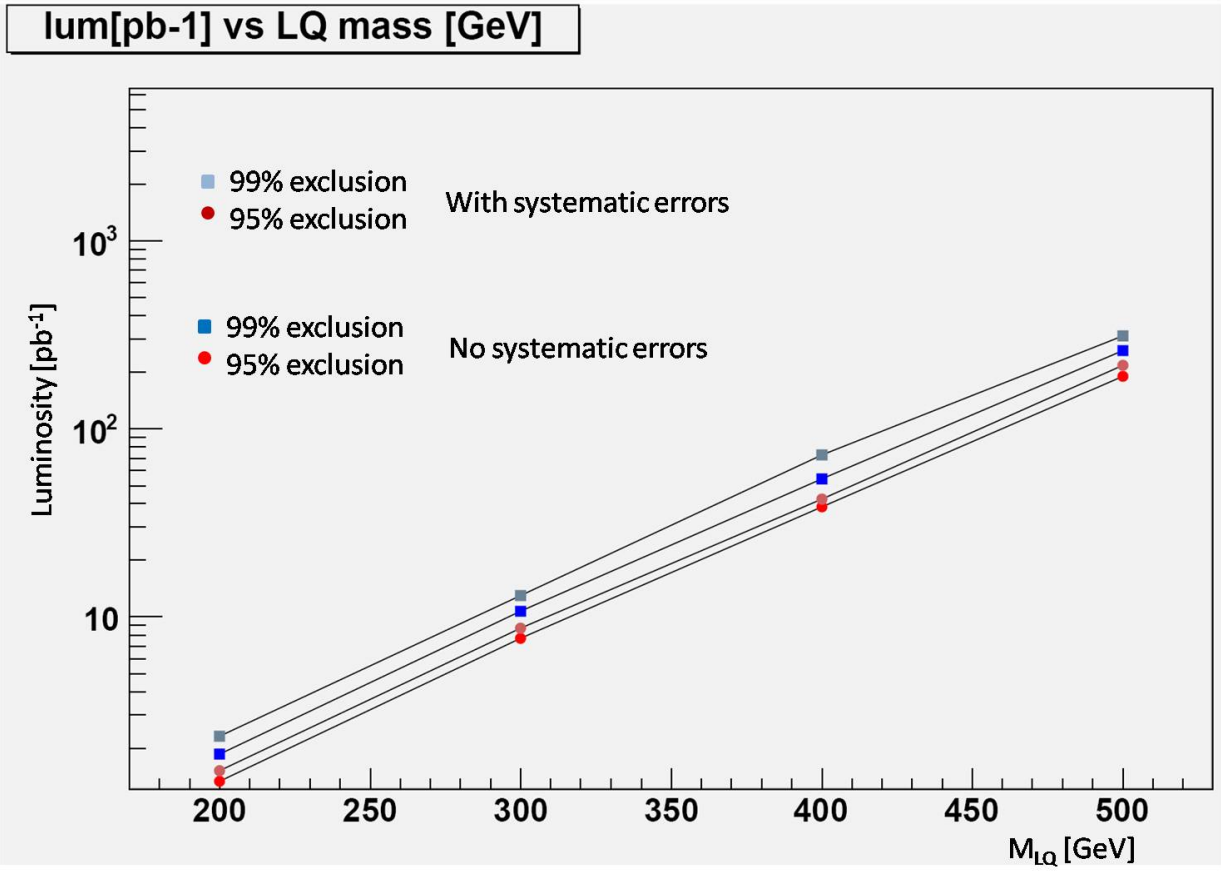

Figure 4.28: Luminosity required for exclusion if $N_{obs} = <N_b>$ at 95% CL (dark red/bright red) and 99% CL (light blue/bright blue) as a function of M_{LQ} [GeV], when systematic errors are included/ignored.

M_{LQ} [GeV]	$\beta(LQ \to \mu q)$	# signal events	# background events
200	0.288	29.9	17.1
300	0.430	11.6	4.9
400	0.766	7.4	1.8

Table 4.22: Minimum branching fraction required for exclusion at 95% confidence level for various M_{LQ}, when systematic errors are considered, and the corresponding number of signal and background events

M_{LQ} [GeV]	$\beta(LQ \to \mu q)$	# signal events	# background events
200	0.340	41.7	17.1
300	0.516	16.7	4.9
400	0.908	10.4	1.8

Table 4.23: Minimum branching fraction required for exclusion at 99% confidence level for various M_{LQ}, when systematic errors are considered, and the corresponding number of signal and background events

M_{LQ} [GeV]	$\beta(LQ \to \mu q)$	# signal events	# background events
200	0.376	51.0	17.1
300	0.626	24.6	4.9

Table 4.24: Minimum branching fraction required for 5σ discovery for various M_{LQ}, when systematic errors are considered, and the corresponding number of signal and background events

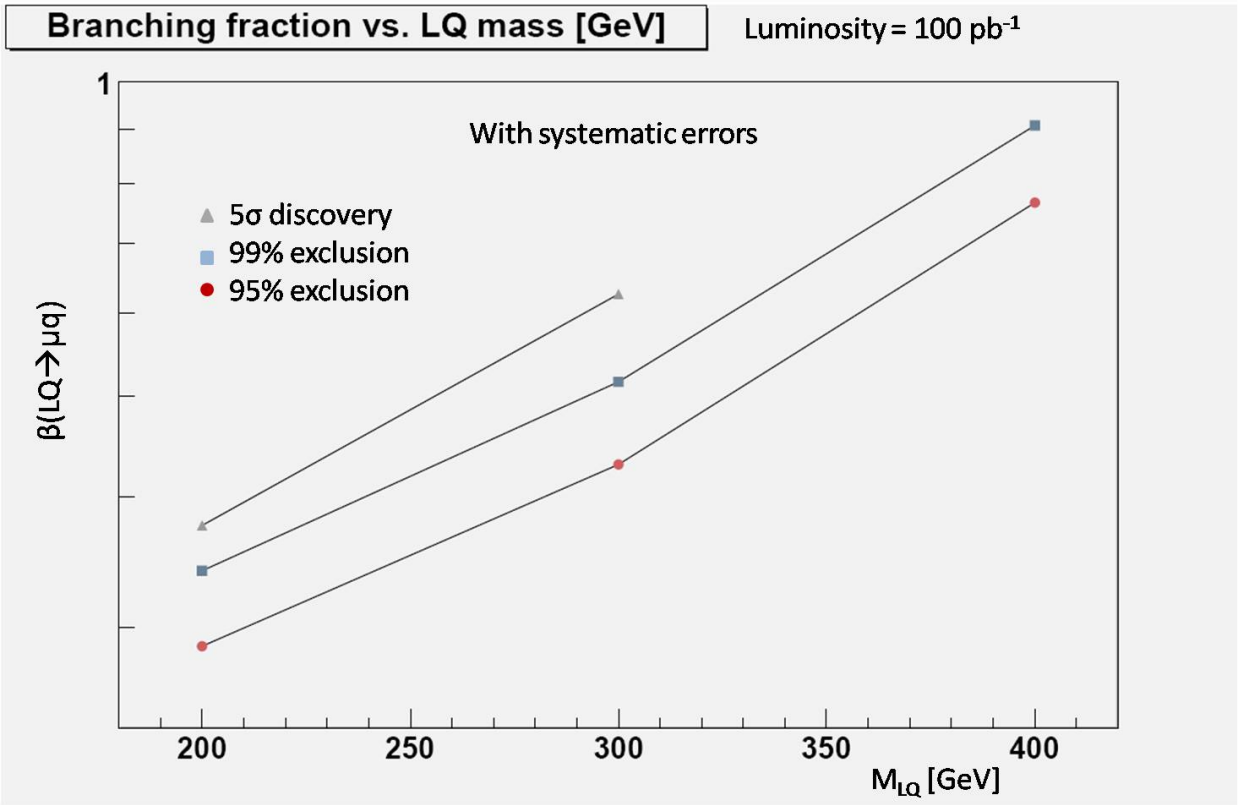

Figure 4.29: Minimum branching fraction $\beta(LQ \to \mu q)$ that can be excluded if $N_{obs} = <N_b>$ at 95% CL (dark red) and 99% CL (light blue) and minimum branching fraction that could be discovered if $N_{obs} = <N_s + N_b>$ (gray) as a function of M_{LQ} [GeV], when systematic errors are included.

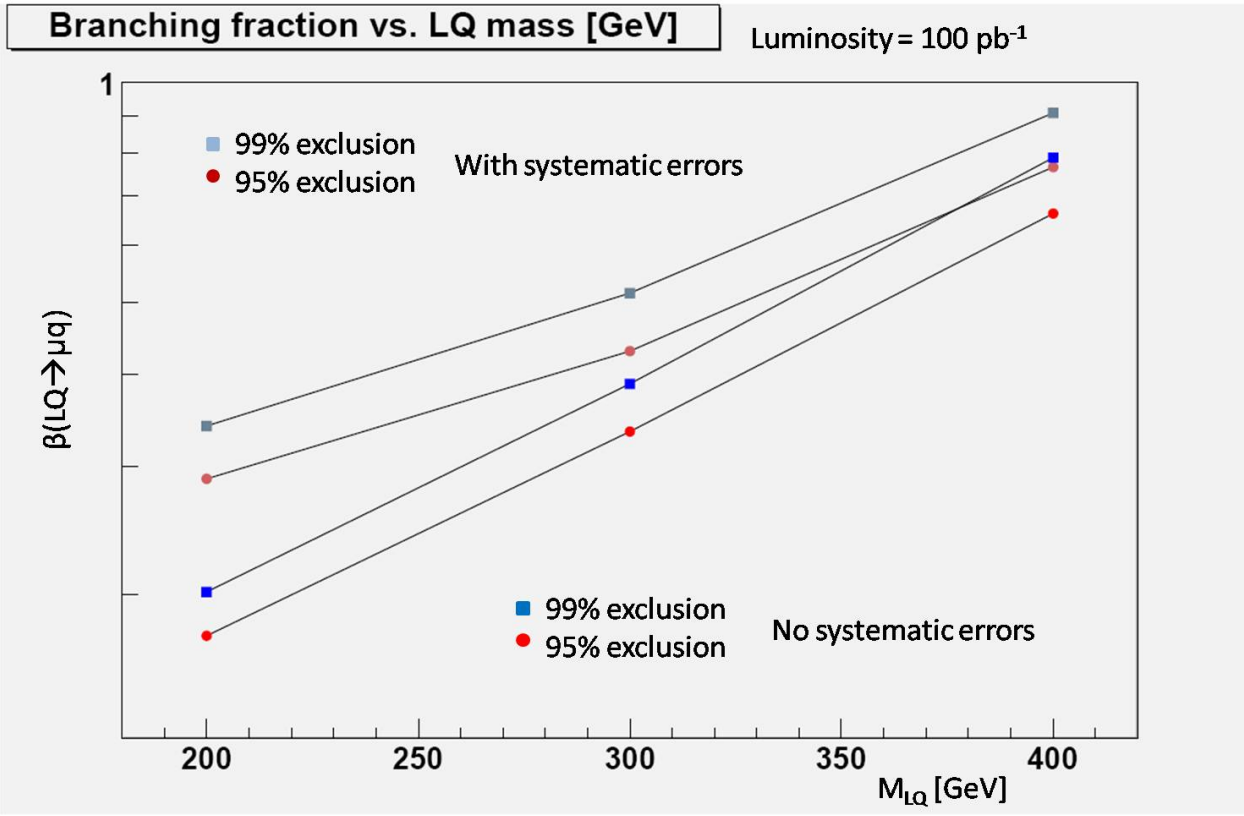

Figure 4.30: Minimum branching fraction $\beta(LQ \to \mu q)$ that can be excluded if $N_{obs} = <N_b>$ at 95% CL (dark red/bright red) and 99% CL (light blue/bright blue), when systematic errors are included/ignored.

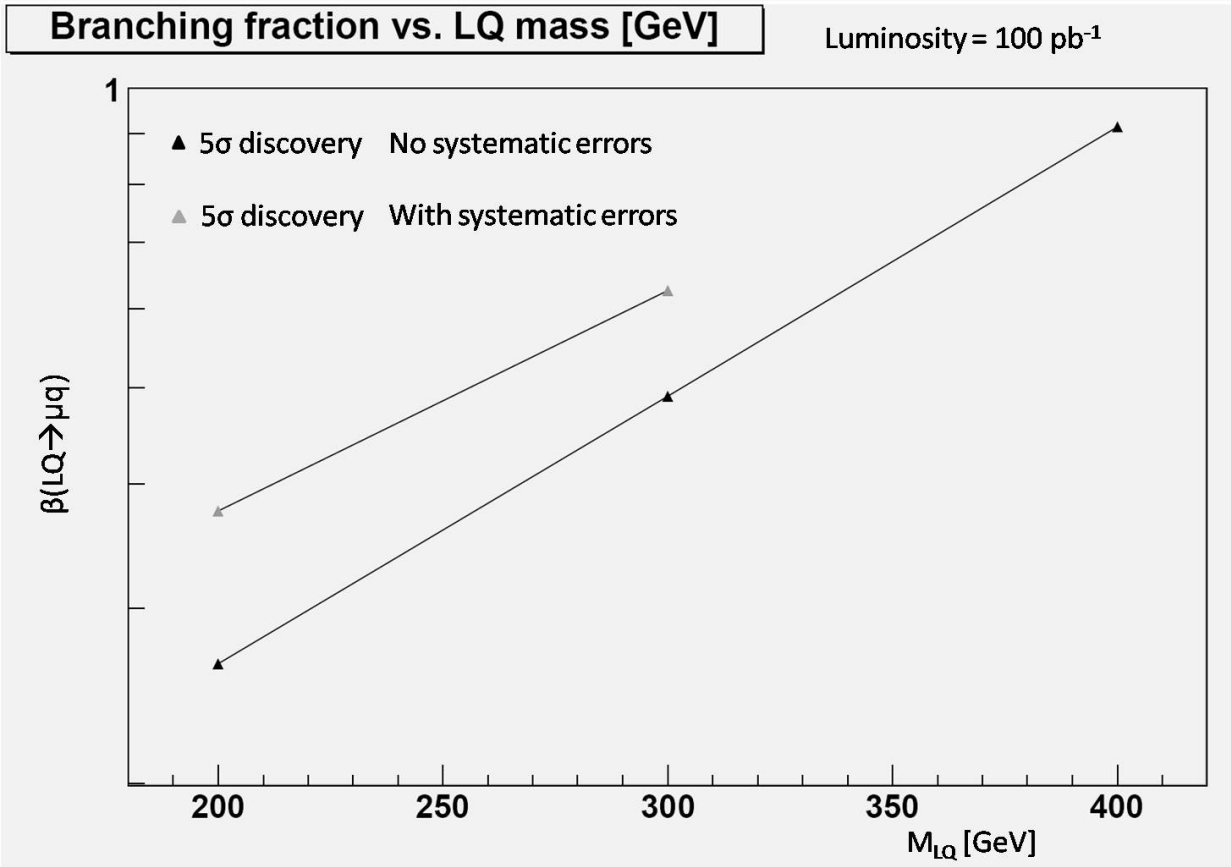

Figure 4.31: Minimum branching fraction $\beta(LQ \to \mu q)$ that can be discovered if $N_{obs} = <N_s + N_b>$ (gray/black) as a function of M_{LQ} [GeV], when systematic errors are included/ignored.

5.0 CONCLUSIONS

Significant improvements can be made on existing limits for second generation leptoquarks with early ATLAS data. Even with the reduced center of mass energy for the colliding proton beams, the LHC provides an excellent opportunity to discover leptoquarks with masses less than 500 GeV. With less than 50 pb^{-1} of integrated luminosity, leptoquarks with masses less than 400 GeV can be excluded at β=1, a significant improvement on current Tevatron limits. With 100 pb^{-1} of integrated luminosity, branching fractions of more than 0.43 can be excluded for M_{LQ} = 300 GeV, compared to the D0 limit of $M_{LQ} > 316$ GeV for β=1. Such leptoquarks could be discovered with the same luminosity of if $\beta > 0.625$. Finally, leptoquarks with masses less than 500 GeV could be discovered with data taken before the LHC is brought down for repairs in 2012 if such leptoquarks always decay to a muon and quark.

BIBLIOGRAPHY

[1] J. Blmlein and R. Ruckl, Phys. Lett. **B304** (1993) 337.

[2] W. Buchmuller and D. Wyler, Phys. Lett. **B177** (1986) 377.

[3] O. Bruning, P. Collier, P. Lebrun, S. Myers, R. Ostojic, J. Poole, and P. Proudlock, LHC Design Report, CERN (2004).

[4] ATLAS Collaboration, Magnet System Technical Design Report, CERN/LHCC/97-18 (1997).

[5] ATLAS Collaboration, Inner Detector Technical Design Report, CERN/LHCC/97-16 (1997).

[6] T. Cornelissen et al., 2008 J. Phys.: Conf. Ser. **119** 032014.

[7] ATLAS Collaboration, arXiv:0901.0512: p16-42 (2008).

[8] ATLAS Collaboration, arXiv:0901.0512 (2008).

[9] ATLAS Collaboration, Calormieter Performance Technical Design Report, CERN/LHCC/96-40 (1996).

[10] W. Lampl et al., Calorimeter Clustering Algorithms: Description and Performance, ATLAS-LARG-PUB-2008-002 (2008).

[11] L. Alsquith, et al., ATL-COM-PHYS-2009-630 (2009).

[12] ATLAS Collaboration, arXiv:0901.0512: p72-140 (2008).

[13] ATLAS Collaboration, Muon Spectrometer Technical Design Report, CERN/LHCC/97-22 (1997).

[14] S. Hassini et al., NIM **A572** (2007) 7779.

[15] ATLAS Collaboration, arXiv:0901.0512: p161-184 (2008).

[16] Th. Lagouri, et al., IEEE Trans. Nucl. Sci. 51 (2004) 30303033.

[17] ATLAS Collaboration, First-Level Trigger Technical Design Report, CERN/LHCC/98-14 (1998).

[18] S. Agostinelli et al., NIM **A506** (2003) 250.

[19] ATLAS Collaboration, Computing Technical Proposal, CERN/LHCC/96-43 (1996).

[20] T. Sjostrand, S. Mrenna and P. Skands, JHEP **05** (2006) 026.

[21] S. Frixione and B.R. Webber, JHEP **06** (2002) 029.

[22] G. Corcella et al., JHEP **01** (2001) 010.

[23] W. Buchmuller, R. Ruckl, and D. Wyler, Phys. Lett. **B191** (1987) 442.

[24] A. Belyaev, C. Leroy, R. Mehdiyev, and A. Pukhov, arXiv:hep-ph/0502067v1 (2005).

[25] M. Kramer, T. Plehn, M. Spira and P. M. Zerwas, arXiv:hep-ph/0411038.

[26] V. M. Abazov et al., Phys. Lett. **B671** (2009) 224.

[27] A. Abulencia et al., Phys. Rev. **D73** (2006) 051102.

[28] A. Aktas et al., Phys. Lett. **B629** (2005) 9.

[29] S. Chekanov et al., Phys. Rev. **D68** (2003) 052004.

[30] C. Friberg, E. Norrbin, T Sjostrand, Phys. Lett. **B403** (1997) 329.

[31] A. Sherstnev, R. S. Thome, arXiv:0711.2473v2 [hep-ph] (2007).

[32] ATLAS Collaboration, arXiv:0901.0512: p1750-68 (2008).

[33] J. Pumplin et al., JHEP 07 (2002) 012, arXiv:hep-ph/0201195.

[34] R. Brun and F. Rademakers, NIM **A389** (1997) 81-86.

[35] T. Junk, NIM **A434**, (1999) 435-443.

[36] S. I. Bityukov, S. E. Erofeeva, N. V. Krasnikov, and A. N. Nikitenko. Prepared for PHYSTATO5: Statistical Problems in Particle Physics, Astrophysics and Cosmology, Oxford, England, United Kingdom, 12-15 Sep 2005.